Fall 2012

The characterization of volatiles associated with young stellar objects

Kari Anne Wojtkowski

Department: Physics

THE CHARACTERIZATION OF VOLATILES ASSOCIATED WITH YOUNG STELLAR OBJECTS

by

KARI ANNE WOJTKOWSKI

A DISSERTATION

Presented to the Faculty of the Graduate Schools of the

UNIVERSITY OF MISSOURI - ST. LOUIS and the

MISSOURI UNIVERSITY OF SCIENCE AND TECHNOLOGY

in Partial Fulfillment of the Requirements for the Degree

DOCTOR OF PHILOSOPHY

in

PHYSICS & ASTRONOMY

2012

Approved by:
Dr. Erika L. Gibb, co-advisor
Dr. John L. Schmitt, co-advisor
Dr. Bruce A. Wilking
Dr. Jerry L. Peacher
Dr. Terry W. Rettig

ABSTRACT

In the first portion of this work, we searched for differences in volatiles within a single star forming region, Rho Ophiuchi. We determined the amount, temperature, and composition of two ice features, the bending modes of CO_2 and H_2O at 15 μm and 6 μm, respectively, toward 28 Young Stellar Objects (YSOs). We found that more than 50% of the YSOs studied contained a portion of crystalline CO_2 ice. We also found that some sources with Flat or borderline Class II Spectral Energy Distributions (SEDs) have a larger abundance of CO_2 ice with respect to H_2O ice. In addition to intracloud differences, we compared our results with several other star forming regions, high mass YSOs, and background objects. The average abundance of CO_2 with respect to H_2O in Rho Oph is comparable to that in Taurus, Perseus, and the value reported by Oberg et al. (2011) toward high mass YSOs, however, it is less than the average abundance reported toward Corona Australis, Serpens, and the value cited by Oberg et al. (2011) toward low mass YSOs.

The second half of this work involved a study of gaseous HCN, C_2H_2, and CO toward a low mass binary system, GV Tau. We report the second detection of these simple molecules toward a low mass YSO. The abundances of these molecules are consistent with that toward the first low mass YSO with a detection, IRS 46 (Lahuis et al., 2006), models from Willacy and Woods (2009), Walsh et al. (2010), and Markwick et al. (2002), and comets. We also found that these molecules have a rotational temperature of $\sim$100 K - 200 K, indicating they may be located in the warm molecular layer of the disk.

This work is part of a larger study to characterize volatiles (others include CH_4, NH_3, the 6.8 μm absorption feature, and CH_3OH) in the gas and/or solid phase toward YSOs in different star forming regions. This characterization includes temperature, location, mass, evolutionary state, and abundance. These characteristics will be used as a diagnostic tool to determine the evolution of molecules during the star formation process.

ACKNOWLEDGMENT

I would like to start by thanking my advisor, Dr. Erika Gibb. Her guidance and instruction have been invaluable, as well as her advice and support on anything I asked about along the way. I would also like to thank my Rolla committee members, Drs. John Schmitt and Jerry Peacher, not only for taking the time to serve on my committee but also for their support and teaching excellence during my undergraduate years. Dr. Bruce Wilking is also deserving of a huge thank you. He made sure I received funding throughout my career, provided opportunities for me to gain teaching experience, and engaged in many discussions regarding my research. The final committee member I would like to thank is Dr. Terry Rettig. He has a way of asking questions that make you think, and feel good about yourself!

In addition to my committee, there have been numerous colleagues and friends who have given me support and help along the way. Dr. Sachin Shenoy taught me how to reduce Spitzer data and Dr. David Horne provided expertise and immeasurable support. There have also been several graduate and undergraduate students who have lended an ear, let me bounce ideas off of them, or helped me reduce data. Those people include Anamaria Balyut, Dan Blake, Logan Brown, Matt Dennis, Bryant Dentinger, Melissa Shenoy, Emily Sudholt, Jamie Williams, and Keara Wright. I would like to extend a very heartfelt thank you to each of these people for their help.

I would also like to acknowledge several sources of funding. First of all, I thank the Department of Physics and Astronomy for their continued support over many years. I would also like to thank the NASA Missouri Space Grant Consortium (Research Fellowship from 2000-2005), Sigma Xi (Grants-in-Aid of Research award), and the National Science Foundation (NSF Stellar Astronomy Grant #0621481, a stimulus grant) for their support.

My final thank you goes to all of my family and friends (including those previously mentioned). I could not have completed this dissertation without your patience and support!

TABLE OF CONTENTS

Page

LIST OF ILLUSTRATIONS

LIST OF TABLES

1. INTRODUCTION

Although the general process of star formation is known, many details of chemical evolution during this process remain unknown. For example, we do not understand how some simple molecules are formed in the interstellar medium (ISM), nor do we understand potential effects of the environment in which the star forms on the chemistry of the region. What effect does nearby radiation (or a lack thereof) have on molecule formation? Are simple molecules formed in the gas phase, or are grain surface reactions necessary? If they are formed on the grain, is it in a polar environment (with H_2O) or an apolar environment? If they are formed in the gas phase, where are they formed? Is it in the disk? If so, which part? This information is critical in order to describe how, where, and when more complex molecules, such as one of the precursors to life: amino acids, are formed and how they might be incorporated into planets. Furthermore, we would like to use our general knowledge of star formation to understand the circumstances surrounding our own solar system formation. Did our solar system form in isolation? Or did it form in the presence of other stars? If so, did it include massive stars with short lifetimes that could have injected the solar nebula with heavy elements? Are there unique differences in the abundances of simple molecules in different types of star forming regions that we can use as a diagnostic? To that end we will begin with a description of the ISM, in § 1.1, as it is the ISM where star forming regions develop. We will then give an overview of star formation in § 1.2, highlighting the stages we focus on in this research. This will be followed by examples of different kinds of star forming regions in § 1.3. Then we will describe the two subsets on which this research focuses, ices surrounding YSOs in § 1.5 and gases in the disk of YSOs in § 1.6, and finally describe the tools we need to complete this study in §1.7.

1.1. THE INTERSTELLAR MEDIUM (ISM)

We begin our discussion of star formation with the material from which stars are made, the interstellar medium (ISM). The ISM is not uniform, it contains clumps of various sizes, densities, and temperatures. We can categorize the ISM into four general components according to their physical properties (see for example Whittet (2003)). The first of these components is cold, dense molecular clouds with temperatures $\sim$ 15 K and densities $>$ 1x10^8 m^{-3}, where molecular hydrogen, H_2, is located. These regions can be large, with diameters up to 60 pc, and have masses up to a million solar masses. Cool regions composed of atomic hydrogen, H I, known as diffuse clouds, comprise the second component of the ISM. They have temperatures of $\sim$80 K and densities around $\sim$ 3x10^7 m^{-3}. These clouds are small, just a few parsecs in diameter, and only contain a few solar masses. Surrounding these small H I regions is warm material composed of atomic, H I, and ionized, H II, hydrogen at about $\sim$8000 K, the third component of the ISM. These regions are about 100 times less dense than diffuse clouds, n$\sim$ 3x10^5 m^{-3}. The fourth general component of the ISM is composed of hot, ionized H II gas, with temperatures $\sim$50,000 K and densities $\sim$5000 m^{-3}. In this work, we focus on the region where star formation occurs, in cold, dense molecular clouds.

1.2. STAR FORMATION

Star formation begins when portions of the slowly rotating molecular cloud start to clump, forming dense cores. Eventually, a dense core will accrete enough matter that it surpasses a critical mass, and it will begin collapsing under its own gravity, forming a higher density region at the center and a lower density envelope. The dense core continues to contract and matter continues to fall toward the center of the system from the envelope. As the radius of the dense core becomes smaller, the core will rotate faster, conserving angular momentum. Imagine looking at the envelope from the side. In general the material in the envelope moves past you in a horizontal direction as it rotates about a vertical axis. However, there will still be some particles with a vertical motion. As particles moving upward collide

with those moving downward, they lose some of their momentum in the vertical direction. However, since as a whole those particles are still rotating around that vertical axis, their horizontal component of momentum does not change much. This causes the material to flatten into a disk. Gas and dust continue to accrete onto the disk and protostar, and interactions between the spinning protostar and infalling material cause outflows of gas along the axis of rotation. As the envelope dissipates from collapse onto the disk, collisions within the disk may start to form planets. Eventually stellar winds from the protostar or outflows, along with collisions in the disk, remove a large portion of the gas and dust leaving a young star with a planetary system.

1.3. TYPES OF STAR FORMING REGIONS

Stars can form individually, in pairs, or in clusters from a molecular cloud. However, work by Carpenter et al. (2000), Lada and Lada (2003), and Porras et al. (2003) indicates that stars are more likely to form in clusters. Whether formed in isolation or in clusters, the stars in each molecular cloud vary in size, so there are regions of low-mass and mixed-mass star formation. The Taurus Molecular Cloud (TMC) is an example of a low-mass star forming region. It is about 140 pc away (Kenyon et al., 1994) and at least some of its stars are formed in isolation, with little influence from their neighbors (Adams, 2010). In contrast, the Orion star forming region, at approximately 414 pc (Menten et al., 2007), is known to have areas of high mass star formation and clusters of star formation (Adams, 2010), and therefore would be a region with both low-mass and high-mass star formation. Finally, Rho Ophiuchi is also a mixed-mass star forming region that most likely lies between 120-145 pc away (see Wilking et al. (2008) for a discussion). However, while this region contains many low mass stars, it is influenced by nearby young, intermediate-mass, B stars rather than massive O stars. Its natal environment could have an impact on a forming star. For example, since massive stars have shorter lifetimes than low-mass stars, it is possible that a nearby massive star at the end of its life which becomes a supernova could provide heavy elements that may be incorporated into the envelope surrounding a nearby low-mass star. TIt is therefore interesting to compare the composition of regions where stars form in

isolation with regions influenced by massive star formation or intermediate mass star formation.

1.4. STAR FORMATION CLASSIFICATION

In order to draw general conclusions about star formation, the process is divided into several stages. An object's stage, or evolutionary status, is determined from its Spectral Energy Distribution (SED). The youngest objects are Class 0 (André et al., 1993). At this stage, the object is simply a dense core surrounded by an envelope, with most of the mass contained in the envelope. Accretion is occuring from the envelope onto the central star, and bipolar outflows occur along the axis of rotation. In fact, these outflows from a "sourceless" object led to the addition of class 0 sources (Bachiller, 1996). The spectrum of these objects consists of radiation from the dust in the far infrared or millimeter portion of the electromagnetic spectrum; there is no contribution to the spectrum from the forming protostar. The next stage consists of objects with a Class I SED. These objects are still deeply embedded, but accretion of the envelope onto the central star and forming disk has decreased. If planet formation is present, it could be in its early stages here. Outflows are present along the axis of rotation. Very little radiation from the protostar reaches the observer, but this is dependent on the orientation. If the object is oriented edge on, so that the observer is looking through mostly envelope and disk, the stellar radiation will be absorbed by the dust. However, if the line of sight is oriented along the axis of the outflow where there is little dust, more stellar radiation can reach the observer. The spectra of these objects results mainly from the dust, and peaks in the mid-infrared. Eventually, the disk dominates over the infalling envelope, and the young star becomes visible. At this stage, the SED of the YSO is referred to as Class II. The observed spectrum peaks in the near infrared, and consists of an infrared excess due to the disk superposed on a blackbody from the star. Material is still accreting from the depleted envelope onto the disk and central star, and thus outflows are still present. Objects at this evolutionary state are known as Classical T-Tauri Stars (CTTS). The last stage before the star moves on to the main sequence produces a Class III SED. Young stars at this stage are known as Weak-Emission

T-Tauri Stars (WTTS). At this point, there is very little envelope remaining, and the process of clearing the disk is prominent. If planets are present at this stage, they would encounter heavy bombardment. This study focuses on objects in the Class I/II stages, where the envelope provides protection for ice formation and chemistry in the disk is occurring.

1.5. FORMATION OF ICES

The first part of this study focuses on the formation of ice mantles on grains in the envelope surrounding YSOs. The idea that ices are present in the ISM is not new. They were proposed as constituents of interstellar grains (see for example Lindblad (1935) and Eddington (1937)). Oort and van de Hulst (1946) developed a theoretical model for ice nucleation and growth in interstellar clouds, which was widely accepted in the 1950s and early 1960s because it explained the observed properties of the dust. van de Hulst (1946) suggested that H_2O, CH_4, and NH_3 were formed when O, C, and N interacted with H on grains composed of dust and ice. Further, in 1951, Bates and Spitzer (1951) suggested that the grains were not composed of ices, but that the ices were catalyzed by the cold surfaces of the silicate and carbon-based dust grains. It was not until 1973 that observations confirmed Bates' theory, when Gillett and Forrest (1973) found a strong absorption feature at 3.1 μm toward the Becklin-Neugebauer object and attributed it to H_2O ice. To date, over 40 features have been found in the solid state on grains (van Dishoeck, 2004), including those due to H_2O, CO_2, CO, CH_3OH, CH_4, HCOOH, NH_3, and H_2CO.

In order to understand how ices can form on grains, we must first consider the mechanisms required for a molecule to stick to the grain. There are two such mechanisms for adsorption, chemical and physical. Physical adsorption is dominated by van der Waals forces, and has a binding energy of about one tenth the binding energy for chemical adsorption (Whittet, 2003). In molecular clouds, physical adsorption dominates. The rate of adsorption depends on the mean speed of the particle, radius of the grain, and the number density of the gas. The probability of adsorption, known as the sticking coefficient, ζ, depends on the temperature of the gas and dust. In a hot gas, the sticking probability is

low, but at the cold temperatures of interstellar clouds it is close to 1. Whittet (2003) estimate that the adsorption time for 0.1 μm grains in dense clouds with a number density, $n_H \sim 1x10^8$ m^{-3} is about nine minutes. Because it is is much more abundant than other atoms, hydrogen is the most abundant atom to stick to the grain. It is also the most efficient at migrating on the grain because of its binding energy. This is important for the formation of molecular hydrogen, H_2, which releases 4.48 eV when formed (Whittet, 2003). This exothermic binding energy prevents the formation of molecular hydrogen in the gas phase; since two hydrogen atoms release energy when binding, there must be a third body available to absorb the released energy. The interstellar grain is the important third body necessary for H_2 formation. Figure 1.1, adopted from Whittet (2003), provides an excellent representation of grain surface interactions. In the case of molecular hydrogen formation, incident hydrogren atoms stick to the dust grain, and then migrate until they find another hydrogen atom. Finally, the hydrogen atoms chemically combine and are ejected from the surface from the release of the binding energy.

Similarly, hydrogen can also find O, C, or N during its migration. These atoms are more likely to combine with hydrogen than with another O, C, or N atom because of the mobility of hydrogen. In addition, the CH, NH, and OH that are formed are more likely than H_2 to remain attached to the grain because of their greater mass. This results in the formation of a polar layer of ices, i.e., those rich in hydrogen. These hydrogenation reactions produce molecules such as H_2O, CH_4, NH_3, and perhaps CH_3OH. This process continues until most of the available hydrogen has been tied up by O, C, or N, or formed H_2, although the critical factor is the H_2 formation. Note that this does not mean that non-hydrogenated species cannot form in this layer. In fact, if a non-polar molecule such as CO_2 is trapped in this polar ice matrix, it can stay on the grain at temperatures higher than the sublimation temperature for CO_2. Once H_2 recombination is mostly complete, a second layer of ices is formed on the mantle. This layer consists of O, C, and N combining with each other. This results in an apolar, or hydrogen-poor, layer of molecules that may include CO_2, O_2, and N_2. CO is also found in this layer, but it is formed in the gas phase and freezes out onto the grains rather than resulting from the migration of atoms already frozen onto the grain. If

these layers are formed at a low temperature, they are disordered, or amorphous. Figure 1.2 provides an illustration of molecules found in these layers. Finally, a third component is seen when the ice has been heated, or annealed, and is now ordered, or crystalline.

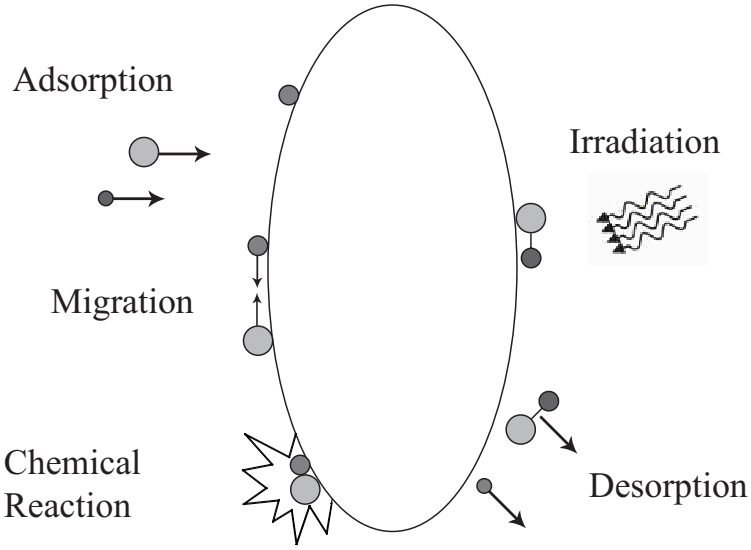

Figure 1.1 Physical and chemical processes on the surface of an interstellar grain. This schematic shows the physical and chemical processes an atom can undergo on the surface of an interstellar dust grain (Whittet, 2003).

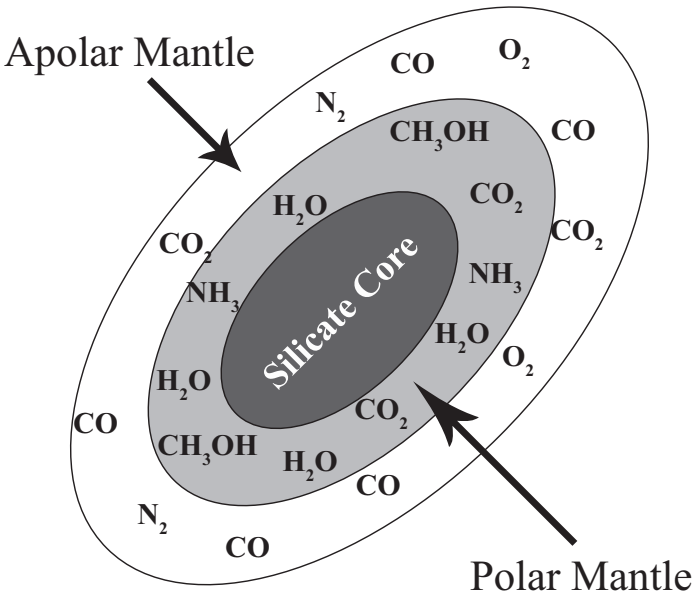

Figure 1.2 Dust grain schematic with ice layers. This schematic from Whittet (2003) shows the silicate dust grain at the center, then a polar layer consisting of mainly of hydrogen-rich molecules such as H_2O, CH_3OH and NH_3 along with a few non-polar molecules such as CO and CO_2 trapped in the ice matrix, and finally an apolar layer with hydrogen-poor molecules such as CO, CO_2, N_2, and O_2.

1.6. ANATOMY OF DISKS

Infalling material from the outer envelope results in the formation of a disk around the forming star. The mass of the disk is much less than that of the star, up to 10% (Whittet, 2003) and has a lifetime of $\sim 10^6$ years (Haisch et al., 2001). There are three main mechanisms that affect the evolution of protoplanetary disks: angular momentum transport, mass infall from the envelope, and stellar winds in the form of outflows (Armitage, 2011). In addition, planet building can affect the evolution in terms of angular momentum transport, and diffusion and mixing are also important. The method of angular momentum transport is particularly unresolved, but leading candidates for a turbulent disk are self-gravitation early in the lifetime of the disk, magnetorotational instability (MRI), and magnetic braking (Armitage, 2011). The geometry of the disk is flared rather than planar, with the thickness increasing with radius from the central star (see Figure 1.3). It

is divided vertically into three regions: a cold midplane, a warm molecular layer, and a surface layer (see Walsh et al. (2010) and Willacy and Woods (2009)). The cold midplane is the densest portion of the disk, and if ices are in the disk, they would be located in this region beyond the sublimation distance. The warm molecular layer is directly above and below the midplane. In this layer simple molecules such as HCN and C_2H_2 exist in the gas phase. Finally, there is the surface layer, which is affected by external radiation from cosmic rays, UV, and X-ray radiation. It is likely that some mixing occurs in these layers, and we expect dust to settle in the midplane (Brittain et al., 2005). The radius of the disk can reach 100s of AU, but is typically found to be about 75 AU (Williams and Cieza, 2011), and the temperature can range from >2000 K at the inner boundary (Dullemond and Monnier, 2010) to 10-20 K at the outer edge (Semenov et al., 2010).

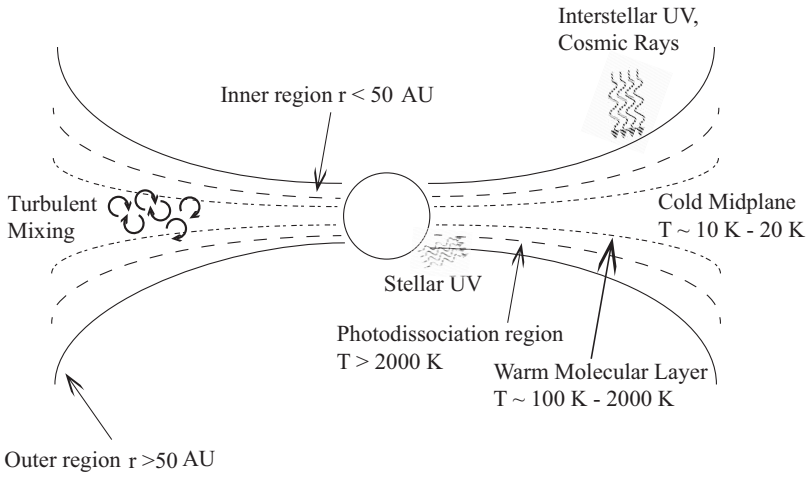

Figure 1.3 Figure showing the geometry of the disk surrounding a YSO adapted from Willacy et al. (2006) and Semenov et al. (2010). Planet formation is generally thought to occur $\leq$30 AU. This disk is divided vertically into a surface layer, or hot dilute atmosphere, a warm molecular layer, and a cold midplane. Numerical models in 1-D (see Willacy et al. (2006) and Semenov et al. (2010)) suggest that turbulent mixing may occur between the warm molecular layer and the cold midplane.

1.7. INFRARED SPECTROSCOPY AS A TOOL

The main tool used to study the chemistry in the envelope and disk at different stages of star formation is spectroscopy. Spectroscopy utilizes the fact that each atom and molecule has a unique fingerprint for absorption or emission, and thus we can determine the composition of the material between an obsever and an object by comparing the observed spectrum with known spectra. Studies of the early processes of star formation use spectroscopy ranging from millimeter wavelengths to near infrared wavelengths, while the later stages are observed at optical and ultraviolet wavelengths.

Many molecules with permanent dipole moments are observed at millimeter wavelengths via their pure rotational transitions. While most molecules have been discovered using their rotational transitions, millimeter spectroscopy has its limitations. For example, rotational transitions obviously exclude solids and symmetric molecules. In addition, the spatial resolution of millimeter observations is limited. Therefore, infrared spectroscopy is used to complement radio observations. Symmetric molecules such as CH_4 and C_2H_2 do not have permanent dipole moments (van Dishoeck, 2004), but do have combined rotational and vibrational (ro-vibrational) modes which occur in the infrared, and the vibrational modes of ices are also in the infrared. The accessibility of these modes, along with the improved spatial resolution of infrared observations, emphasize the importance of using infrared spectroscopy to determine chemical composition in star forming regions.

To date, close to 40 ice absorption features have been detected in the infrared, and can be attributed to vibrational transitions of $\sim$17 molecules frozen onto dust grains (Boogert and Ehrenfreund, 2004). In addition to these vibrational transitions, numerous ro-vibrational transitions of these molecules in the gas phase are found in the infrared portion of the electromagnetic spectrum. These simple molecules are the components of prebiotic molecules such as amino acids (Pontoppidan et al., 2003) and thus are of particular interest. The solid molecules are important diagnostics of the composition of the protostellar cloud and the

thermal history of the grains. We expect to see ices in the envelope surrounding the star or possibly in the midplane (beyond ∼5 AU) of the circumstellar disk where they are protected from the energetic radiation from the forming star. Gas phase molecules are used to determine density, temperature, and kinematic information. These characteristics are used to infer the location of the molecule, which may include the envelope surrounding the YSO, the outer part of the circumstellar disk, the inner portion of the disk, or an outflow associated with the forming star. Molecules in both phases are essential to understanding the organic chemistry of the system.

1.8. TECHNOLOGICAL ADVANCES

Since the first molecule, the methylidyne radical, CH, was discovered spectroscopically by (Swings and Rosenfeld, 1937), many advances in the technology have occurred. Due to strong absorption from the atmosphere, many infrared studies use either space-based or airborne telescopes. Early contributers to infrared astronomy were the Kuiper Airborne Observatory, KAO, (Haas et al., 1995), the Infrared Astronomical Satellite, IRAS[1], and the first Japanese orbiting telescope, the Infrared Telescope in Space, IRTS[2]. The field of infrared astronomy was revolutionized with the launch of the Infrared Space Observatory (ISO) led by the European Space Agency (ESA) in November, 1995 (Kessler et al., 2003). ISO provided the first coverage of the entire 2-200 μm region without the hindrance of our atmosphere. It allowed the first comprehensive study of star formation regions, which radiate predominantly in the infrared. ISO provided observations of a variety of atomic and molecular species, including, atomic, H_2, and HD lines, gas phase transitions of molecules such as H_2O, CH_4, C_2H_2, HCN, and CO_2, polycyclic aromatic hydrocarbons (PAHs), and the vibrational bands of ices, silicates, oxides, carbides, carbonates, and sulfides (van Dishoeck, 2004). The Short Wavelength Spectrometer (SWS) was extremely useful in probing solid state features in molecular clouds. Ice features such as H_2O, $^{13}CO_2$, CO, CH_4, and CO_2 were in the spectral range of the Short Wavelength Spectrometer (SWS), with medium resolv-

[1] *http://irsa.ipac.caltech.edu/IRASdocs/exp.sup/toc.html*
[2] *http://www.ir.isas.jaxa.jp/irts/irts_E.html*

ing power of ∼2000 (van Dishoeck, 2004). The protostars studied with SWS were predominately high-mass, but did include a handful of intermediate mass (van den Ancker (2000), Nummelin et al. (2001), Schreyer et al. (2002)), and low mass YSOs (Boogert et al. (2000), White et al. (2000), Vandenbussche et al. (1999), van den Ancker (2000)). Improved technology and the launch of the Spitzer Space Telescope have allowed for the study of low-mass YSOs.

This study focuses on ices toward $\sim$ 30 low-mass YSOs toward the Rho Ophiuchi dark cloud and simple molecules found in the gas phase toward the binary system GV Tau. In § 2 we will describe the instruments used to take observations, those observations, and reduction techniques. In § 3 we discuss in detail the results for ice absorption, the analysis of those results is presented in § 4. The results and analysis of the gas analysis will be discussed in § 5. Finally, we will conclude with a discussion about the importance of the gas and ice molecules in star formation, what questions remain unanswered, and what further observations should be made to answer those questions in § 6.

2. OBSERVATIONS AND DATA REDUCTION

The success of SWS on ISO showed the feasibility of using infrared spectroscopy to study chemistry in the ISM. Since then, another space-based mission: The Space Infrared Telescope Facility, now known as the Spitzer Space Telescope, has been launched and successfully utilized. In addition, ground based facilities such as SpeX at the NASA Infrared Telescope Facility (IRTF) and the Near-Infrared Spectrograph (NIRSPEC) at the Keck II observatory have provided invaluable ground based data. Current missions such as SOFIA and Herschel and future missions such as the James Webb Space Telescope (JWST) will further develop this field. This study utilizes the Infrared Spectrograph (IRS) on the Spitzer Space Telescope, NIRSPEC on Keck II, and SpeX on IRTF.

2.1. THE INFRARED SPECTROGRAPH ON THE SPITZER SPACE TELESCOPE

2.1.1. Overview. The Spitzer Space Telescope (Werner et al., 2004) is a lightweight structure (∼110 pounds) with a 0.85 m primary mirror (Figure 2.1)[1]. The telescope assembly, except for the mirror mounts, is made of beryllium, an excellent material for infrared telescopes because it cools quickly. A cryostat is attached to the telescope to keep it and its instruments cold, reducing infrared noise. The telescope was launched in 2003 in a trailing earth orbit. There are three instruments with the telescope: the Infrared Array Camera (IRAC), the Multiband Imaging Photometer (MIPS), and the Infrared Spectrograph (IRS). This study uses data taken with the staring mode of the Infrared Spectrograph (IRS, Houck et al., 2004). IRS consists of four modules, two of which are low-resolution and two that are high-resolution. The low-resolution modes, short low and long low (SL & LL), provide a resolving power, $\lambda/\delta\lambda$, of R=60-120 covering wavelengths from 5.2 μm to 38.0 μm. The SL slit has dimensions of 3.5″ x 57″ and 3.7″ x 57″ for the first and second orders, respectively, and the LL has dimensions

[1] *http://ssc.spitzer.caltech.edu/spitzermission/missionoverview/spitzertelescopehandbook/1/*

of 10.5″ x 168″ and 10.7″ x 168″ for the first and second orders, respectively. These modes cover prominent ice features at short wavelengths such as H_2O at 6 μm and the unknown 6.8 μm feature, as well minor constituents such as HCOOH at 5.85 μm and 7.25 μm, CH_4 at 7.67 μm, NH_3 at 9.0 μm, and CH_3OH at 9.7 μm. The high-resolution modes, short high, SH (4.7″ x 11.3″) and long high, LH (11.1″ x 22.3″) provide enough resolving power, R$\sim$600 to distinguish the distinct double-peak structure of pure or annealed CO_2 at 15.2 μm. Together, these modes cover wavelengths from 9.9 μm to 37.2 μm.

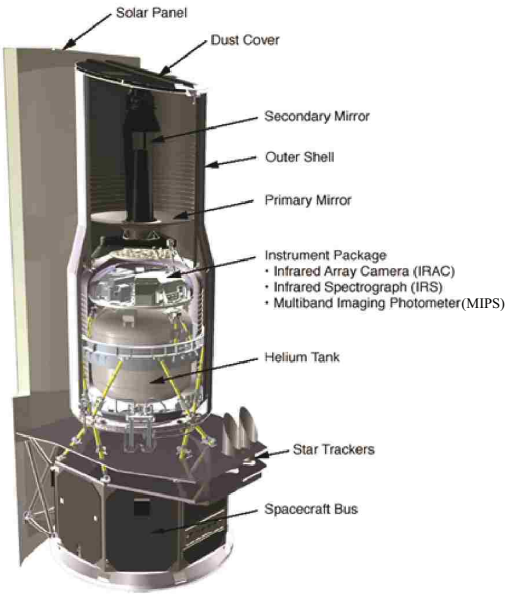

Figure 2.1 Schematic of the Spitzer Space Telescope and its flight system is shown. Lockheed Martin constructed the solar panel and spacecraft while Ball Aerospace provided the Cryogenic Telescope Assembly (CTA). This includes the telescope and cryostat, along with the necessary shields and shells. The instruments were provided by teams led by the Principle Investigators (see Gehrz et al. (2007) for more information).

2.1.2. Spitzer Observations & Reduction. The space-based data were taken using staring mode of the IRS, and analysis included all available modes for each source taken from a comprehensive search of the Spitzer Space Telescope public archive (see Table 2.1). The data were initially processed using

the Spitzer pipeline, version 18.7.0. The Spitzer pipeline flagged cosmic ray hits and corrected for saturated pixels. It also corrected droop, which occurs when subsequent observations accumulate more and more negative charge, and thus appear to "droop." Next, the pipeline dark subtracted the data, removing the baseline noise. Finally, the data were flatfielded to correct for the non-linearity of the detector, and the final basic calibrated data (BCDs) were output. After a proprietary period of six months, during which the primary investigator had sole access, the data were made available through the public archive. We began with those BCDs, first manually cleaning them for cosmic ray hits and hot and cold pixels that were missed in the initial reduction. We used software provided by the Spitzer Science Center (SSC), called IRSClean_mask[2]. The initial "rogue" mask, a mask in which known bad pixels are flagged, was provided by the SSC (see all campaign roguemasks). Next, an extraction program also provided by the SSC, SPICE[3], was used in the "point source regular extraction" mode. The first step created a spatial profile, defining the location of the orders on the detector. This is necessary because the detector is cross-dispersed: the spatial spectrum is split into different columns on the detector (see Figure 2.2). Then, the peak in that profile, the columns on the detector where the flux from the object is greatest, was determined. Each of these steps used a spatial calibration file, resulting in a calibrated wavelength axis. Next, the one-dimensional spectrum was extracted along the trace defined in the previous step. Finally, the data were converted from electrons/sec to Flux density, in Janskys (Jy). This process was repeated for each individual BCD for the source. These BCDs were then stacked, edge effects clipped, and averaged (the median was used for 6 or more BCDs and the mean was used for fewer than 6 BCDs) using SMART (Higdon et al., 2004). In some cases, mainly the LH mode, it was necessary to calibrate between orders. When this was necessary, before the average of the BCDs was calculated, overlapping pixels in the two adjacent orders were averaged and the data scaled to the shorter wavelength order. The modes were calibrated, if necessary, using the same method as above, and then combined producing the final spectrum (for example see Figure 2.3).

[2] $http://irsa.ipac.caltech.edu/data/SPITZER/docs/dataanalysistools/tools/irsclean/$
[3] $http://irsa.ipac.caltech.edu/data/SPITZER/docs/dataanalysistools/tools/spice/$

Table 2.1. Spitzer observations.

Source	RA	Dec	AOR	Modules*	Itime (s)
ISO-Oph 29	16 26 21.42	-24 23 6.4	12699392	SL	12.58
			5647616	SH/LH	62.92/58.72
ISO-0ph 65	16 26 44.2	-24 34 48.3	12699136	SL/LL	12.58/12.58
			5647616	SH/LH	62.92/58.72
ISO-Oph 76	16 26 53.47	-24 32 36.2	12693504	SL/LL	88.08/243.8
ISO-Oph 77	16 26 54.29	-24 24 38.2	12693504	SL/LL	88.08/243.8
ISO-Oph 90	16 26 59.17	-24 34 58.8	4899072	SH	377.5
ISO-Oph 92	16 27 2.34	-24 37 27.2	4902912	SH	125.84
ISO-Oph 99	16 27 5.4	-24 36 31	12697600	SL/LL	29.36/62.92
ISO-Oph 108	16 27 9.43	-24 37 18.8	12699648	SH/LH	12.58/12.58
			4899328	SH	37.74
ISO-Oph 112	16 27 11.1	-24 40 46	12698880	SL/LL	12.58/12.58
			9829888	SH	125.84
ISO-Oph 114	16 27 11.71	-24 38 32.1	12692992	SL/LL	12.58/125.84
			14493184	SL/LL	704.66/868.24;572.54
			9829888	SH/LH	125.84/58.72
ISO-Oph 119	16 27 12.9	-24 24 53	12697600	SL/LL	29.36/62.92
ISO-Oph 120	16 27 15.45	-24 26 39.8	12698368	SL/LL	12.58/29.36
WL-20S	16 27 15.88	-24 38 42.9	25932544	SH	188.74
WL-20W	16 27 15.69	-24 38 43.4	9829888	SH	125.84
			12698880	SL	12.58
ISO-Oph 124	16 27 17.5	-24 28 56.3	12698880	SL	12.58
			5647616	SH/LH	62.92/58.72
ISO-Oph 125	16 27 18.3	-24 28 54	10727168	SH	1462.76
			12694784	SL/LL	12.58/243.8
			14492928	SL/LL	352.32/587.22
ISO-Oph 132	16 27 21.7	-24 41 43	12699648	SL/SH	12.58/12.58
			5647616	SH/LH	62.92/58.72
ISO-Oph 134	16 27 21.8	-24 29 53.4	12698880	SL/LL	12.58/12.58
			22350592	SH	731.4
			5647616	LH	58.72
ISO-Oph 137	16 27 24.8	-24 41 3	9346048	SL/SH/LH	29.36/243.8/967.3
ISO-Oph 139	16 27 26.29	-24 42 46.1	12689664	SL/LL	58.72/125.84
ISO-Oph 141	16 27 27	-24 40 52	12699648	SL/SH/LH	12.58/12.58/12.58
ISO-Oph 143	16 27 27.9	-24 39 32	12699648	SL/SH/LH	12.58/12.58/12.58
ISO-Oph 144	16 27 28.4	-24 27 21.9	12698624	SL/LL	12.58/12.58
			12664320	SH/LH	125.84/243.8
ISO-Oph 145	16 27 29.41	-24 39 17.0	12698624	SL/LL	12.58/12.58
			22348800	SH	365.7
			28247070	SH	503.36
			28247296	SH	503.36
			31618048	SL	44.03
ISO-Oph 147	16 27 30.18	-24 27 43.4	12698624	SL/LL	12.58/12.58
			5647616	SH/LH	31.46/58.72
ISO-Oph 154	16 27 32.9	-24 32 36	12692736	SL/LL	29.36/125.84
			10728448	SH	975.16
ISO-Oph 161	16 27 37.2	-24 42 38	12698624	SL/LL	12.58/12.58
ISO-Oph 167	16 27 39.83	-24 43 15.1	12699648	SL/SH/LH	12.58/12.58/12.58
			9829888	SH/LH	125.84/58.72
WLY 2-63	16 31 35.53	-24 1 28.03	12676608	SL/SH/LH	12.58/12.58/12.58
			9827840	SH/LH	62.92/29.36
ISO-Oph 204	16 31 52.2	-24 56 13	12704256	SL/LL	12.58/12/58
			12664064	SH/LH	62.92/121.90
ISO-Oph 209	16 32 1	-24 56 44	12704000	SL/SH/LH	12.58/12.58/12.58

*Note: For the SL and LL modes, there are two orders which are observed independently. With the exception of ISO-Oph 114, the time listed is the same for each order in that mode. For ISO-Oph 114, the integration times for orders 1 and 2 of the LL mode are separated by a semi-colon.

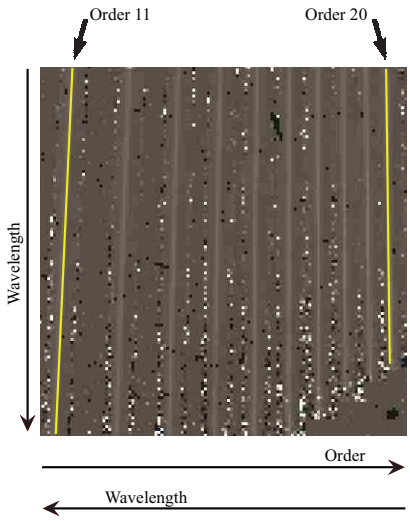

Figure 2.2 A raw frame from the cross-dispersed SH mode is shown. The spectrum is split with an echelle grating into ten orders on the detector. A line is drawn through the left-most and right-most orders for clarity. Thus, instead of a long detector with a short width with one column of data, a square detector can be used. The orders increase to the right the detector, and the wavelength decreases down and to the left. The bright and dark squares are hot or cold pixels, or cosmic ray hits.

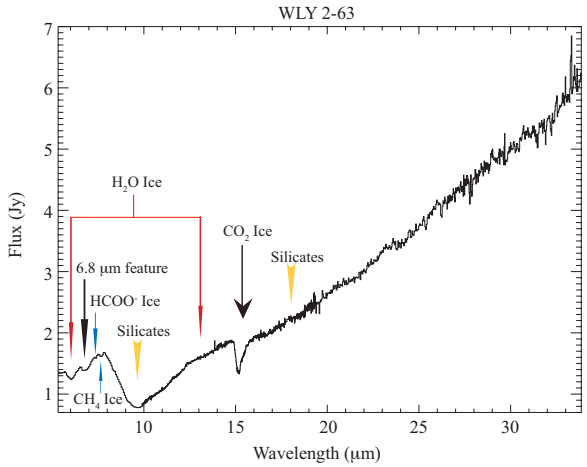

Figure 2.3 The fully extracted spectrum for WLY 2-63 using the reduction methods described above. Note the H_2O bending mode at 6 μm, the unknown feature at 6.8 μm, and the CO_2 bending mode at 15.2 μm. The minor species, HCOO- at 7.40 μm and CH_4 at 7.7 μm, are also visible. The libration mode of H_2O at 13 μm is blended with silicates at 9.7 μm and 18 μm.

2.1.3. Analysis of Spitzer Ices. The analysis of ices consisted of calculating the optical depth for the source, fitting laboratory spectra to the data, and then finding the column density of each molecule along a particular line of sight. The intensities of the final spectra, I (Fig 2.3), were used to calculate the optical depth profiles using:

$$\tau = -ln(\frac{I}{I_o}) \tag{1}$$

where I_o is the intensity of the continuum (see §2.1.4 and §2.1.5). Once the optical depth was calculated, we determined the temperature of the ice and its composition using laboratory spectra as described in Gerakines et al. (1999), Nummelin et al. (2001), and Gibb et al. (2004), with various combinations of molecules at different temperatures from several laboratory databases (see for example Ehrenfreud et al. (1999), Gerakines et al. (1995), Gerakines et al. (1996), and White et al. (2009)). A least squares fit was conducted that covers all the ice mixtures and temperatures, and we performed a two or three component fit to find the best χ^2 match to our data. We used a combination of the scaled laboratory profiles to find the column density, N (Equation (2)), by integrating over the ice feature and dividing by the band strength, or integrated cross section, of the transition, A_i (see Table 2.2 for the values used in this paper).

$$N = \frac{\int \tau d\nu}{A_i} \tag{2}$$

Table 2.2. Band strengths.

Feature	Wavelength (μm)	Band Strength, A (cm/molecule)	Reference
H_2O	3.05	$2.00\text{x}10^{-16}$	Hagen and Greenberg (1981)
H_2O	6.0	$1.20\text{x}10^{-17}$	Gerakines et al. (1995)
HCOOH	5.85	$6.7\text{x}10^{-17}$	Maréchal (1987)
H_2CO	5.74	$9.6\text{x}10^{-18}$	Schutte et al. (1993)
H_2O	13.0	$3.10\text{x}10^{-17}$	Gerakines et al. (1995)
CO_2	15.2	$1.10\text{x}10^{-17}$	Gerakines et al. (1995)

2.1.4. Continuum Determination of the Bending & Libration Modes of H_2O. Due to the lack of continuum in the 5-20 μm region, the continuum determination for the H_2O ice modes is non-trivial. This region has a complex of broad, blended absorption features overlapping the 5-8 μm region, silicates at $\sim$ 9.7 μm and 18 μm, and the CO_2 ice absorption on the red wing of the H_2O libration mode at 13 μm (Figure 2.3). In order to constrain the the continuum between 5-25 μm, we adopted the method of Boogert et al. (2008) to remove the 9.7 μm silicate feature. A third order polynomial was used to remove the continuum from a spectrum of GCS 3I obtained by Gibb et al. (2004). Then, the spectrum was scaled such that the peak depth of the 9.7 μm silicate feature matched the peak depth of the object spectrum. This was an iterative process in which a scale factor was applied, the scaled spectrum subtracted from the object, and a third order polynomial was fit to the modified object spectrum. The sum of the polynomial and scaled GCS 3I spectrum was overplotted on the original object data in order to gauge the validity of the fit. The scale factor was adjusted accordingly, until a visual match between the peak depth of the silicate features from GCS 3I and the object was obtained. Our main concern was matching the depth of the silicate feature rather than the wings because establishing the true continuum level is important for the analysis of the ice features, and the region around the maximum depth reaches continuum in the absence of 9.7 μm silicate absorption. There is continuum between the 6 μm and 13 μm H_2O feature from about 9.5 μm-9.7 μm. GCS 3I was chosen because it is composed mainly of amorphous silicates, similar to low mass YSOs (Kemper et al., 2004). The GCS 3I spectrum is not the only silicate model that could be used, and it does not provide a fit that matches the

wings of the silicate feature well. However, it provides a sufficient constraint to the continuum given that it is the dominant absorbing component in that region. The third order polynomial used with this model was fit to the continuum in the regions 5.2-5.7 μm, 9.5-9.7 μm, 23-25 μm, and 28-36 μm (Figure 2.4). It should be noted that the second region extends slightly into the blue wing of the 13 μm H_2O libration mode. However, the absorption in this region is negligible compared to the peak of the absorption.

To check the validity of this fit, a second iteration was performed. Laboratory spectra were used to determine the strength and temperature of the H_2O bending mode at 6.0 μm, assuming pure H_2O (see § 3). The best fit laboratory spectrum was subtracted from the data, providing additional continuum from 5.7-6.3 μm, assuming the contribution from minor species such as H_2CO and HCOOH were negligible, and from 9.7-12.5 μm from the tail of the 13.0 μm water feature. This iterated polynomial was used to further constrain the continuum fit over the 6.0 μm H_2O feature.

In some cases, the object spectrum contained polycyclic aromatic hydrocarbons (PAHs), making the determination of the continuum level difficult. In these cases, a code developed by Smith et al. (2007), PAHFIT, was fit to the spectrum after the CO_2 ice and the initial estimate for H_2O ice were removed. This model reconstructs the spectrum of the source using atomic emissions, dust features, PAH emission and absorption, and silicate absorption (see Figure 2.5). It also determines the temperature of the star, which can be compared to the spectral type, if known. Once this spectrum was removed from the source, a polynomial was again fit to the continuum. That polynomial was used on the original data to find the optical depth for H_2O.

The continuum determination has the largest affect on the 13 μm libration mode of H_2O. Depending on the continuum fit, the column density for this mode can vary by up to 50%. The column density of the bending mode of H_2O at 6 μm is affected by only about 10%. The spectrum of each source and its final continuum fit are shown in Figure 2.6.

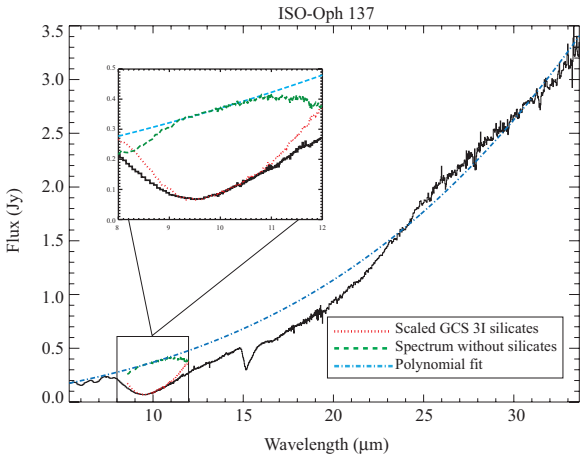

Figure 2.4 The basic method in which a spectrum of GCS 3I is used to model the silicate feature is shown. Note that the primary purpose of this modeling is to find an adequate fit to the depth of the silicate feature so that an additional continuum point is available after removal of the absorption. As such, the model focuses on the depth of the feature rather than the wings. The original spectrum is shown in black with the scaled GCS 3I spectrum as the red dotted line. The green dashed line shows the original spectrum without the silicates. Finally, the blue dot-dashed line represents the resulting polynomial fit to the continnum. The inset simply magnifies the 8-12 μm region for clarity.

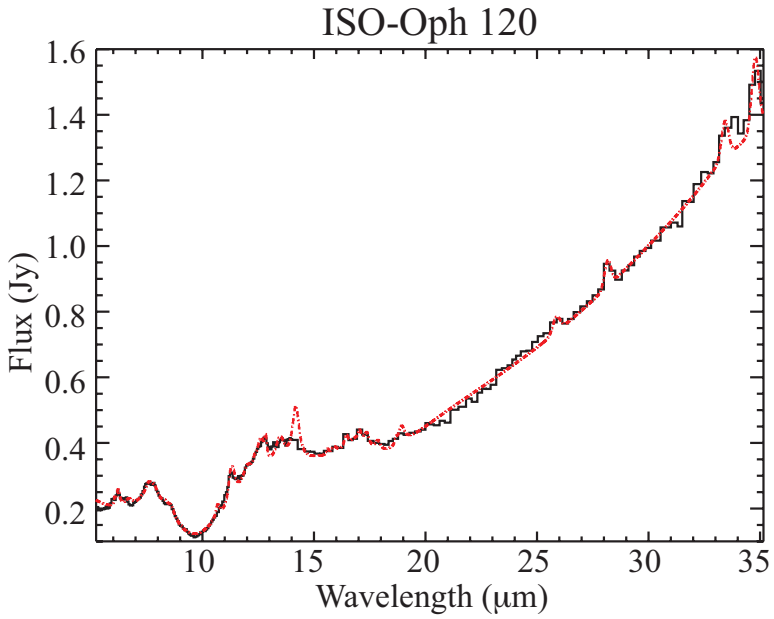

Figure 2.5 As a check for sources containing PAH emission, a PAHFIT spectrum (Smith et al., 2007) was fit to the data after the H_2O and CO_2 ices were removed. This spectrum is shown as the red dot−dashed line along with the spectrum without H_2O in black. Note that the synthetic spectrum matches the observed spectrum quite well from about 6-14 μm, where there is little continnum. Therefore, subtraction of this synthetic spectrum works well to constrain the polynomial fit to the continuum in that region.

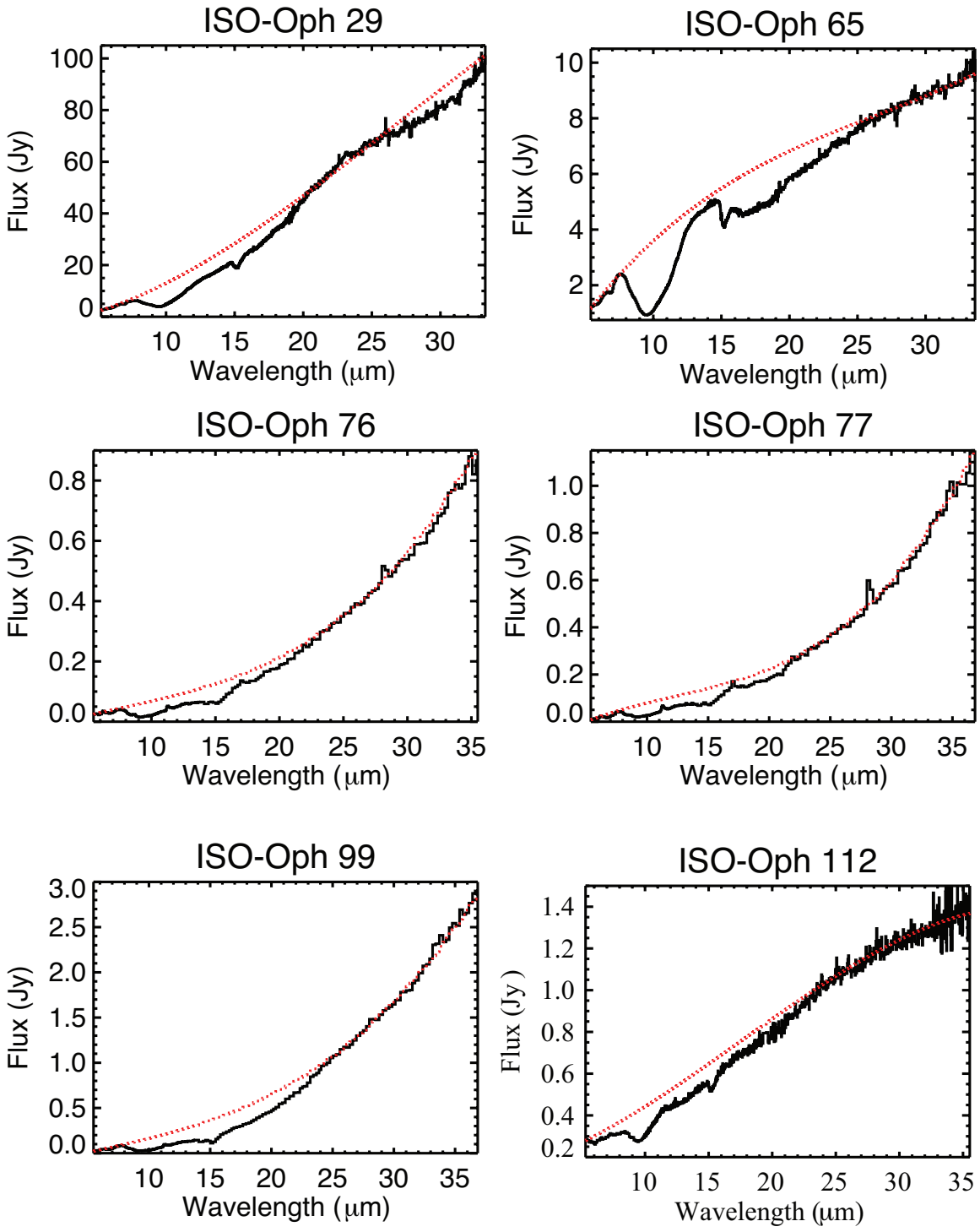

Figure 2.6 This figure illustrates the continuum determination for the 5-30 μm region used to analyze the 6 μm and 13 μm H_2O absorption features. The spectrum of each source is shown in black. The final polynomial fit to the continuum is shown as the red dotted line.

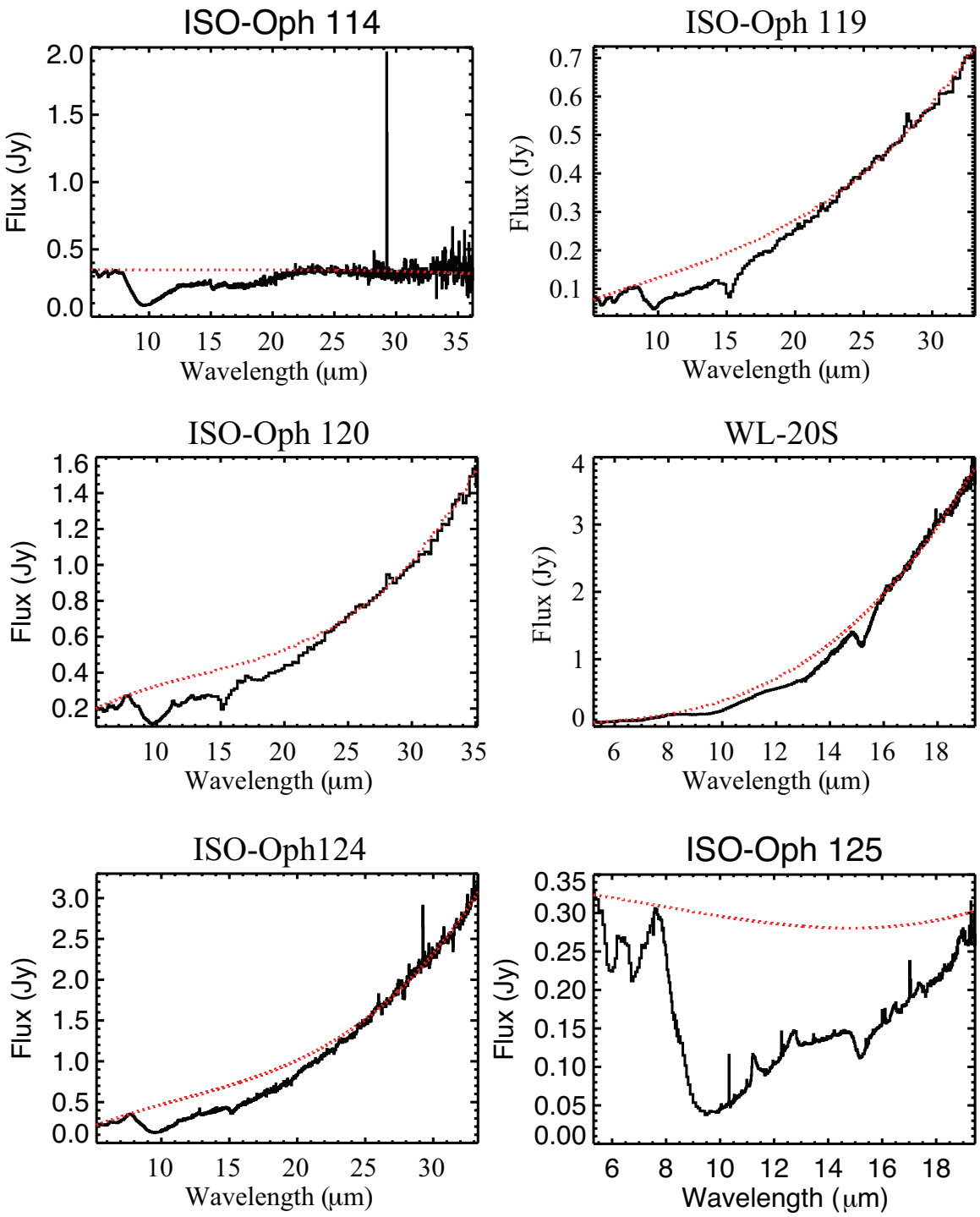

Figure 2.6 This figure illustrates the continuum determination for the 5-30 μm region used to analyze the 6 μm and 13 μm H_2O absorption features. (cont.)

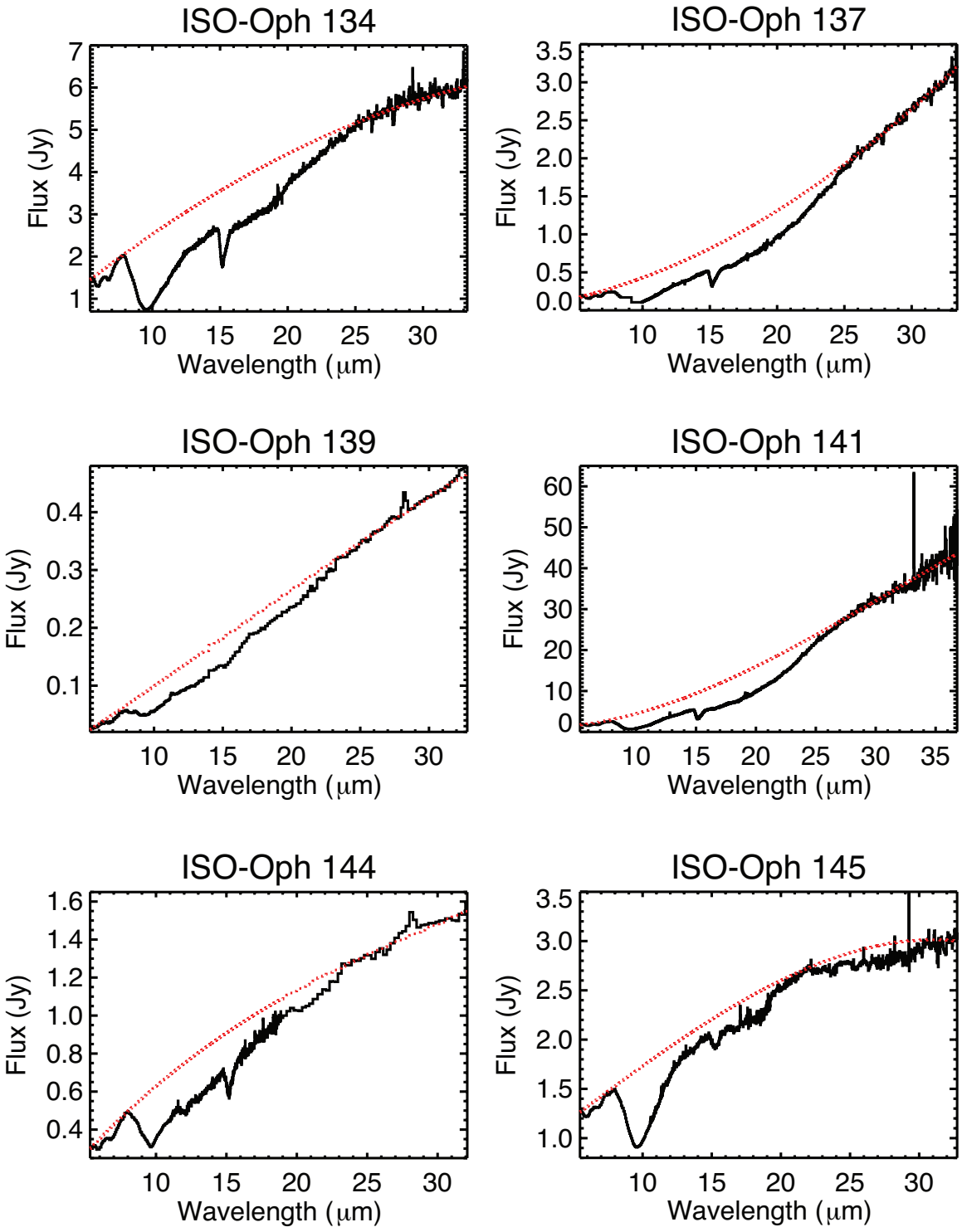

Figure 2.6 This figure illustrates the continuum determination for the 5-30 μm region used to analyze the 6 μm and 13 μm H_2O absorption features. (cont.)

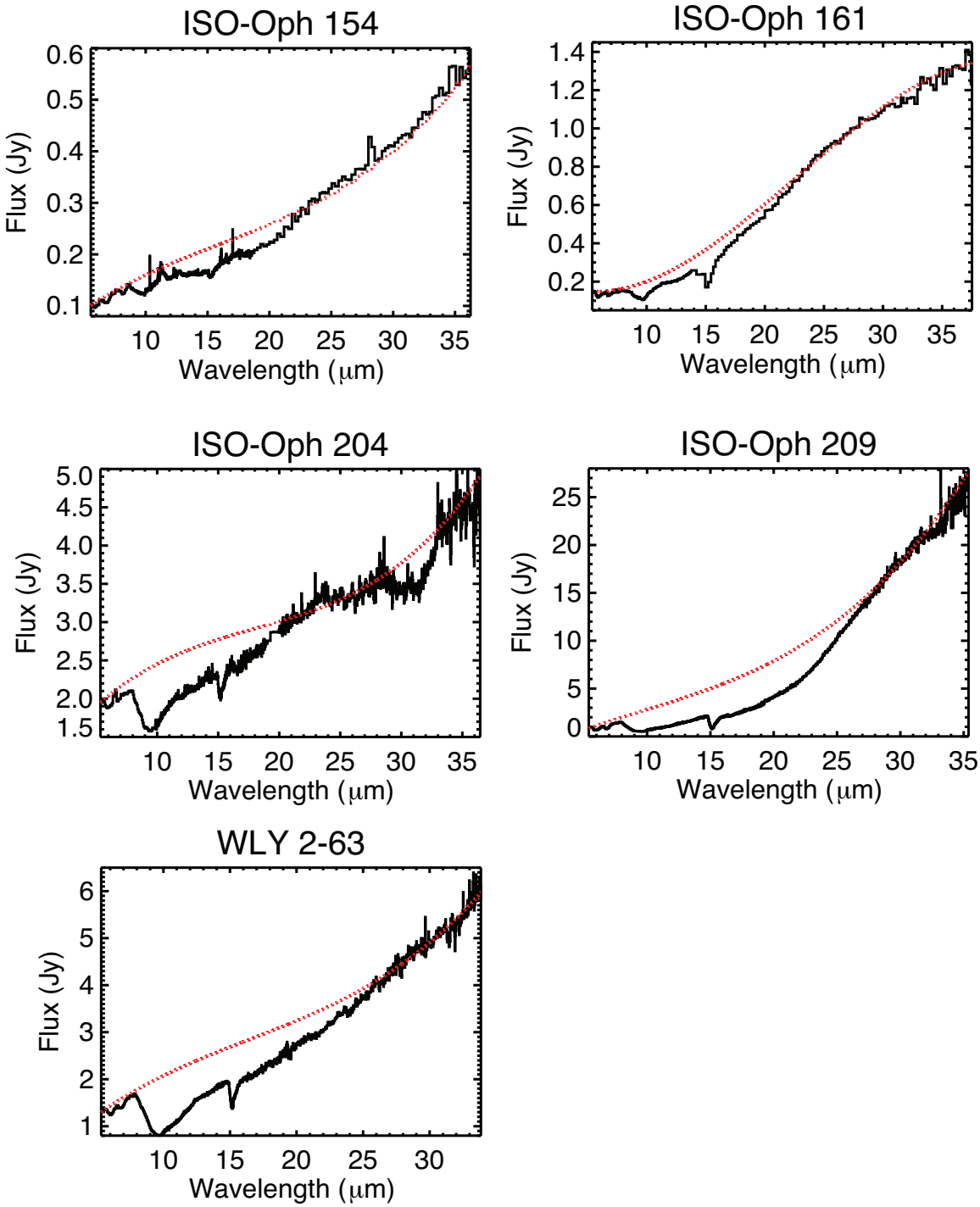

Figure 2.6 This figure illustrates the continuum determination for the 5-30 μm region used to analyze the 6 μm and 13 μm H_2O absorption features. (cont.)

2.1.5. Continuum Determination of the Bending Mode of CO_2. Similarly, the continuum determination for the 15 μm CO_2 bending mode must consider blending with the water libration mode at 13 μm, silicates at 18 μm, and in some cases an absorption of unknown origin at 16.45 μm (see Gerakines et al. (1999) and Pontoppidan et al. (2008)). Thus, a local continuum was used, removing the contamination from the water libration mode and silicates (Figure 2.7a). When present, the 16.44 μm feature was removed using the method by Pontoppidan et al. (2008), which involved fitting a Gaussian with a full width half max (FWHM) of 73 cm^{-1}, centered at 608 cm^{-1} (16.45 μm). Finally, a third order polynomial was fit to the data in the 13.8-14.2 μm, 14.6-15.0 μm, 16.1-16.6 μm, and 17.2-18.0 μm regions (see Figure 2.7b). The 15 μm region of each source with the polynomial or polynomial + gaussian representing the continuum fit is shown in Figure 2.8.

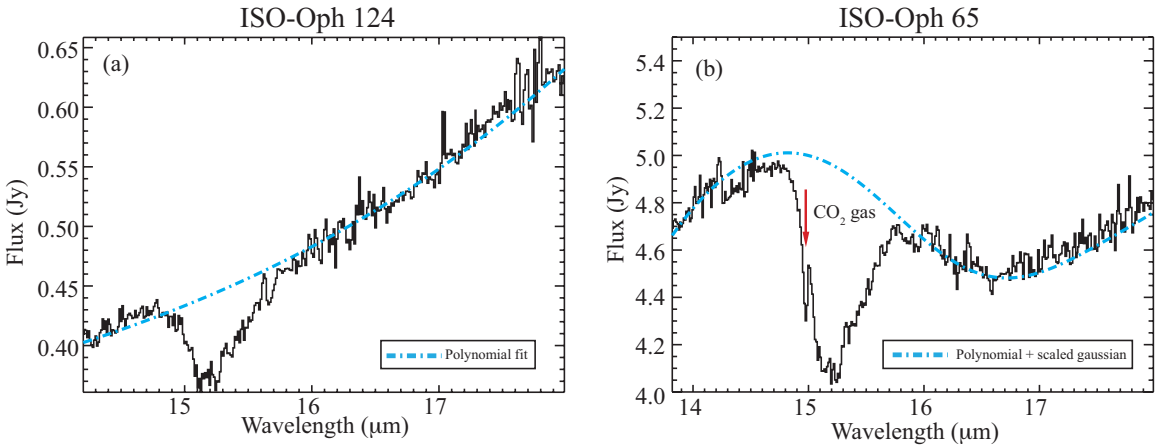

Figure 2.7 Sample spectra show the continuum determination for the 15 μm CO_2 absorption. (a) The solid black line is the extracted spectrum of ISO-Oph 124. The dot-dashed blue line is the third order polynomial fit to the continuum of the YSO. (b) The spectrum of ISO-Oph 65 is the solid black line. Note CO_2 gas absorption at 14.9 μm. The blue dot-dashed line is the third order polynomial fit to the local continuum, plus a gaussian scaled to the 16.44 μm feature. The Gaussian is centered at 608 cm^{-1} (16.45 μm) and has a FWHM of 73 cm^{-1} (Pontoppidan et al., 2008).

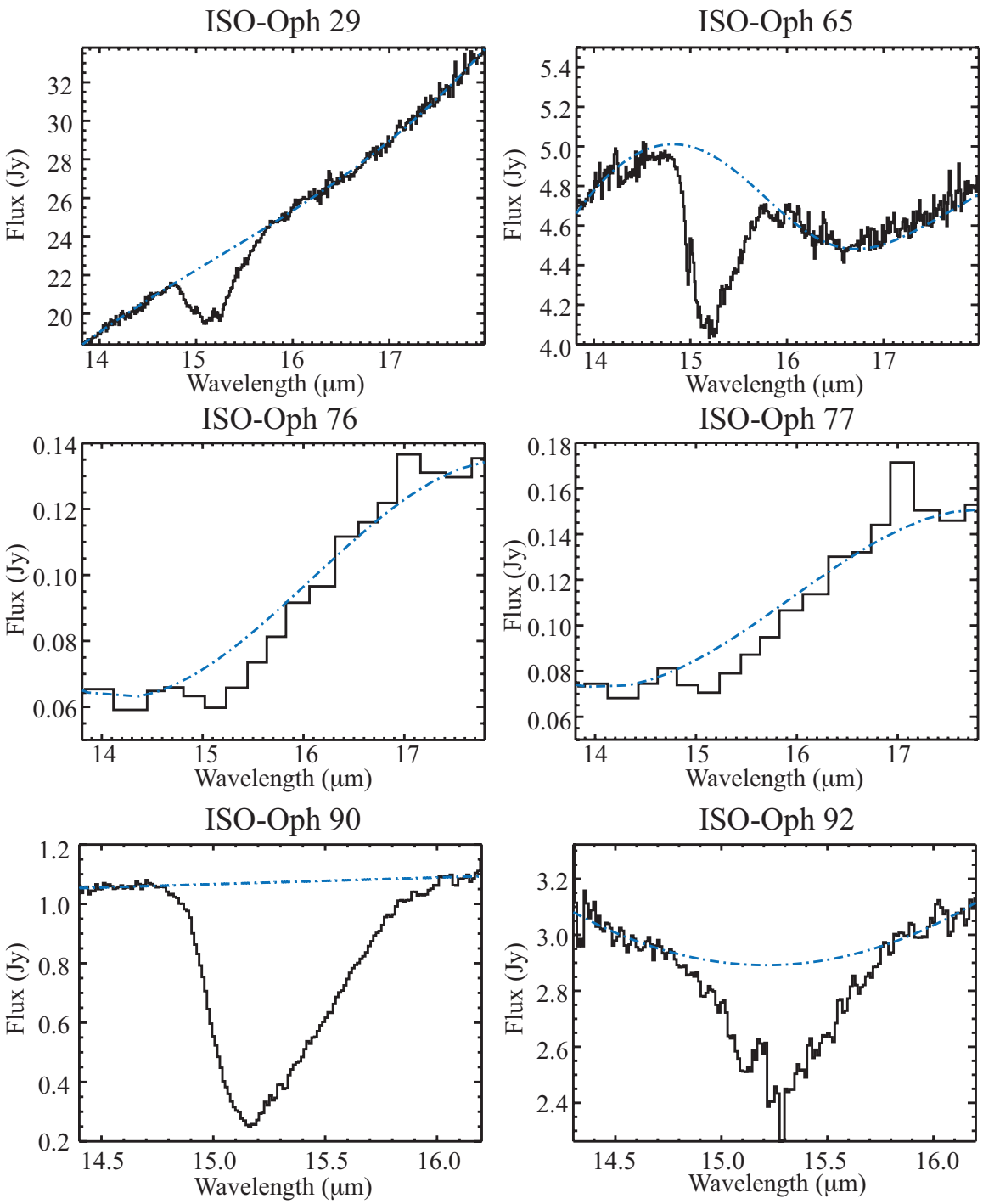

Figure 2.8 This figure illustrates the continuum determination for the 15 μm bending mode of CO_2. The spectrum of each source is shown in black. The final polynomial fit to the continuum is shown as the blue dot-dashed line.

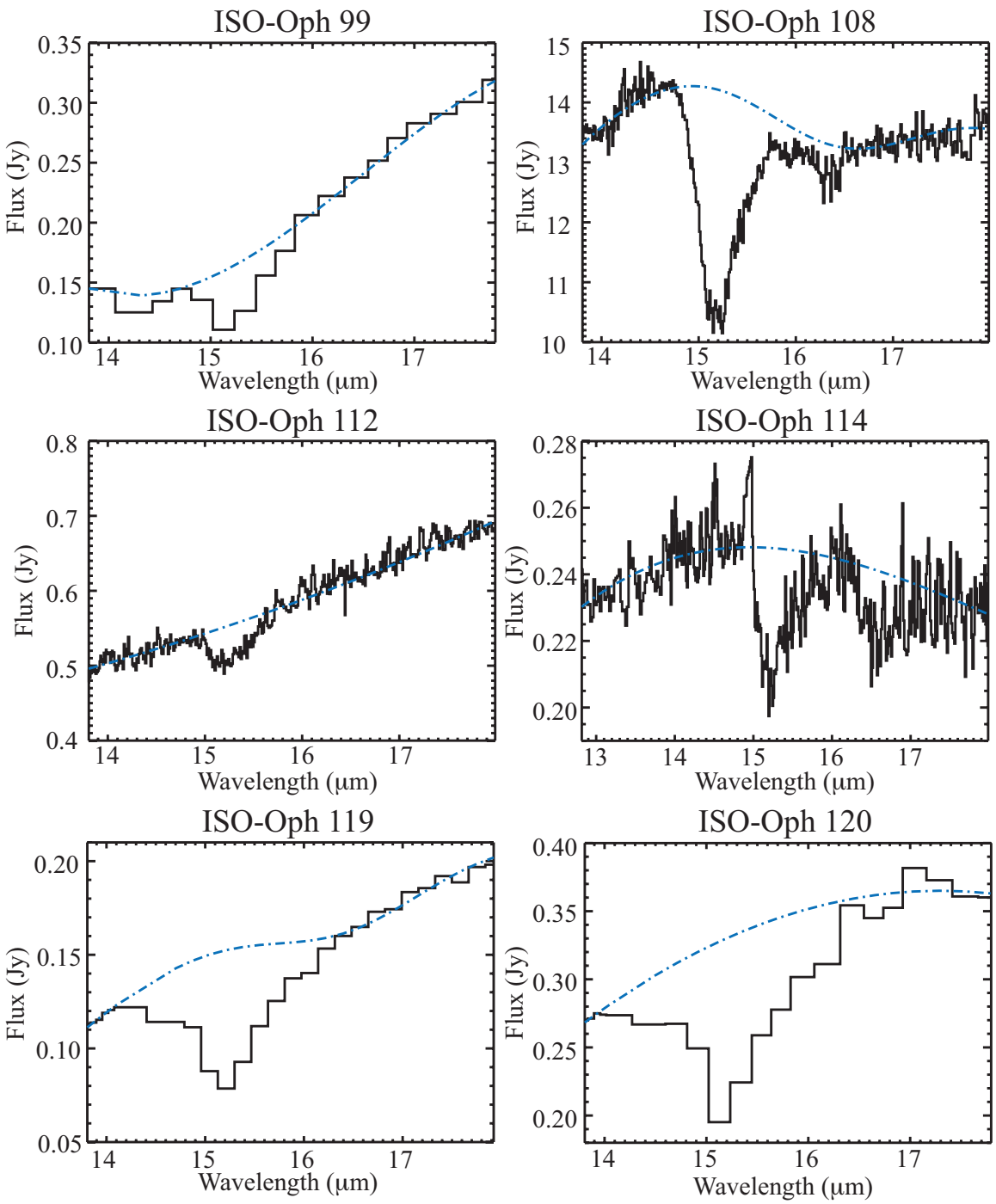

Figure 2.8 This figure illustrates the continuum determination for the 15 μm bending mode of CO_2. (cont.)

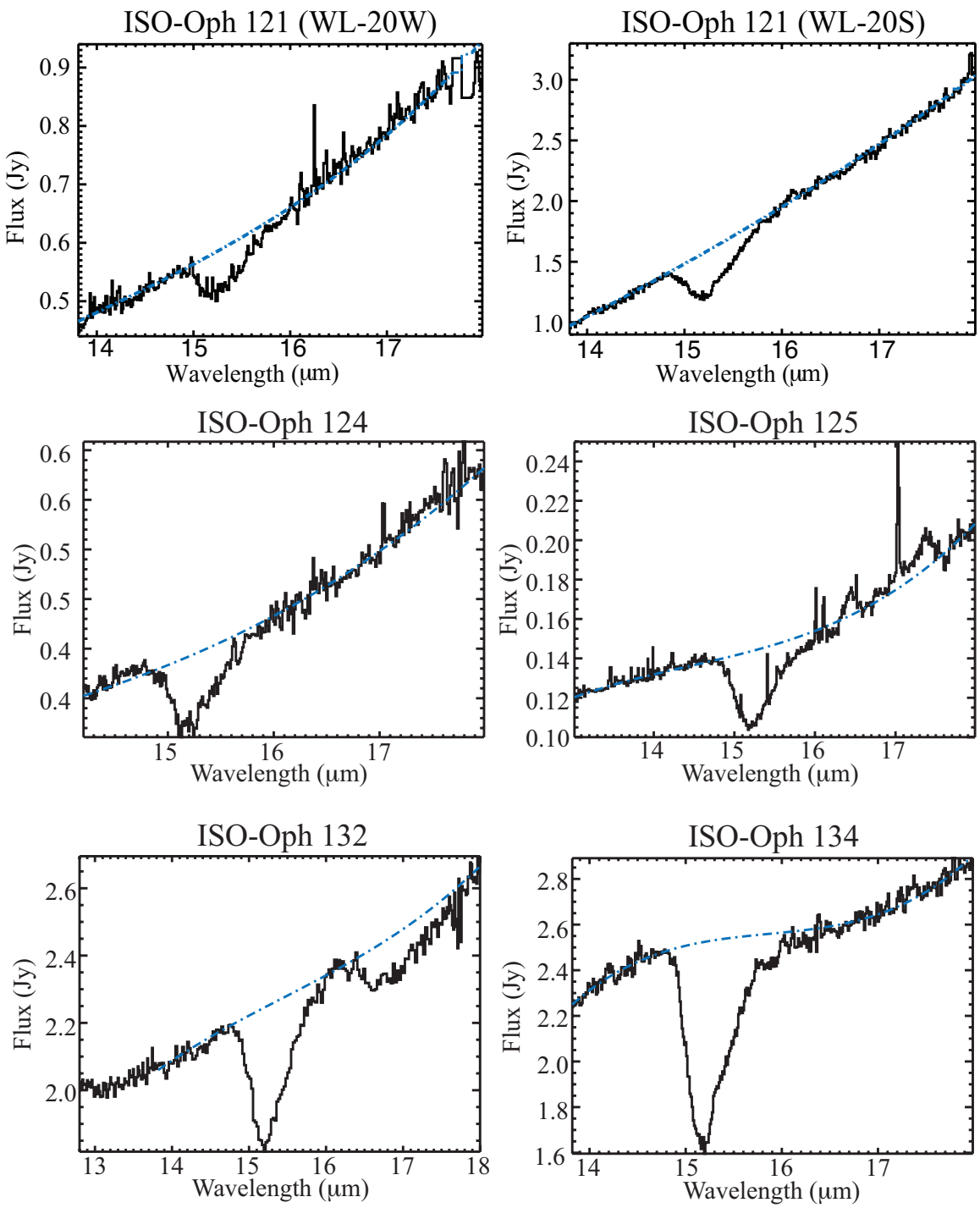

Figure 2.8 This figure illustrates the continuum determination for the 15 μm bending mode of CO_2. (cont.)

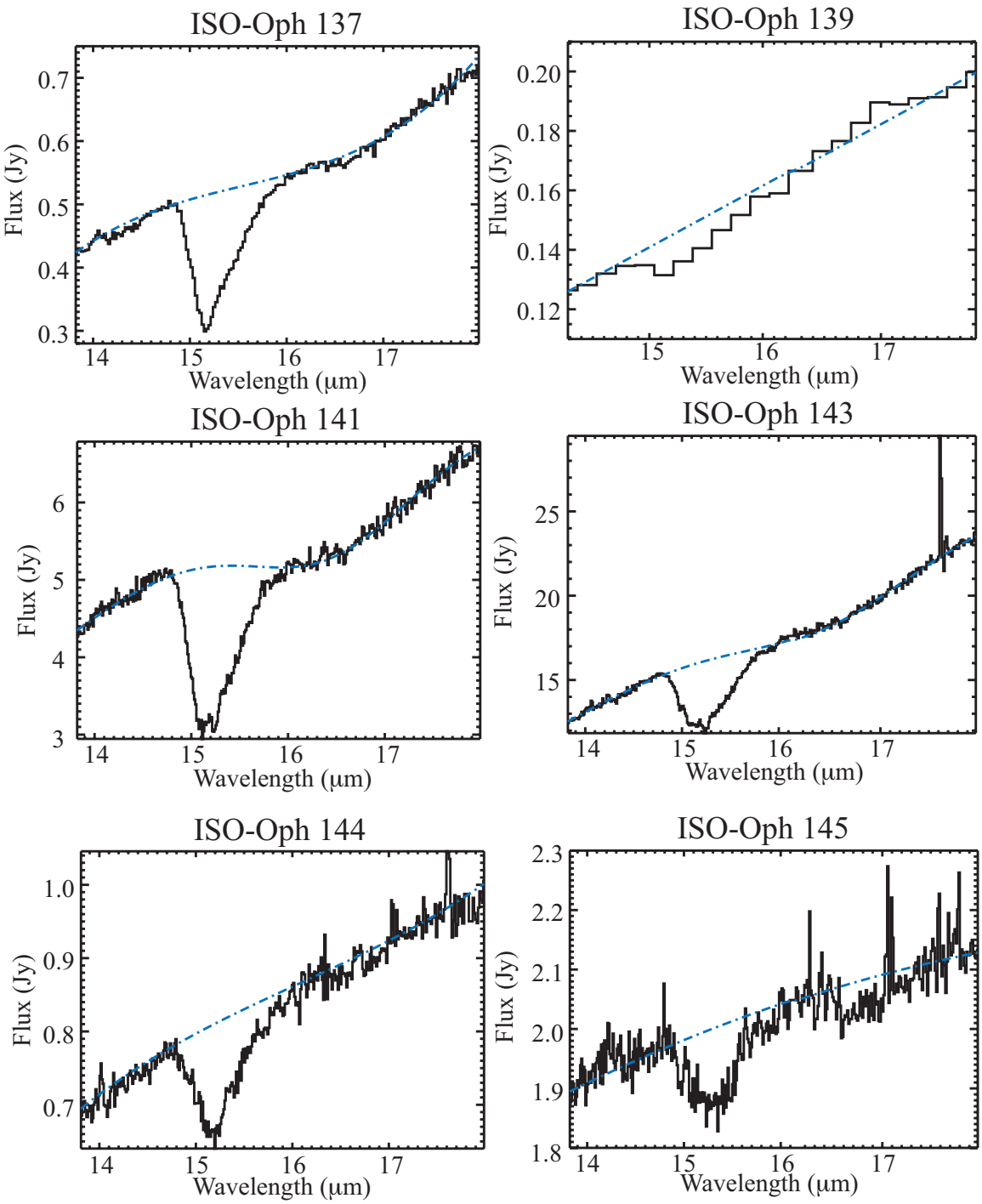

Figure 2.8 This figure illustrates the continuum determination for the 15 μm bending mode of CO_2. (cont.)

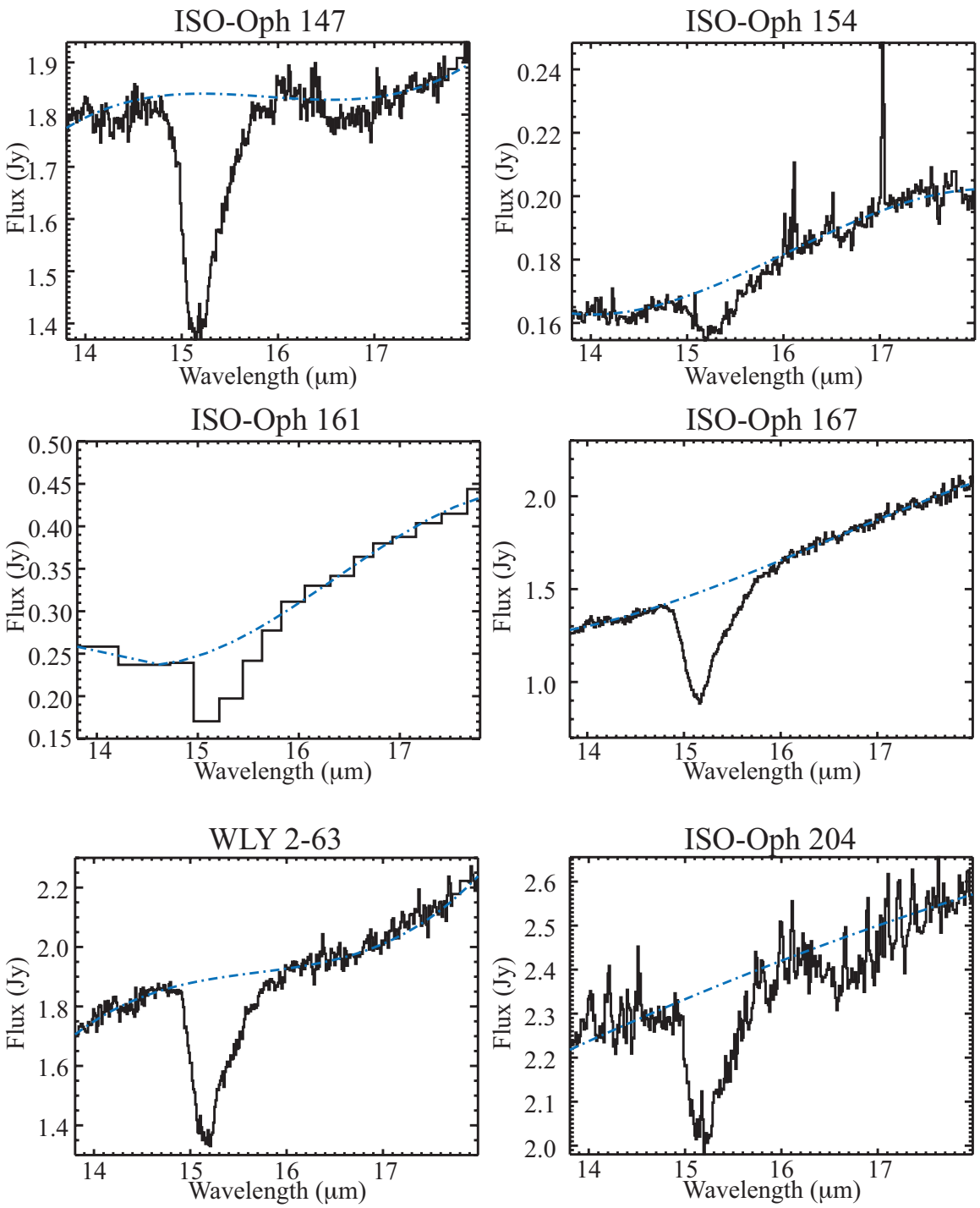

Figure 2.8 This figure illustrates the continuum determination for the 15 μm bending mode of CO_2. (cont.)

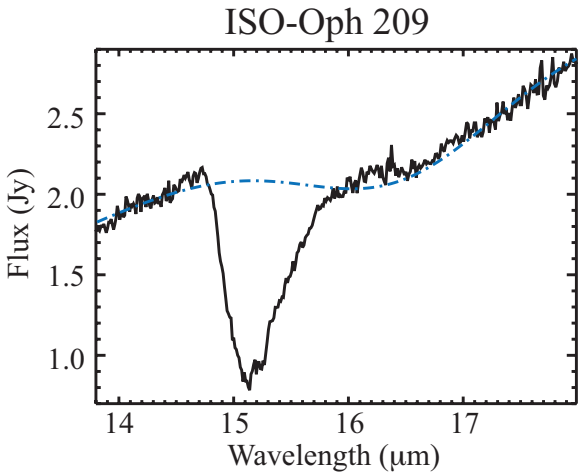

Figure 2.8 This figure illustrates the continuum determination for the 15 μm bending mode of CO_2. (cont.)

2.2. SPEX AT THE NASA INFRARED TELESCOPE FACILITY

2.2.1. Overview. The NASA Infrared Space Telescope Facility, (IRTF) is a small, 3 m, telescope optimized for infrared observations and located at the summit of Mauna Kea, Hawai'i (Figure 2.9). There are several instruments that can be utilized: NSFCAM2, CSHELL, the Mid Infrared Spectrometer and Imager, MIRSI, and SpeX. Our data were taken with SpeX, which is a medium resolution (R = 1000 - 2000) spectrograph that operates from 0.8 μm - 5.5 μm (Rayner et al., 2003). It can be used in seven different modes, SXD (short wavelength cross-dispersed), LXD1.9, LXD2.1, LXD2.3 (long wavelength cross-dispersed with coverage starting at 1.9 μm, 2.1 μm, and 2.3 μm, respectively), Low-resolution, Short single order, and Long single order. The slit width ranges from 0.3″ to 3.0″Ẇe used the LXD2.1 mode with either the 0.5″ or 0.8″ slit, depending on sky conditions. This covers a spectral range of 2.1 μm - 5.0 μm, which includes the stretching mode of H_2O ice at 3.0 μm, the C-H stretching mode of CH_3OH at 3.53 μm, and the stretching-vibration mode of CO at 4.67 μm.

Figure 2.9 This photo shows the IRTF telescope and its support structure. The orange metal structure is the actual telescope assembly and a portion of the instrumentation is at the bottom. The tan pieces on the side are the concrete arms of the mount, and the dome is visible near the top. ©Kari A. Wojtkowski

2.2.2. SpeX Observations & Data Reduction. Data were taken of the Rho Ophiuchi region in June 2006 and June 2008 (Table 2.3) using the standard observation practice of the ABBA pattern. The telescope is nodded (or moved) between two positions, referred to as A and B, located in the top half and bottom half of the slit. Specifically, the telescope starts in the A position, an exposure is taken, then the telescope is nodded to the B position, and a second exposure is taken. Now, instead of moving the telescope back to the A position, another exposure in the B position is taken, and then finally the telescope is nodded back to the A position to finish the sequence. This has the advantage of reducing the amount of time spent moving the telescope. The A and B positions are necessary to remove sky emission. By subtracting the B frame from the A frame, background from the sky and atmosphere is removed, as is shown in Figure 2.10, a critical step needed to produce a spectrum of the object. The data were reduced using software called Spextool, an IDL gui-based package developed by Cushing et al. (2004) to reduce data taken with SpeX. Calibration files were created using darks, flats, and an AB pair, and the data were stacked. Next, the spectra were extracted

Table 2.3. IRTF observations.

Source	RA	Dec	Date	Slit width (")	Itime(s)
ISO-Oph 92	16 27 02.17	-24 37 28.7	June 4, 2006	0.8	1387
ISO-Oph 132	16 27 21.57	-24 41 44.7	June 4, 2006	0.8	2468
ISO-Oph 147	16 27 30.29	-24 27 45.1	June 5, 2006	0.8	4978
ISO-Oph 167	16 27 40.17	-24 43 06.4	June 10, 2008	0.3	1530

and the "A-B" and "B-A" results were combined. Although the calibration files include a sky cancellation to first order, it is still necessary to remove atmospheric absorption lines. This was accomplished using the program xtellcor (Vacca et al., 2003), which is provided as part of the Spextool package. This routine compares the standard star to a high resolution model of Vega in order to remove intrinsic stellar features found in the A0 star, leaving just the black body with instrumental effects. Sky and instrument effects were removed by dividing the object spectrum by the corrected standard spectrum. The object spectrum was then flux calibrated to the standard. Finally, the spectrum was cleaned and smoothed. Areas where the atmospheric transmittance is low were removed (for example from $\sim$2.5 μm - 2.8 μm), and a gaussian with FWHM of the slit width (in pixels) was used for smoothing. A sample final spectrum is shown in Figure 2.11.

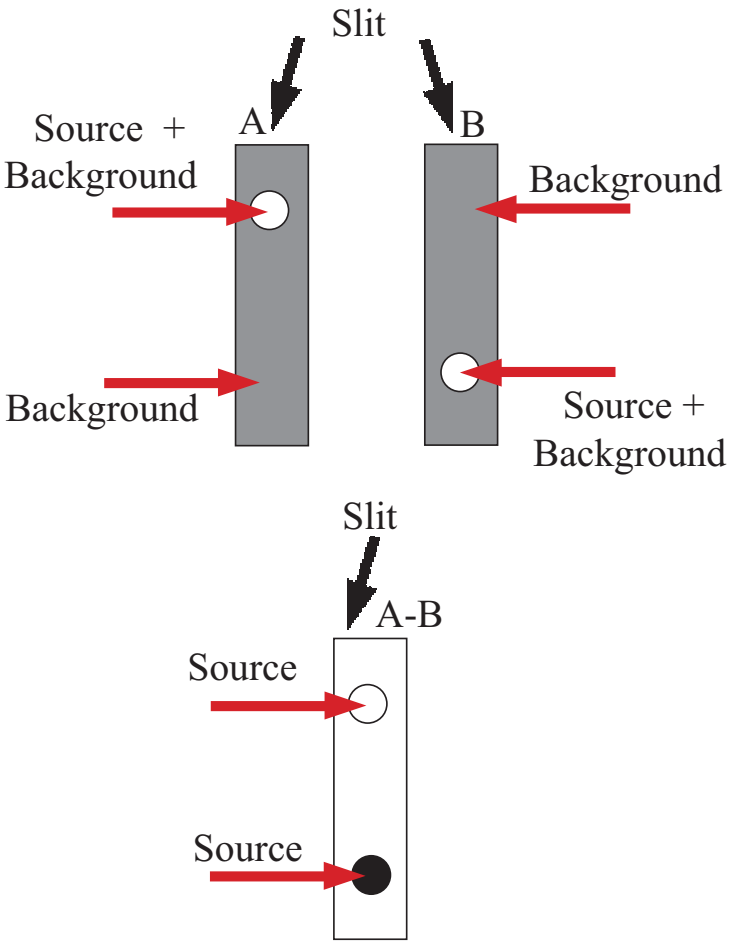

Figure 2.10 This brief schematic illustrates AB pairs and background cancellation. The slit labeled "A" shows the source centered in the top half of the slit with background (sky + atmosphere) throughout. The "B" slit has the source in the lower half of the slit, and with background throughout. The slit at the bottom shows the result of subtraction, A - B, in which the background has been removed, an image of the source is located in the top portion and an inverted image of the source in the bottom portion. This is only a first order correction as the background will vary along the slit. It is still necessary to perform a telluric correction to remove atmospheric absorptions.

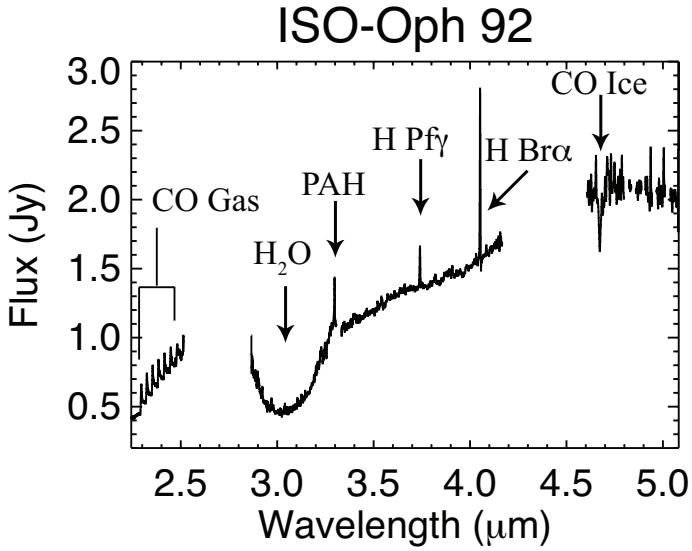

Figure 2.11 The fully extracted spectrum for ISO-Oph 92 using the reduction methods described above. Note the H_2O stretching mode at 3 μm, and the stretching mode of CO at 4.67 μm. PAH emission at $\sim$ 3.3 μm, excited hydrogen at 3.74 μm and 4.05 μm, and the CO overtone lines (v = 2-0) from 2.3 μm - 2.5 μm are labeled.

2.2.3. Analysis of IRTF Ices. We used the same method to analyze the IRTF ices as we did for the Spitzer ices. The first step was to determine the continuum. A polynomial was fit to short wavelengths from about 2.25 μm - 2.3 μm, from 2.45 μm - 2.55 μm (if no CO gas emission was present), longward of the H_2O ice from $\sim$4.0 μm-4.2 μm(excluding the brackett alpha emission line of hydrogen at 4.05 μm), and 4.8 μm - 5.1 μm. There were four Spitzer sources for which we obtained IRTF data. Those spectra with the polynomials fitted to the continuum are shown in Figure 2.12.

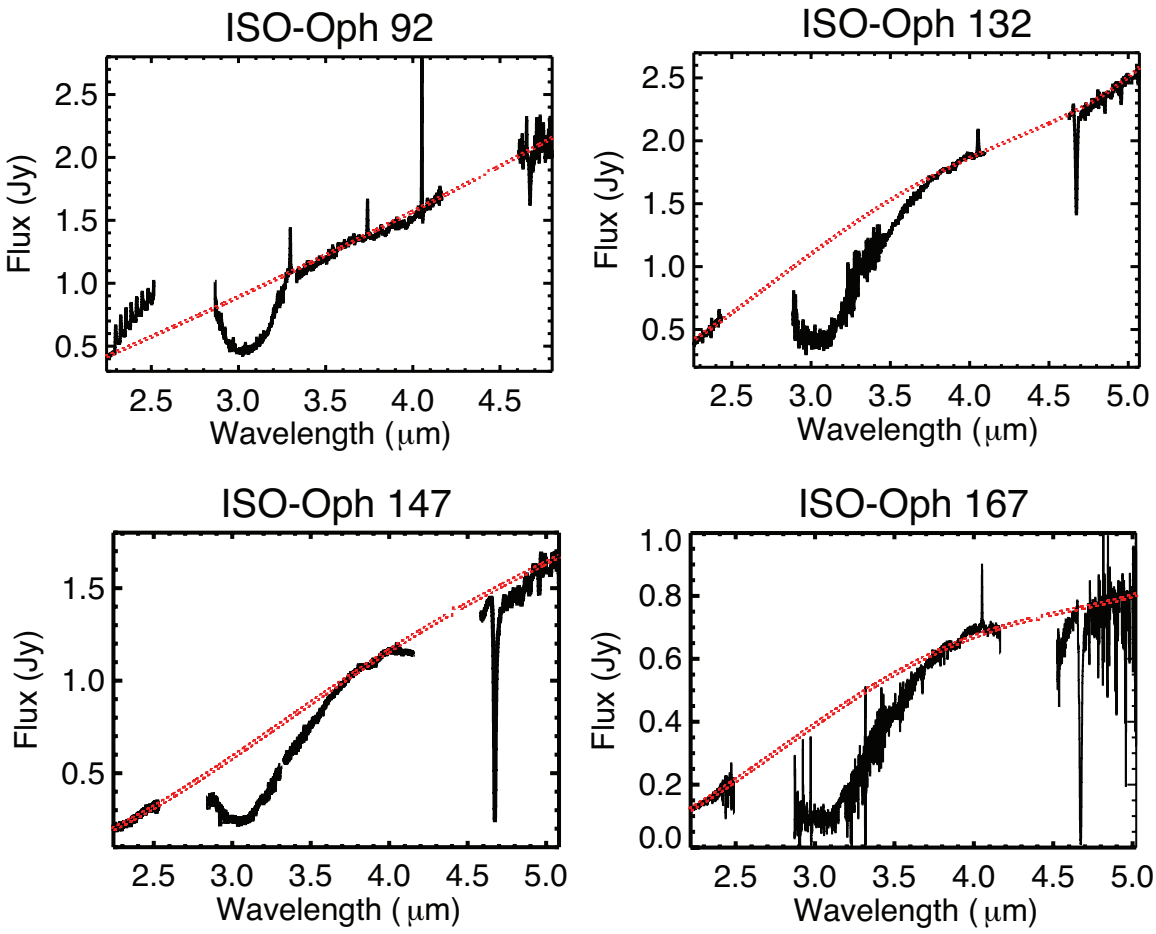

Figure 2.12 This figure illustrates the continuum determination for the 3 μm stretching mode of H_2O. The spectrum of each source is shown in black. The final polynomial fit to the continuum is shown as the red dotted line.

2.3. NIRSPEC ON THE KECK II AT THE WM KECK OBSERVATORY

2.3.1. Overview. Keck II is one of a pair of 10 m optical and infrared telescopes located at the WM Keck Observatory on Mauna Kea, HI (McLean et al., 1998). They are the largest optical telescopes in the world, and their mirrors are composed of 36 hexagonal segments that are controlled to work as a single mirror (Figure 2.13). The telescopes have an active optics system which allows the mirrors to deform in response to turbulence in Earth's atmosphere, and a number of spectrographs and cameras including the Deep Extragalactic Imaging Multi-Object Spectrograph (DEIMOS), the Echellette Spectrograph (ESI),

the High Resolution Echelle Spectrometer (HIRES), the Low Resolution Imaging Spectrograph (LRIS), the Near Infrared Camera (NIRC), the second-generation Near Infrared Camera/AO system (NIRC-2/AO), the Near-Infared Spectrometer (NIRSPEC), and the OH-Suppressing Infrared Imaging Spectrograph (OSIRIS). We used the 0.43″ x 24″ slit on NIRSPEC, a cross-dispersed high resolution cryogenic echelle spectrograph. This results in a resolving power of ∼25,000 and, using several different filters, covers the 0.95-5.4 μm wavelength range.

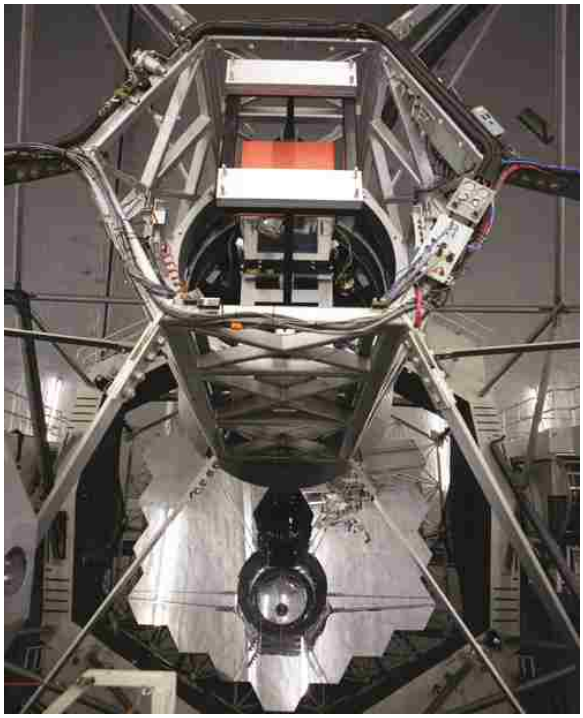

Figure 2.13 This image shows the segmented primary mirror of the Keck II telescope, along with the secondary mirror and instrument assembly. ©LaurieHatch.com

2.3.2. Keck II Observations & Data Reduction. High-dispersion, infrared observations of GV Tau were taken with NIRSPEC in 2003 and 2006. The high resolving power of NIRSPEC allows for the clean separation of fundamental and excited states of ^{12}CO, ^{13}CO, and $C^{18}O$ as well as the ν_1 band of HCN and two strong bands of C_2H_2 (ν_3 and $\nu_2 + (\nu_4 + \nu_5)^0_+$). Table 2.4 presents the spectral settings, wavelength coverage, and integration times for the spectral orders analyzed in this project. The M- and K-band data covering the fundamental and overtone transitions of CO, respectively, were acquired in March and August 2003. KL band spectra were obtained on February 17-18, 2006 to search for gas phase absorptions due to organic species toward GV Tau. The infrared companion of GV Tau, GV Tau N, was observed simultaneously with GV Tau S during the February 17, 2006 and March 2003 observations, enabling us to characterize the spectra toward both objects.

Like SpeX, NIRSPEC is a cross-dispersed instrument, which allows a large spectral range to be observed by splitting it into several rows on the detector. However, this also means the the data must be processed according to orders, or the different rows on the detector. The observations were taken using the ABBA method to provide a first order correction from atmospheric contributions. We began by stacking the data, clipping the appropriate order from the file, and then flat fielding and performing dark subtraction. The data do not fall linearly across the detector, so it is necessary to straighten the clipped data in both the spatial and spectral directions. Spatial straightening involves fitting a gaussian to each column to determine the peak position of the star, then fitting a polynomial to the peak positions, and finally using that polynomial to place the data horizontally. Spectral straightening was achieved using sky emission lines at known wavelengths. Once straightening was complete, data were cleaned by comparing each pixel to its neighbors using the standard deviation. We performed a careful inspection with various multiples of standard deviation to check that bad pixels were removed but data were not. This corrects for systematically hot and dead pixels and cosmic ray hits. Examples of extracted spectra are shown in Figures 2.14 and 2.15.

Table 2.4. Observing log.

Date	Instrument Setting	Wavelength Coverage	Integration Time (s)
03/18/2003	MW1	2118–2153 cm^{-1} (order 16)	240
03/18/2003	MW2	2094–2127 cm^{-1} (order 16)	240
08/05/2003	K1[a]	4202–4267 cm^{-1} (order 32)	1200
		4333–4397 cm^{-1} (order 33)	
08/05/2003	K2[a]	4265–4326 cm^{-1} (order 33)	1200
02/17/2006	KL1	3024–3072 cm^{-1} (order 23)	240
		3286–3337 cm^{-1} (order 25)	
02/18/2006	KL2[b]	2985–3028 cm^{-1} (order 23)	240
		3243–3290 cm^{-1} (order 25)	

[a]Note: The IRC was not in the slit in this observation.

[b]Note: The primary was not in the slit in this observation.

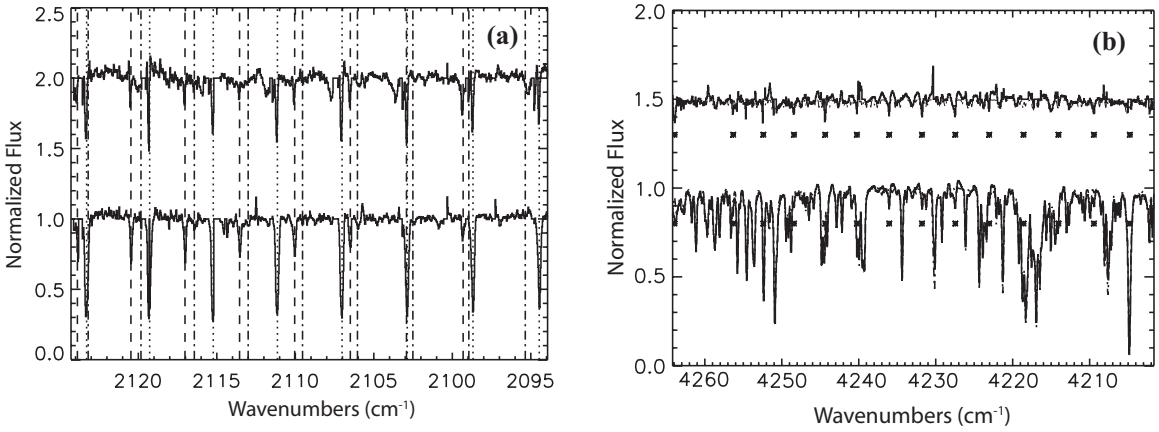

Figure 2.14 M-band and K band for GV Tau S are shown. (a) Sample normalized residual M-band spectrum showing CO absorption toward GV Tau S (bottom) and the IRC (top). The dotted lines indicate positions of the ^{12}CO lines, the dashed lines indicate ^{13}CO, and the dot-dashed lines indicate $C^{18}O$. (b) Normalized K-band spectrum of GV Tau S with the telluric model overplotted (dot-dash line). Above is the residual with the Arcturus spectrum overplotted, convolved to the resolving power of NIRSPEC, veiled and Doppler shifted to the geocentric velocity of GV Tau. Asterisks indicate the positions of CO v = (2-0) absorption lines.

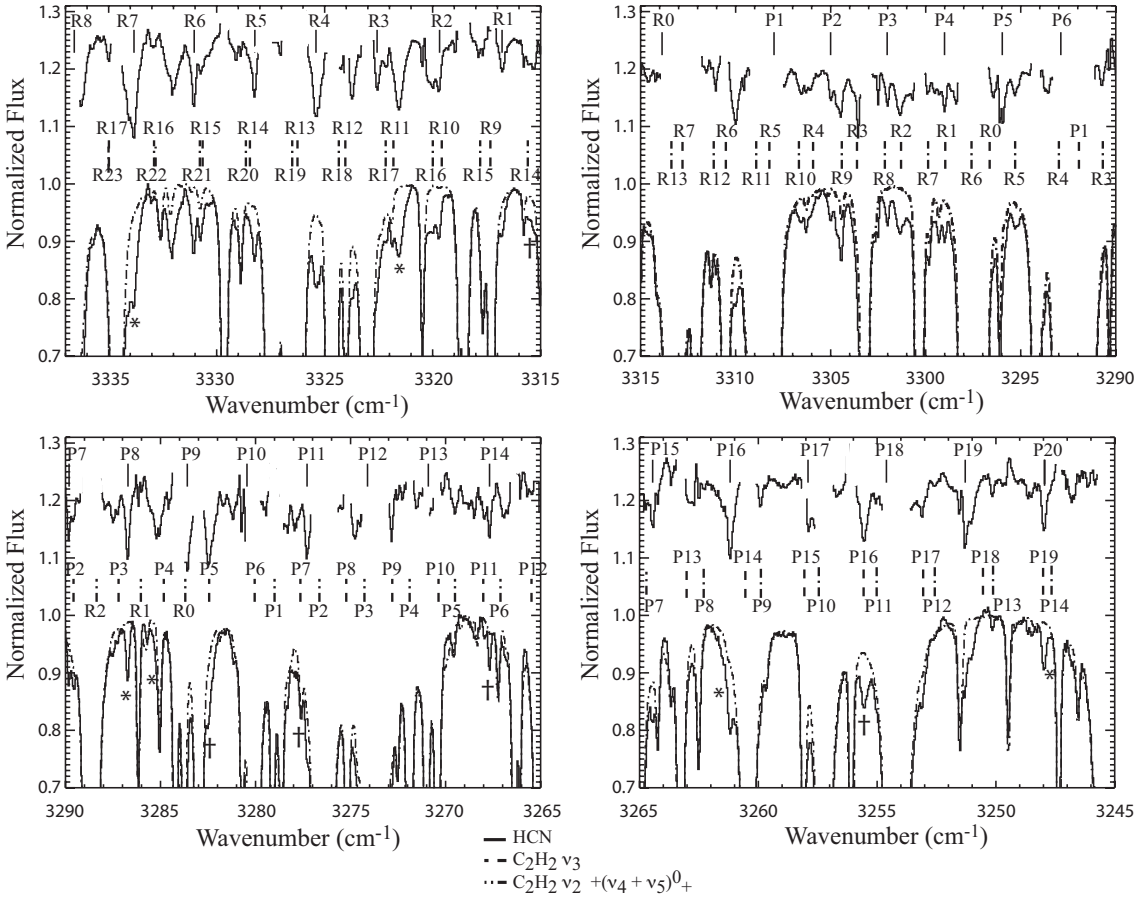

Figure 2.15 GV Tau N, KL Order 25 spectra showing the positions of HCN and C_2H_2 lines. The extracted spectra (solid black lines) are shown with the telluric spectra (dot-dashed) lines overplotted in the lower half of each frame. The residual spectra (data-telluric model) are shown shifted to the top of each frame, with tick marks above and below representing the positions of absorbing molecules. Solid black ticks are the HCN ν_1 band, dashed ticks indicate the C_2H_2 ν_3 band, and dot-dashed ticks indicate the C_2H_2 $\nu_2 + (\nu_4 + \nu_5)^0_+$ band. Asterisks and crosses denote Doppler shifted positions of stellar OH and NH, respectively. The gaps in the residual are regions where there is low transmittance of light due to our atmosphere.

The ABBA method only provides a first order correction for the atmosphere. In order to remove atmospheric absorptions, an atmospheric transmittance function was modeled using the Spectrum Synthesis Program (Kunde & Maguire, 1974, SSP), which accesses the HITRAN 2004 molecular database (Rothman et al., 2005). For each grating setting, the column burdens of atmospheric species, the spectral resolving power, and the wavelength calibrations were established by fitting the optimized model. To extract our spectral absorption features, we subtracted the model, convolved to the resolution of the instrument, from the spectral extract. This results in a residual that is still convolved with the transmittance. For intrinsically narrow lines, we obtain the true line intensity incident at the top of the terrestrial atmosphere by dividing each spectral line by the transmittance at the Doppler shifted position using the fully resolved model. The optimized model is shown as the dashed line in Figures 2.14 and 2.15 and has been found to reproduce the telluric spectrum accurately.

3. ICE RESULTS

3.1. THE DARK CLOUDS OF RHO OPHIUCHI

Rho Ophiuchi is a nearby star forming region, ∼135 pc away (see Wilking et al. (2008) for discussion). It consists of three main dark clouds, L1688, L1689, and L1709. It has areas of extremely high extinction, at least A_v ∼50-100 in its densest cores. It is a region of low-mass and intermediate-mass clustered star formation. Most of our sources are located in the main cloud, L1688. Figure 3.1 illustrates the location of the three main cores. It is an 850 μm continuum map taken with the Submillimetre Common-Users Bolometer Array (SCUBA) at the James Clerk Maxwell Telescope (JCMT). Dark regions indicate areas of cold dense dust. In L1688, there are three main cores, A, B, and F. The A core is warmer than the B and F cores due to the presence of the intermediate mass YSO, Oph S1 (ISO-Oph 48), which has a spectral type of B4 (Gagné et al., 2004), and is located at a right ascension (RA) of $16^h26^m34.2^s$ and a declination (DEC) of -24°23'28.3". Oph S1 and another B star, SR 3 located at an RA of $16^h26^m09.3^s$ and a DEC of -24°34'12.1", are thought to be the major contributors to heating the dust in the cloud (Wilking et al., 2008). These nearby intermediate mass stars lead to strong external UV radiation. Also near the western edge of L1688 is another intermediate mass star, HD 147889, a B2V type star (Abergel, 1996), located at an RA of $16^h25^m24.3^s$ and a DEC of -24°27'56.3". HD 147889 is responsible for a photo dissociation region (PDR) at the western edge of the cloud.

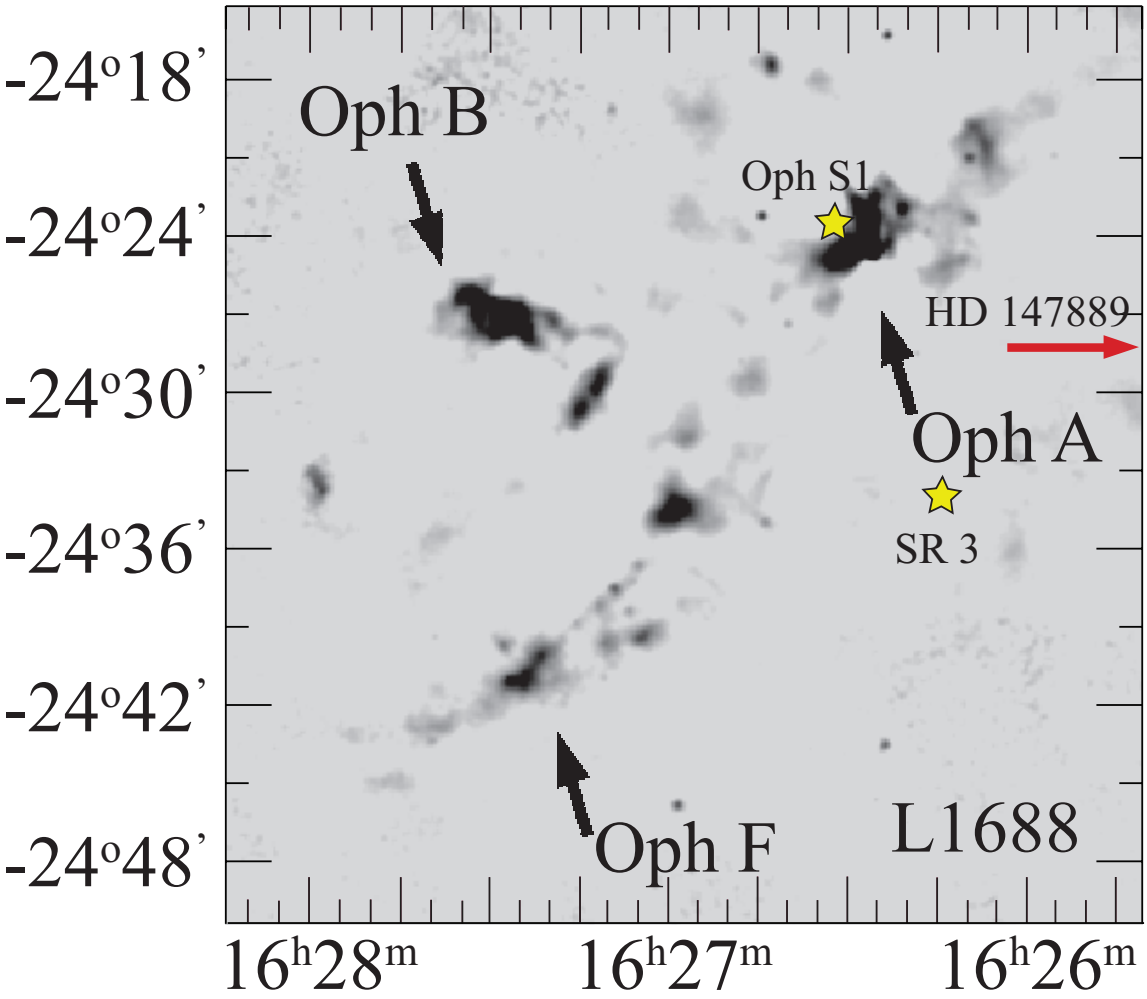

Figure 3.1 An 850 μm continuum map of L1688 in the Rho Ophiuchi region taken with the Submillimetre Common-User Bolometer Array (SCUBA) at the James Clerk Maxwell Telescope (JCMT) (Johnstone et al., 2000). The dark regions are areas of cold, dense dust. The Ophiuchus-A core is located in the upper right, the Ophiuchus-B core is in the middle-left, and the Ophiuchus-F core is in the lower left corner.

3.2. H_2O ICE

3.2.1. Background. H_2O was first detected in the gas phase in the ISM by Cheung et al. (1969) at microwave wavelengths. As was stated in §1, it was found as a solid by Gillett and Forrest (1973) toward the Becklin-Neugebauer object. H_2O ice is formed on the grain by successive hydrogenation reactions with oxygen (Tielens and Hagen, 1982), which has a high sticking probability

(Boogert and Ehrenfreund, 2004). However, it is uncertain if it follows a pathway of hydrogenation with atomic oxygen, O (Dulieu et al. (2010) and Romanzin et al. (2011)), molecular oxygen, O_2 (Ioppolo et al. (2008), Matar et al. (2008), Miyauchi et al. (2008), Oba et al. (2009), Cuppen et al. (2010), and Ioppolo et al. (2010)), ozone, O_3 (Tielens and Hagen (1982), Mokrane et al. (2009), Romanzin et al. (2011)), or a combination of all three. It is apparent, however, that reactions on the grain surface are essential for the formation of H_2O ice. It is not possible to account for the amount of H_2O ice found in the ISM using gas phase reactions alone (see D'Hendecourt et al. (1985) and Hasegawa et al. (1992)).

The three major vibrational modes of H_2O are the stretching mode at 3.05 μm, the bending mode at 6.0 μm, and the libration mode at 13 μm. The stretching mode is the only mode observable from the ground, and it is the most reliable mode. It has a band strength $\sim$16 times greater than the 6 μm bending mode and $\sim$3 times greater than the 13 μm libration mode. Although there are other absorbing features in the 3 μm region, it is the major contributing species in the 3 μm region, unlike the 6 μm band for which there is evidence that the profile may also contain significant contributions from organic refractory materials (Gibb and Whittet, 2002), HCOOH at 5.85 μm and H_2CO at 5.7 μm. The profile shape of each H_2O mode is dependent on the composition and temperature of the ice (Figure 3.2). The profile of the 3 μm feature may also be affected by scattering since the grain size is similar to the wavelength of light. Therefore, it may be necessary to apply a scattering model based on the grain size and shape (see Chiar et al. (2002) and references therein). When possible, obtaining H_2O ice temperatures and column densities with the 3 μm mode is desirable. Unfortunately, this mode was not in the spectral range of IRS on Spitzer. The next strongest mode, the libration mode at 13 μm, would seem to be the next best mode to use to characterize H_2O ice. However, the continuum determination is non-trivial, and affects the libration mode more than the bending mode, as was discussed in § 2.1.4. Therefore, we focused on the 6 μm bending mode to determine H_2O ice column densities, unless 3 μm data were available.

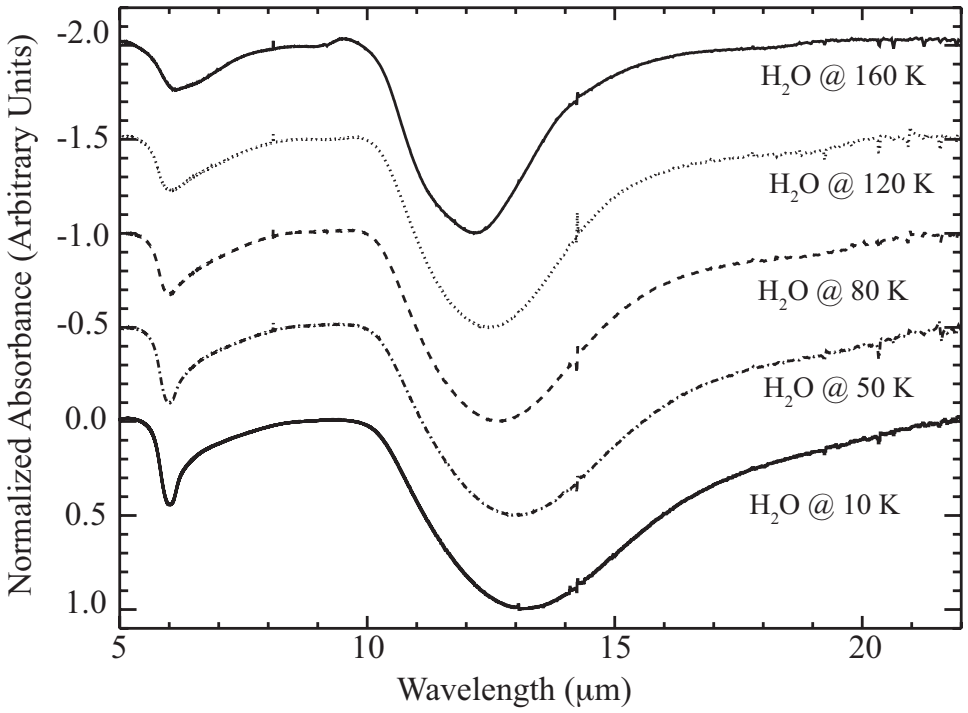

Figure 3.2 Laboratory spectra showing the dependence of the H_2O bending and libration profiles on temperature (Ehrenfreud et al., 1999). The normalized spectra of H_2O at 10 K, 50 K, 80 K, 120 K, and 160 K are plotted, offset for clarity. Note that at 6 μm as the temperature increases the profile widens, adding a shoulder at longer wavelengths, but the peak position is constant. However, for the 13 μm libration mode the peak position shifts to shorter wavelengths and becomes narrower as the temperature increases.

3.2.2. Laboratory Fits. Once the optical depths were calculated, a least χ^2 fit was performed with laboratory data. The 6 μm H_2O profile was fit with components from two groups: pure H_2O ranging from 10 K - 160 K for one group, and either pure H_2CO at 10 K or pure HCOOH at 10 K - 80 K for the other group. The 3 μm data was also fit using two components, but a two-temperature fit was completed and minor species were not included. Each group of components contained only pure H_2O ranging from 10 K - 160 K. This mode required an additional step, the application of a scattering model (see Chiar et al. (2002) and references therein for details). As the size of the ice-covered grains approaches the wavelength of the radiation, scattering is not negligible, and it changes the ice profile. The scattering model uses Mie scattering of spherical

silicate grains with a graphite coating which follow an MRN size distribution, $N(a) \sim a^{-3.5}$ (Mathis et al., 1977). The minimum grain size is 0.005 μm and the maximum grain size ranges from 0.02 μm to 0.65 μm. While the scattering model was necessary for H_2O at 3 μm, it is not necessary at 6 μm and 13 μm for our maximum grain size.

The pure H_2O laboratory spectra were taken from Hudgins et al. (2003). The methods used to measure pure H_2CO and pure HCOOH in the laboratory are described in Gerakines et al. (1996)[1]. The peak optical depth of each component was determined using the laboratory spectra and the peak optical depth of the absorption feature was measured from the data. These values are presented in Table 3.1. The best laboratory mixtures for each component are listed in Table 3.2. Finally, the total column density and the column density of each component were determined from the laboratory spectra and are listed in Table 3.3.

[1] *http://www.strw.leidenuniv.nl/lab/databases/ice-analogues-schutte/database/*

Table 3.1. Peak optical depths for 6 μm feature.

Source	H_2O	H_2CO	HCOOH	Total
ISO-Oph 29	0.113	—	—	0.117±0.002
ISO-Oph 65	0.104	0.032	—	0.108±0.002
ISO-Oph 76	0.191	—	0.096	0.255±0.032
ISO-Oph 77	0.326	0.166	—	0.327±0.044
ISO-Oph 92[a]	0.651	—	—	0.754±0.020
ISO-Oph 99	0.151	0.040	—	0.153±0.032
ISO-Oph 112	0.071	—	0.032	0.164±0.007
ISO-Oph 114	0.107	—	—	0.153±0.001
ISO-Oph 119	0.227	—	0.149	0.325±0.006
ISO-Oph 120	0.179	—	0.043	0.186±0.014
WL 20S[b]	0.127	—	—	—
ISO-Oph 124	0.147	—	0.038	0.181±0.006
ISO-Oph 125	0.298	—	0.100	0.356±0.042
ISO-Oph 132[a]	1.052	—	—	0.244±0.008
ISO-Oph 134	0.183	—	0.034	0.212±0.004
ISO-Oph 137	0.239	—	0.032	0.526±0.013
ISO-Oph 139	0.101	—	0.040	0.139±0.009
ISO-Oph 141	0.275	—	—	0.272±0.010
ISO-Oph 143	0.184	—	—	0.282±0.004
ISO-Oph 144	0.140	—	0.048	0.163±0.009
ISO-Oph 145	0.082	0.016	—	0.082±0.001
ISO-Oph 147[a]	0.904	—	—	1.013±0.031
ISO-Oph 154	0.068	—	0.035	0.096±0.005
ISO-Oph 161	0.120	—	0.154	0.245±0.013
ISO-Oph 167[a]	1.808	—	0.047	1.605±0.485
WLY 2-63	0.132	—	—	0.154±0.002
ISO-Oph 204	0.079	—	—	0.080±0.012
ISO-Oph 209	0.430	—	0.219	0.563±0.002

[a]The stretching mode at 3 μm was measured.

[b]The data at 6 μm do not show a definite peak to use for the determination of the peak optical depth (see Figure 4.2).

Table 3.2. Best laboratory spectra for 6 μm feature.

Source	H_2O	H_2CO	HCOOH
ISO-Oph 29	Pure H_2O 50 K	—	—
ISO-Oph 65	Pure H_2O 10 K	Pure H_2CO 10 K	—
ISO-Oph 76	Pure H_2O 160 K	—	Pure HCOOH 80 K
ISO-Oph 77	Pure H_2O 10 K	Pure H_2CO 10 K	—
ISO-Oph 92	Pure H_2O 10 K; 0.25 μm	—	—
ISO-Oph 99	Pure H_2O 10 K	Pure H_2CO 10 K	—
ISO-Oph 112	Pure H_2O 80 K	—	Pure HCOOH 80K
ISO-Oph 114	Pure H_2O 10 K	—	—
ISO-Oph 119	Pure H_2O 10 K	—	Pure HCOOH 10 K
ISO-Oph 120	Pure H_2O 10 K	—	Pure HCOOH 10 K
WL 20S	Pure H_2O 80 K	—	—
ISO-Oph 124	Pure H_2O 80 K	—	Pure HCOOH 10 K
ISO-Oph 125	Pure H_2O 80 K	—	Pure HCOOH 50 K
ISO-Oph 132	Pure H_2O 10K; 0.65 μm	—	—
ISO-Oph 134	Pure H_2O 10 K	—	Pure HCOOH 10 K
ISO-Oph 137	Pure H_2O 10 K	—	Pure HCOOH 10 K
ISO-Oph 139	Pure H_2O 120 K	Pure H_2CO 10 K	—
ISO-Oph 141	Pure H_2O 10 K	—	Pure HCOOH 10K
ISO-Oph 143	Pure H_2O 10 K	Pure H_2CO 10 K	—
ISO-Oph 144	Pure H_2O 10 K	Pure H_2CO 10 K	—
ISO-Oph 145	Pure H_2O 10 K	Pure H_2CO 10 K	—
ISO-Oph 147	Pure H_2O 10K; 0.65 μm	—	—
ISO-Oph 154	Pure H_2O 80 K	—	Pure HCOOH 50 K
ISO-Oph 161	Pure H_2O 30 K	—	Pure HCOOH 10 K
ISO-Oph 167	Pure H_2O 10K; 0.65 μm	—	—
WLY 2-63	Pure H_2O 10 K	—	—
ISO-Oph 204	Pure H_2O 80 K	—	—
ISO-Oph 209	Pure H_2O 10 K	—	Pure HCOOH 10 K

Table 3.3. Column densities, N for species near 6 μm.

Source	H_2O (10^{17} molecules/cm^2)	H_2CO	HCOOH
ISO-Oph 29	22.9±0.6	—	—
ISO-0ph 65	18.5±1.4	0.6	—
ISO-Oph 76	34.2±6.2	—	1.2
ISO-Oph 77	58.4±23.4	2.6	—
ISO-Oph 92[a]	11.4±0.4	—	—
ISO-Oph 99	27.0±8.2	0.6	—
ISO-Oph 112	16.9±2.3	—	0.4
ISO-Oph 114	28.7±0.2	—	—
ISO-Oph 119	40.6±3.3	—	1.7
ISO-Oph 120	28.5±4.1	—	0.6
WL 20S	22.8±3.1	—	—
ISO-Oph 124	35.1±1.9	—	0.6
ISO-Oph 125	78.2±10.9	—	1.2
ISO-Oph 132[a]	22.1±0.3	—	—
ISO-Oph 134	32.7±2.0	—	0.435
ISO-Oph 137	42.70±1.3	—	0.358
ISO-Oph 139	25.9±5.3	0.6	—
ISO-Oph 141	49.1±3.2	—	—
ISO-Oph 143	37.5±2.3	—	—
ISO-Oph 144	25.1±2.4	—	0.6
ISO-Oph 145	14.2±0.4	—	—
ISO-Oph 147[a]	19.8±0.5	—	—
ISO-Oph 154	16.1±2.9	—	0.4
ISO-Oph 161	22.9±4.8	—	2.0
ISO-Oph 167[a]	35.9±1.1	—	0.5
WLY 2-63	23.6±0.9	—	—
ISO-Oph 204	14.2±2.5	—	—
ISO-Oph 209	76.9±2.2	—	2.5

[a]The stretching mode at 3 μm was measured.

3.3. CO_2 ICE

3.3.1. Background. Interstellar CO_2 ice was discovered by de Graauw et al. (1996) using the short wavelength spectrometer (SWS) on ISO. Like H_2O, it is found as a solid on dust grains, and does not sublimate off of the grain until about 90 K (Gerakines et al., 1999). Its strongest mode is the asymmetric stretching fundamental vibration at 4.27 μm. This mode, as well as two combination modes at 2.70 μm and 2.78 μm and the bending mode at 15.2 μm were studied with ISO (Keane et al., 2001). Like the bending mode, the combination modes can only be studied from space because of atmospheric absorption. As such, the only mode that can be studied in the infrared with current observatories is the bending mode at 15.2 μm (Gerakines et al., 1999).

The profile of CO_2 consists of three main components: a broad polar component (H_2O-rich), a non-polar (H_2O-poor) component, and a broad shoulder due to

combination with CH_3OH (Gerakines et al., 1999). It is environment-dependent, and thus is an important tracer of the evolution of the molecular cloud. Laboratory mixtures with varying compositions and temperatures taken from databases provided by Ehrenfreud et al. (1999) and White et al. (2009) can be used to show this dependence. Figure 3.3 shows how the profile changes in the presence of other molecules. These molecules interact with the CO_2, slightly changing its dipole moment, which affects the peak wavelength and width of the CO_2 ice profile. The temperature also affects the CO_2 profile. For example, pure CO_2 and annealed CO_2 mixtures result in a profile that is double–peaked (see Figures 3.4 and 3.5). Note that in each of these cases, the peak position and width of the profile change. In addition, Figure 3.5 shows the profile dependence in the presence of CH_3OH, as well as the profile of pure CO_2 at 10 K and 80 K.

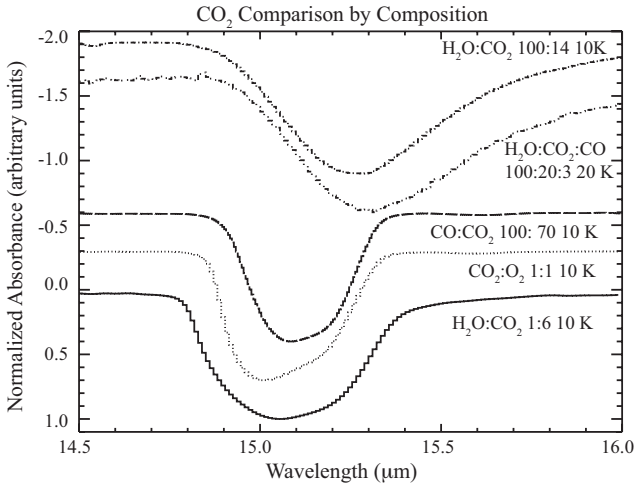

Figure 3.3 The profile of the CO_2 ice depends on other molecules present in the mixture. Here we present cold laboratory spectra (offset for clarity) of mixtures of CO_2 with other molecules (see Ehrenfreud et al. (1999) and White et al. (2009)). The three lowest profiles are apolar mixtures while the top two are polar mixtures, which have a high content of H_2O. Note that both the peak and width of the profiles change. For example, the profiles of the polar mixtures are shifted to longer wavelengths compared to the profiles of the apolar mixtures.

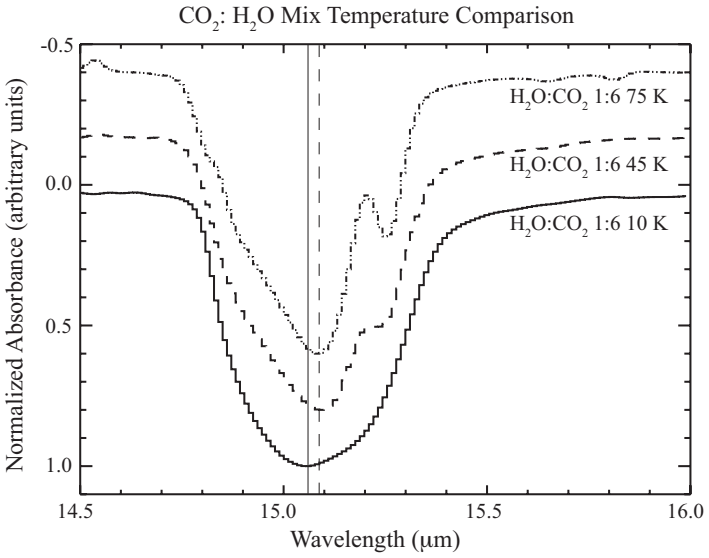

Figure 3.4 Laboratory spectra illustrating the dependence of the bending mode profile on temperature (Ehrenfreud et al., 1999). The normalized spectra of H_2O:CO_2 1:6 mixture at 10 K, 45 K, and 75 K are plotted, offset for clarity. Notice that the profile is broader at colder temperatures. As the ice is heated, or annealed, the profile splits into a double-peaked structure.

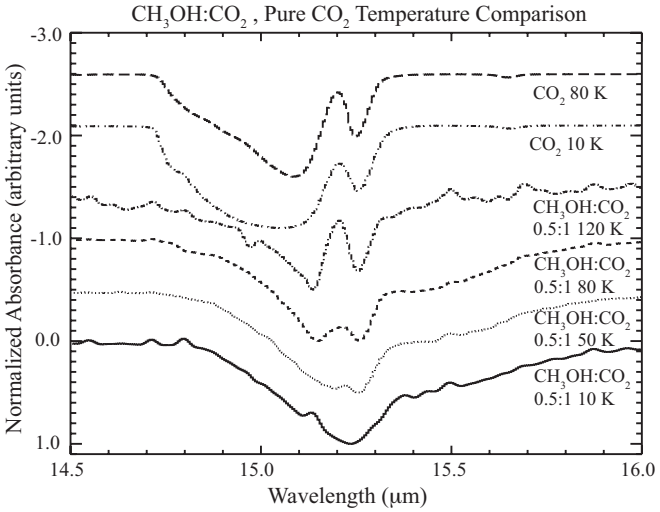

Figure 3.5 In many of our sources, it is necessary to include CH_3OH in the mixture with CO_2. The four bottom laboratory fits are a mixture of CH_3OH and CO_2 at increasing temperatures, 10 K, 50 K, 80 K, and 120 K (White et al., 2009). The most notable feature of a mixture including CH_3OH is the presence of a "shoulder" at red wavelengths. Again, note that as the mixture is annealed the profile has a double-peaked structure. The widths of each peak depends on both the temperature and composition. For comparison, the top two spectra are pure CO_2 at 10 K and 80 K (Ehrenfreud et al., 1999).

Early results, for example, Gerakines et al. (1999), reported an average CO_2 abundance of 17±3% with respect to H_2O regardless of whether it was observed toward a YSO, in the quiescent interstellar medium, or toward background stars. However, their data show some scatter, with individual abundances ranging from 9-23%. Whittet et al. (2009) report abundances ranging from 21-35% toward background stars in Taurus. They also note that a large percentage of the CO_2 ice feature consists of a polar component, ∼85%. Pontoppidan et al. (2008) report an average abundance of CO_2 28±2% toward low mass YSOs, and Nummelin et al. (2001) found a column density ratio toward two intermediate mass YSOs of 34-37%, and an abundance of 9-30% toward several other sources, including high and intermediate mass YSOs, field stars, and an FU Orionis-type object. More recent results indicate a lower abundance toward low mass YSOs in Taurus of 12%±4% (Zasowski et al., 2009). Cook et al. (2011) report a strong correlation between H_2O and CO_2 toward low mass YSOs in Taurus, with a steeper slope, 0.29±0.01, than that found for background objects, 0.18±0.04, for background objects in Taurus, which also show a strong correlation. They report a slope of 0.28±0.03 toward all low mass YSOs in their sample, again, with a strong correlation. In addition, in contrast to the CO_2 toward quiescent regions, Pontoppidan et al. (2008) found that the CO_2 toward some high mass YSOs show a double-peak feature, indicating a portion of the pure CO_2 is crystalline. We now know that this double-peak feature is not limited to high mass YSOs, but is also found toward low mass YSOs. The mechanism for the double-peak feature is still unknown, but could be due to CO_2 splitting from a polar mixture of CH_3OH and H_2O upon heating (segregation) or CO sublimating from an apolar CO and CO_2 mixture, leaving behind pure CO_2 (distillation) (Pontoppidan et al., 2008).

3.3.2. Potential Formation Routes. The CO_2 found in the ice mantles on grains is thought to form on the grain, rather than being adsorbed from the gas phase. There are three potential pathways to formation on grains (Pontoppidan et al., 2008):

$$CO + OH \rightarrow CO_2 + H \quad (3)$$

$$O + HCO \rightarrow CO_2 + H \quad (4)$$

$$CO + O \rightarrow CO_2 \quad (5)$$

The exact mechanism is still unknown, but is likely a combination of each of the reactions depending on environment. Reaction (3) has a small activation barrier of 80 K according to Ruffle and Herbst (2001), but Oba et al. (2010) found this reaction can occur at temperatures as low as 10 K using surface experiments. Although reaction (4) is barrierless (Garrod and Pauly, 2011), Woon (2002) found that the HCO radical needed for the reaction possesses an activation-energy barrier of 500 K. Reaction (5) is much more controversial. Before the discovery of CO_2 in the interstellar medium, simulations predicted CO_2 should be easily formed and abundant for this direct formation route (Tielens and Hagen, 1982). These simulations agreed with laboratory experiments performed by Fournier et al. (1979). If this is the case, then CO_2 should be found toward many diverse lines of sight. The restricting factors would be the availability of CO and O, and temperatures low enough (<90 K) that the CO_2 ice does not sublimate off the grain. (Roser et al., 2001) and (D'Hendecourt et al., 1985) reported that it possesses a significant activation barrier of 290 K - 1000 K, but Grim and d'Hendecourt (1986) suggested the barrier may be overcome via UV photolysis. However, Roser et al. (2001) report CO_2 can be efficiently formed via equation (5), without UV photolysis. There are two main differences in these experiments. In the Grim and d'Hendecourt (1986) experiment, the O atoms were obtained from photolysis of O_2, whereas Roser et al. (2001) used solid CO and O. In addition, Roser et al. (2001) deposited a layer of H_2O-ice on top of the CO and O, simulating the formation of CO_2 in a polar environment. This result was confirmed by Menella et al. (2004). It suggests that CO_2 may be efficiently formed in a polar environment (Oba et al., 2010), however, it does not correctly simulate astrophysical conditions since the polar ice is deposited on top of an apolar layer, rather than being deposited on the grain first.

3.3.3. Laboratory Fits. Once the optical depths were calculated, a least χ^2 fit was performed with laboratory data. The CO_2 was fit with two or three components, either polar (H_2O-rich) and apolar (H_2O-poor) components, or polar, apolar, and annealed or methanol-rich CO_2-rich components. The polar and

apolar components were taken from Ehrenfreud et al. (1999), and the continuous distribution of ellipsoids was used. The annealed and methanol-rich laboratory mixtures were provided by White et al. (2009). The peak optical depth of each component was determined using the laboratory spectra and the peak optical depth of the absorption feature was measured from the data. These values are presented in Table 3.4. The best laboratory mixtures for each component are listed in Table 3.5. Finally, the column density of each component was determined from the laboratory spectra and are listed in Table 3.6. Only the total column density is given for sources for which only low-resolution data were available, as it is not possible to uniquely determine the composition.

Table 3.4. CO_2 peak optical depths.

Source	Polar	Apolar	Crystalline	Total
ISO-Oph 29	0.036	0.120	0.065	0.187±0.012
ISO-0ph 65	0.083	0.082	0.051	0.195±0.004
ISO-Oph 76	—	—	—	0.212±0.006
ISO-Oph 77	—	—	—	0.220±0.036
ISO-Oph 90	0.951	0.611	—	1.450±0.017
ISO-Oph 92	0.120	—	0.064	0.195±0.003
ISO-Oph 99	—	—	—	0.366±0.008
ISO-Oph 108	0.114	0.050	0.141	0.274±0.018
ISO-Oph 112	0.104	0.012	—	0.119±0.009
ISO-Oph 114	0.099	0.043	0.075	0.212±0.012
ISO-Oph 119	—	—	—	0.065±0.018
ISO-Oph 120	—	—	—	0.348±0.006
WL 20S	0.083	—	0.182	0.282±0.015
WL 20W	0.084	—	0.057	0.152±0.008
ISO-Oph 124	0.104	—	0.094	0.215±0.032
ISO-Oph 125	0.250	0.082	—	0.307±0.005
ISO-Oph 132	0.177	0.062	—	0.244±0.008
ISO-Oph 134	0.203	0.109	0.152	0.452±0.003
ISO-Oph 137	0.333	0.216	—	0.521±0.013
ISO-Oph 139	—	—	—	0.088±0.009
ISO-Oph 141	0.120	0.084	0.438	0.606±0.014
ISO-Oph 143	0.109	—	0.211	0.322±0.011
ISO-Oph 144	0.156	0.082	—	0.265±0.021
ISO-Oph 145	0.078	0.013	—	0.078±0.006
ISO-Oph 147	0.104	0.119	0.084	0.286±0.006
ISO-Oph 154	0.088	—	—	0.088±0.006
ISO-Oph 161	—	—	—	0.495±0.044
ISO-Oph 167	0.114	0.236	0.213	0.546±0.005
WLY 2-63	0.177	0.153	0.052	0.358±0.033
ISO-Oph 204	0.094	0.036	0.040	0.171±0.009
ISO-Oph 209	0.088	0.324	0.505	0.928±0.058

Table 3.5. Best CO_2 laboratory spectra.

Source	CO_2 Polar	CO_2 Apolar	CO_2 Crystalline
ISO-Oph 29	H_2O:CO_2:CO	H_2O:CO_2	H_2O:CO_2
	100:20:3 20 K	1:6 50 K	15:1 130 K
ISO-0ph 65	H_2O:CO_2	H_2O:CO:CO_2	H_2O:CH_3OH:CO_2
	100:14 10 K	1:50:56 10 K	10:17:1 120 K
ISO-Oph 90	H_2O:CO_2	CO:N_2:CO_2	—
	100:14 10 K	100:50:20 30 K	
ISO-Oph 92	H_2O:CO_2	—	H_2O:CO_2
	100:14 10 K		1.9:1 90 K
ISO-Oph 108	H_2O:CO_2	CO:O_2:CO_2	H_2O:CH_3OH:CO_2
	100:14 10 K	100:50:21 30 K	1.8:0.5:1 120 K
ISO-Oph 112	H_2O:CO_2	CO:N_2:CO_2	—
	100:14 10 K	100:50:20 30 K	
ISO-Oph 114	H_2O:CO_2:CO	CO:CO_2	H_2O:CH_3OH:CO_2
	100:20:3 20 K	100:26 10K	2.2: 1.5:1 135 K
WL 20W	H_2O:CO_2:CO	—	H_2O:CH_3OH:CO_2
	100:20:3 20 K		2:0.9:1 140 K
WL 20S	H_2O:CO_2	—	H_2O:CH_3OH:CO_2
	100:14 10 K		1.8:0.5:1 120 K
ISO-Oph 124	H_2O:CO_2	—	CH_3OH:CO_2
	100:14 10 K		0.5:1 80 K
ISO-Oph 125	H_2O:CO_2	H_2O:CO:CO_2	—
	100:14 10 K	1:50:56 10 K	
ISO-Oph 132	H_2O:CO_2	H_2O:CO_2	—
	100:14 10 K	100:70 10 K	
ISO-Oph 134	H_2O:CO_2	CO:O_2:CO_2	H_2O:CH_3OH:CO_2
	100:14 10 K	100:50:32 10 K	2:0.9:1 120 K
ISO-Oph 137	H_2O:CO_2	CO:O_2:CO_2	—
	100:14 10 K	100:11:20 10 K	
ISO-Oph 141	H_2O:CO_2	CO:O_2:CO_2	H_2O:CH_3OH:CO_2
	100:14 10 K	100:50:21 30 K	2:0.9:1 120 K
ISO-Oph 143	H_2O:CO_2	—	H_2O:CH_3OH:CO_2
	100:14 10 K		2:0.9:1 120 K
ISO-Oph 144	H_2O:CO_2	H_2O:CO:CO_2	—
	100:14 10 K	1:50:56 10 K	
ISO-Oph 145	H_2O:CO_2:CO	CO:N_2:CO_2	—
	100:20:3 20 K	100:50:20 30 K	
ISO-Oph 147	H_2O:CO_2	CO:O_2:N_2:CO_2	H_2O:CH_3OH:CO_2
	100:14 10 K	100:50:25:32 30 K	2:1:0.1 120 K
ISO-Oph 154	H_2O:CO_2	—	—
	100:14 10 K		
ISO-Oph 167	H_2O:CO_2	CO:O_2:CO_2	H_2O:CH_3OH:CO_2
	100:14 10 K	100:50:32 10 K	2.1:0.1:1 120 K
WLY 2-63	H_2O:CO_2	CO:O_2:N_2:CO_2	H_2O:CO_2
	100:14 10 K	100:50:25:32 30 K	1.9:1 150 K
ISO-Oph 204	H_2O:CO_2	CO:O2:CO_2	H_2O:CH_3OH:CO_2
	100:14 10 K	100:50:32 10 K	2:0.9:1 140 K
ISO-Oph 209	H_2O:CO_2	H_2O:CO_2	H_2O:CH_3OH:CO_2
	100:14 10 K	1:6 42 K	2:0.9:1 120 K

Table 3.6. CO_2 column densities, N.

Source	Polar	Apolar	Crystalline	Total
	(10^{17} molecules/cm^2)			
ISO-Oph 29	0.78	1.94	1.07	3.79±0.39
ISO-0ph 65	1.81	1.09	0.88	3.76±0.36
ISO-Oph 76	—	—	—	5.59±0.58
ISO-Oph 77	—	—	—	5.72±1.04
ISO-Oph 90	20.69	5.54	—	26.20±0.76
ISO-Oph 92	2.60	—	1.26	3.84±0.38
ISO-Oph 99	—	—	—	8.16±0.78
ISO-Oph 108	2.49	0.47	2.84	5.79±0.62
ISO-Oph 112	2.26	0.11	—	2.37±0.30
ISO-Oph 114	2.17	0.37	1.00	3.54±0.53
ISO-Oph 119	—	—	—	15.18±1.53
ISO-Oph 120	—	—	—	7.55±0.56
WL 20S	1.81	—	3.65	5.45±0.28
WL 20W	2.01	—	1.06	3.08±0.35
ISO-Oph 124	2.35	—	1.60	3.95±0.61
ISO-Oph 125	5.43	1.09	—	6.51±0.28
ISO-Oph 132	3.85	0.75	—	4.59±0.34
ISO-Oph 134	4.41	1.05	3.07	8.54±0.23
ISO-Oph 137	7.24	1.73	—	8.96±0.46
ISO-Oph 139	—	—	—	2.12±0.29
ISO-Oph 141	2.60	0.80	8.93	12.31±0.49
ISO-Oph 143	2.47	—	4.40	6.87±0.22
ISO-Oph 144	3.39	1.09	—	4.47±0.88
ISO-Oph 145	1.71	0.11	—	1.82±0.18
ISO-Oph 147	2.26	1.14	1.63	5.03±0.26
ISO-Oph 154	2.00	—	—	2.00±0.56
ISO-Oph 161	—	—	—	12.27±1.47
ISO-Oph 167	2.49	2.27	4.15	8.92±0.43
WLY 2-63	3.84	1.47	0.70	6.00±0.41
ISO-Oph 204	2.04	0.35	0.65	3.02±0.28
ISO-Oph 209	1.92	5.95	10.24	18.16±1.09

4. ICE ANALYSIS

CO_2 and H_2O are important diagnostics in interstellar ice studies. The profile shapes can be used to determine the thermal history of the ices and indicate which mixtures, such as polar, apolar, or crystalline, are present along the line of sight toward each object. This information, along with the density of the region, SED, and proximity to various objects, can be used to test formation scenarios suggested by different laboratory studies, such as those described in § 3. For example, if CO_2 forms in a hydrogen-rich environment in tandem with H_2O, as for reaction 3.3, we would expect the column density of CO_2 with respect to the column density of H_2O, $N(CO_2)/N(H_2O)$, to show a linear relation (Ioppolo et al., 2011). In this case, a large portion of the CO_2 would be polar, as is found toward unprocessed background stars. On the other hand, if CO_2 primarily forms in a hydrogen-poor environment on the apolar mantle, as for reactions 3.4 and 3.5, then we would not expect a linear correlation with water. In this case, there would be large differences between unprocessed background stars and warmer YSOs that heat and remove a significant portion of the apolar mantle. In this section, we investigate the correlations between CO_2 column densities and ice mixtures to H_2O column densities and ice mixtures, extinction, Spectral Energy Distribution (SED), and proximity to intermediate-mass young stars. In § 4.1 we make comparisons within a single star forming region, Rho Oph, and in § 4.2 compare Rho Oph as a whole with other star forming regions.

4.1. INTRACLOUD CORRELATIONS

4.1.1. Location. We can gain a better understanding of the local environment of our sources by considering data of the region at different wavelengths. For example, longer wavelengths are excellent tracers of cold, dense dust. Such data is available from the Submillimetre Common-User Bolometer Array (SCUBA) located on the James Clerk Maxwell Telescope (JCMT). In Figure 4.1, our source

positions located in L1688 are presented on an 850 μm continuum map created by Johnstone et al. (2000). Note the distribution of our sources. They are fairly well scattered throughout the cloud, with some located near the darkest areas, or the dense cores. Also note that there are several sources near the Oph B and Oph F cores, but only one near the Oph A core. Sources not located in L1688, ISO-Oph 204, ISO-Oph 209, and WLY 2-63 are not shown. We will be using this figure as a diagnostic throughout the analysis.

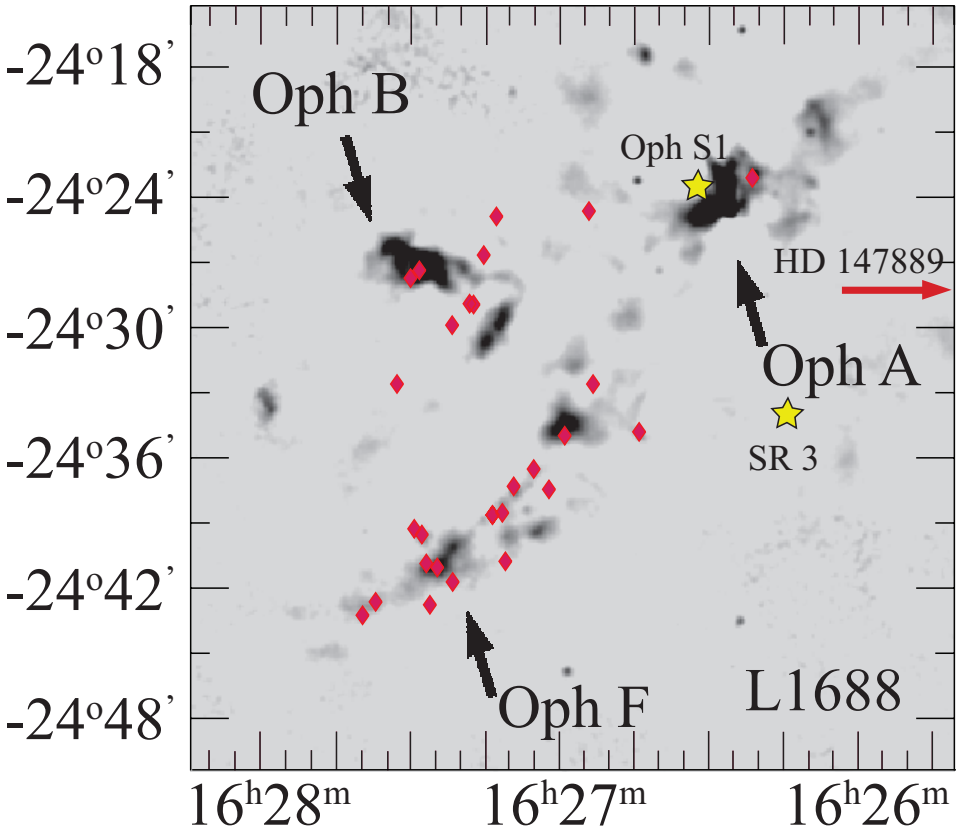

Figure 4.1 Our source positions are plotted on a map of L1688 in Rho Oph created at 850 μm with SCUBA on JCMT (Johnstone et al., 2000). The dark areas are cold, dense regions. The Oph A, B, and F cores are labeled. The positions of the three most massive members of L1688, Oph S1, SR 3, and HD 147889 are also indicated.

4.1.2. Laboratory Fits. 4.1.2.1. 6 μm ice feature. The optical depths and best laboratory mixtures for the ice at 6 μm are presented in Figure 4.2. Although the listed mixtures represent the least χ^2 available, in many cases there are several different mixtures that could produce a sufficient fit to the optical depth of our sources. The approach of using two components, the first being H_2O at different temperatures, and the second being H_2CO and HCOOH at different temperatures, has its benefits and disadvantages. By only including one component to determine the temperature of the H_2O, we can only determine if the H_2O is predominately cold or warm. However, including the H_2CO and HCOOH as the second component produced better fits at 6 μm. In addition, if there were multiple H_2O temperatures that gave similar fits at 6 μm, inclusion of the minor species produced a more consistent fit at 13 μm with a single temperature. Mixtures which provide similar χ^2 values do not affect the measured column density by more than a few percent, and we can obtain a range of temperatures and a general composition. For example, H_2O at 160 K and H_2O at 10 K will not give similar fits, in the absence PAH emission or absorption at 6.2 μm. In cases where PAH emission or absorption was present, the portion of the spectrum with the PAH was excluded from the laboratory fit. This increases the uncertainty in the peak position and the shape of the long wavelength wing of the feature, making the temperature determination uncertain, as is shown in Figure 4.3. About one-third of our sample shows potential PAH contamination, making the temperature determination uncertain. However, in general we categorize our sources as having either predominately cold ($\leq$50 K) or predominately warm (>50 K) H_2O, HCOOH, or H_2CO. The laboratory fits for H_2O show that 64% of the sources were best fit by mostly cold (10 K) H_2O. In order to reproduce the optical depth of the source at 6 μm, 25% required the addition of H_2CO and 44% required the addition of HCOOH. In general, sources with warm H_2O that required HCOOH contained warm HCOOH, and sources with cold H_2O that required HCOOH or H_2CO contained those species at a temperature similar to the H_2O. These similar temperatures indicate that these molecules may be located in the same location along the line of sight toward the YSO rather than being distributed at two different depths along the line of sight, for example in the

foreground molecular cloud material or in the circumstellar material associated with the YSO. Figure 4.4 shows the locations of sources with a predominately cold 6 μm component and a predominately warm 6 μm component. Note that the sources are scattered throughout the figure; there is no cluster of warm or cold sources. If the warm or cold sources had been near a dense core or nearby star, it might indicate an influence from the respective core or nearby star. There are sources with a warm ice feature located in less dense areas, away from the cold, dense cores, indicating that perhaps radial proximity to the core provides some protection from external radiation. However, in less dense regions there are YSOs with cold ices and YSOs with warm ices. Therefore, while sources located near dense cores may be protected from external radiation, resulting in a cold ice feature at 6 μm, radial proximity to a dense core is not required for a cold 6 μm ice feature. It is also important to note that we are only considering the radial distance to the dark cores, not the relative distance, since we are viewing a two-dimensional projection onto the sky and do not know the distance to each source, or its depth within the cloud.

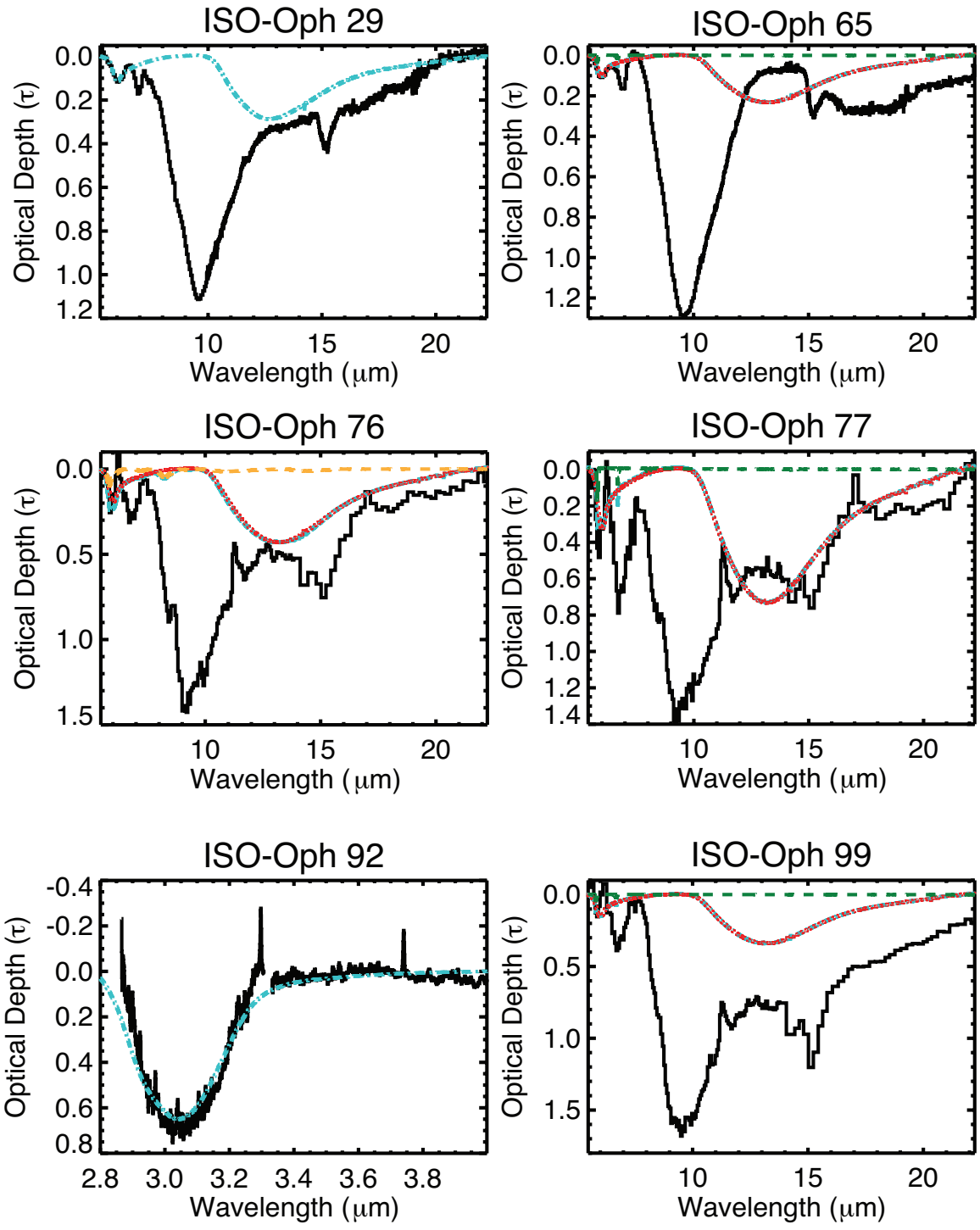

Figure 4.2 Optical depths with best fit laboratory spectra for H_2O. The data are the solid black line. The H_2O, H_2CO, and HCOOHlaboratory components are the red dotted line, the orange dashed line, and the green dashed line, respectively. The sum of each component is the total laboratory spectrum, and is shown as the teal dot-dashed line.

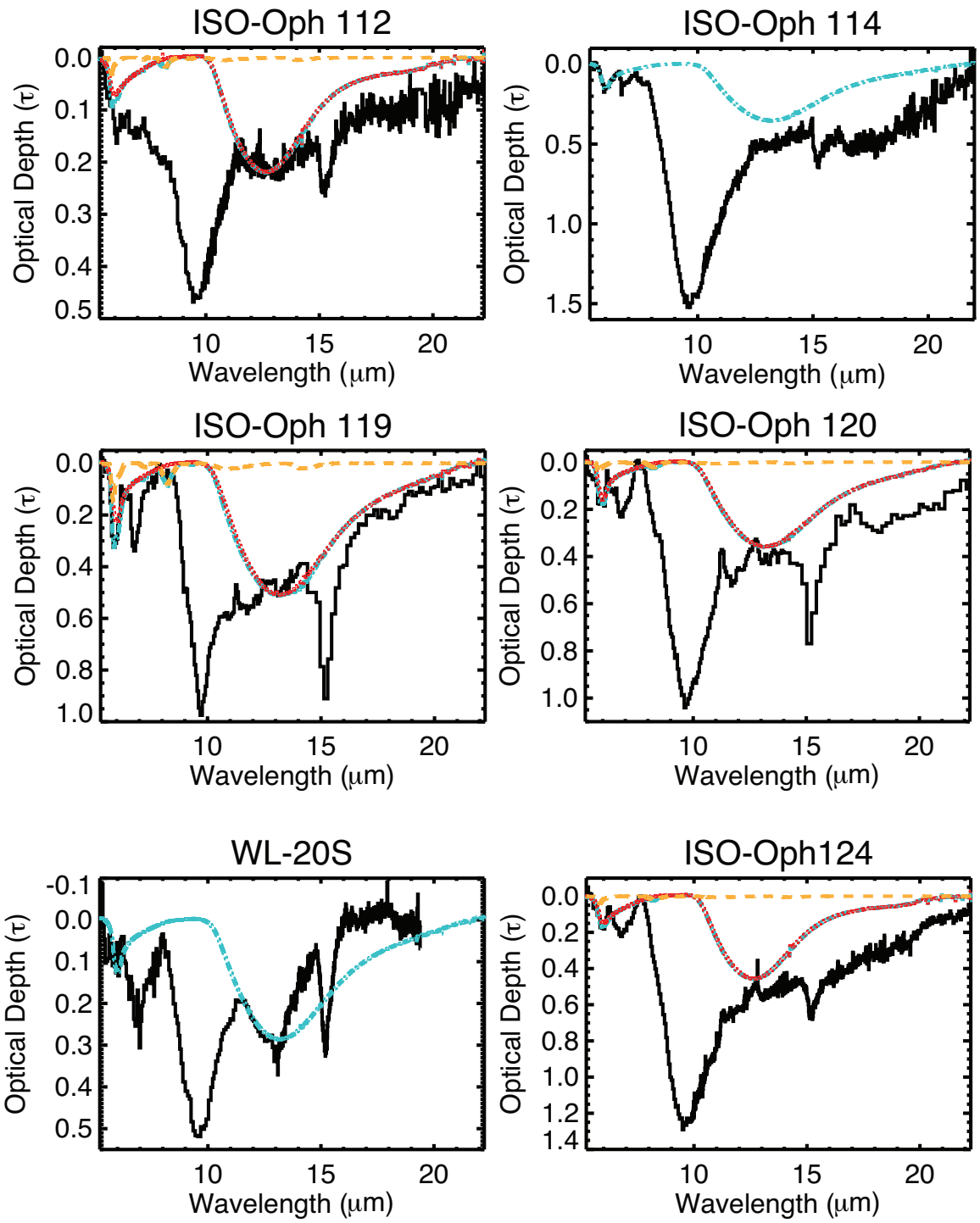

Figure 4.2 Optical depths with best fit laboratory spectra for H_2O. (cont.)

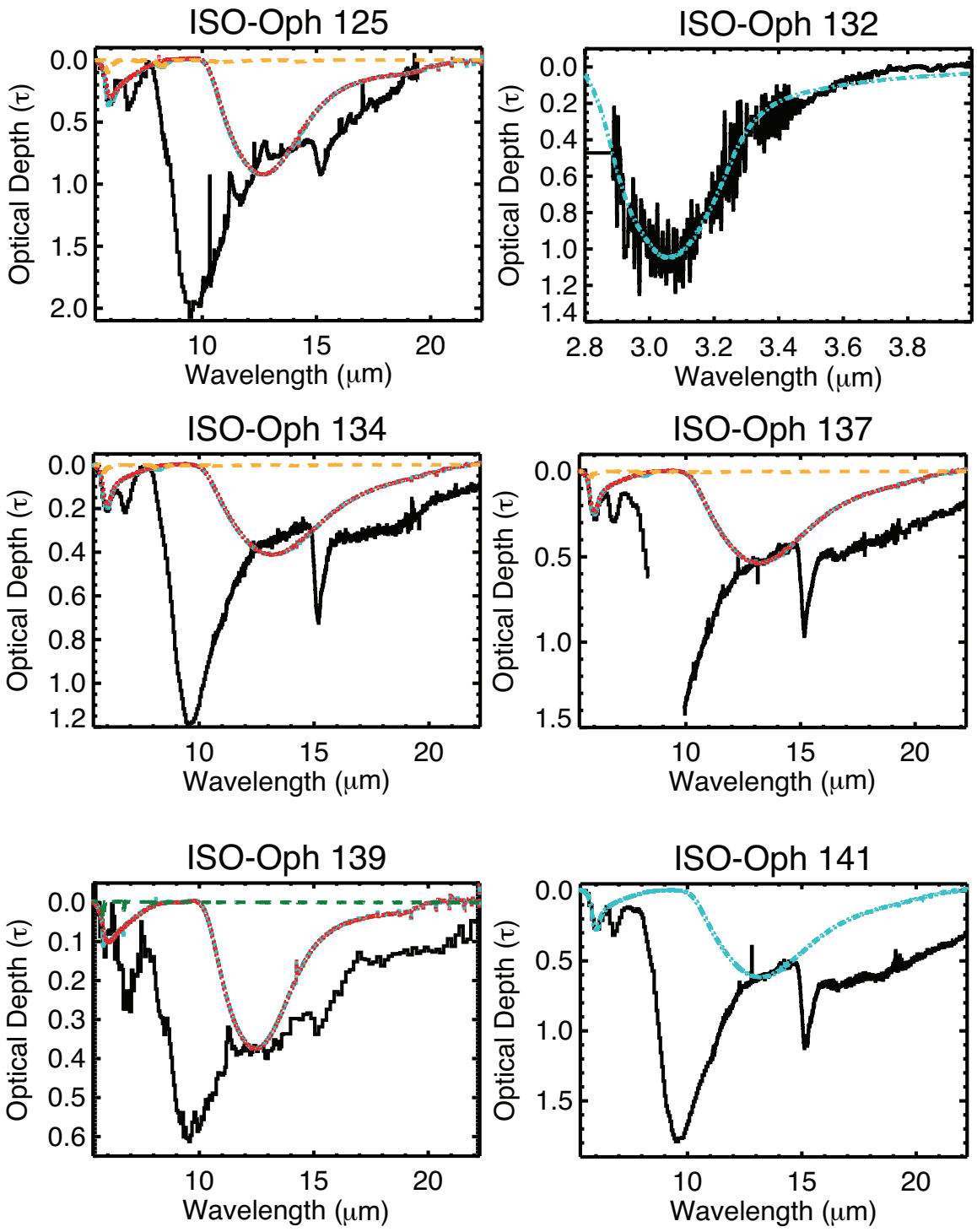

Figure 4.2 Optical depths with best fit laboratory spectra for H_2O. (cont.)

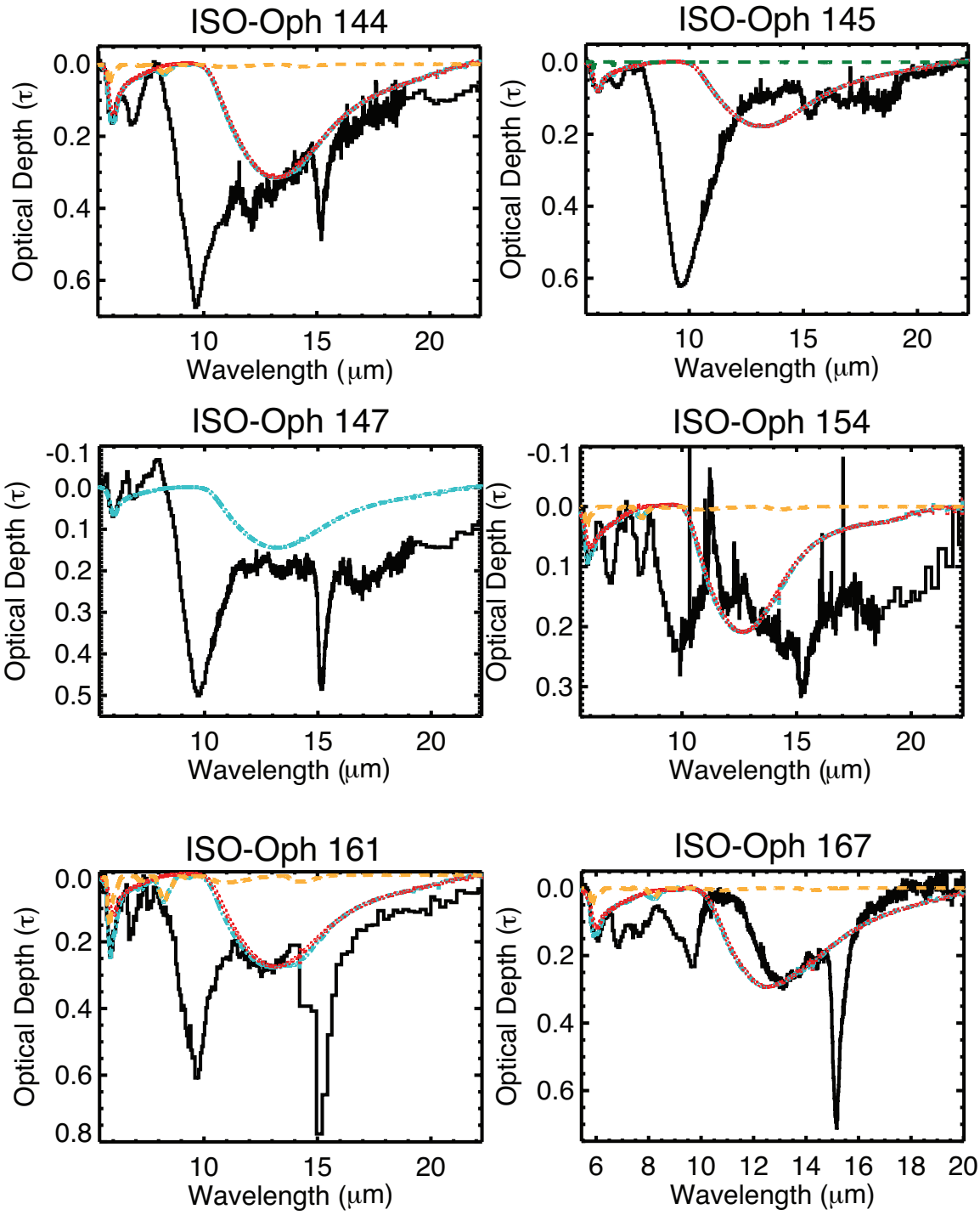

Figure 4.2 Optical depths with best fit laboratory spectra for H_2O. (cont.)

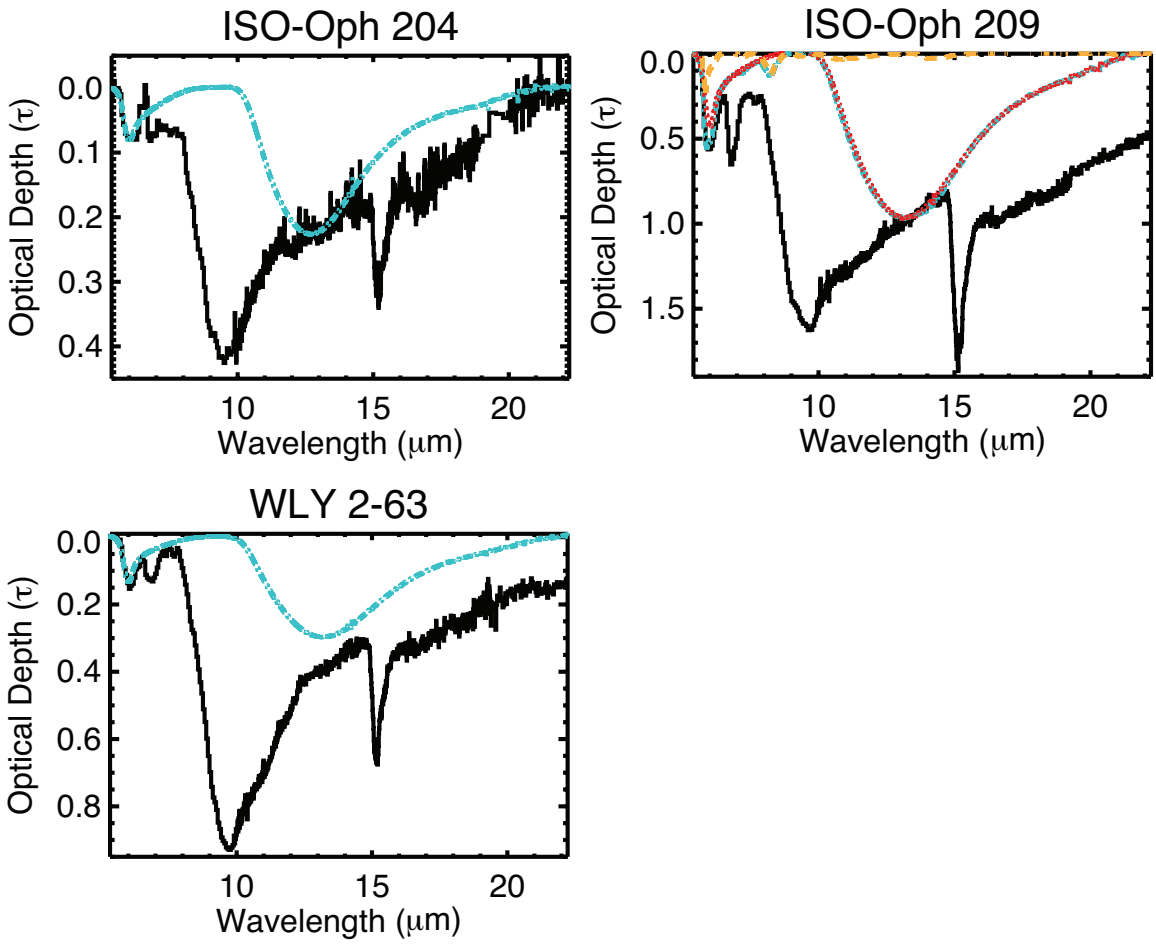

Figure 4.2 Optical depths with best fit laboratory spectra for H_2O. (cont.)

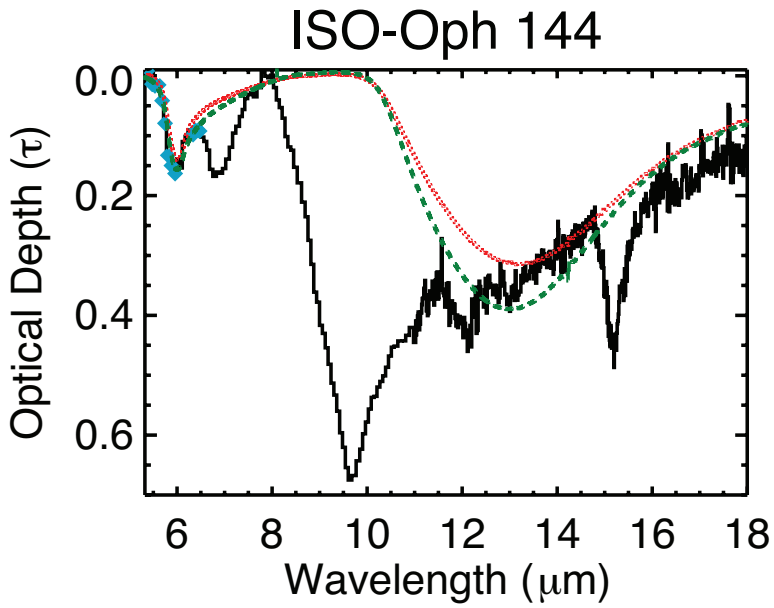

Figure 4.3 The spectrum for ISO-Oph 144 is the solid black line. The portion of the spectrum used to determine the best laboratory spectrum is overplotted as the teal diamonds. Notice that after removing the PAH emission at 6.26 μm, either cold H_2O (red dotted line) or warm H_2O (green dashed line) provide sufficient fits at 6 μm. In these cases, we considered the laboratory spectrum fit at 13 μm, and chose the laboratory spectrum consistent at both 13 μm and 6 μm. We emphasize, however, that the uncertainty in the continuum at 13 μm is large, and further study is needed to confirm the temperature of the ice.

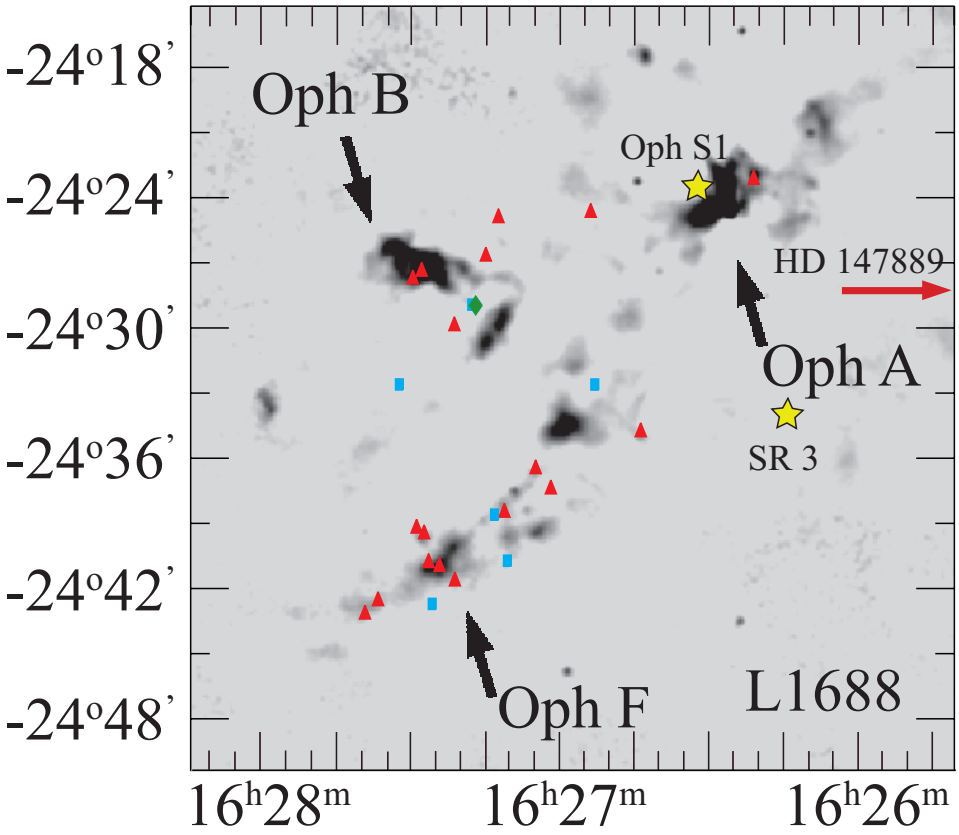

Figure 4.4 The location of our sources according to the temperature of the 6 μm feature are shown. Red triangles indicate sources with a cold ice feature ($\leq$50 K), blue squares are sources with a warm ice feature (>50 K) and the green diamond represents the location of ISO-Oph 124, which has a predominately warm H_2O component, but the temperature of the HCOOH component could be either warm or cold.

4.1.2.2. CO_2 ice. The optical depths and best laboratory mixtures for the bending mode of CO_2 are presented in Figure 4.5. Again, we note that other laboratory mixtures may give a comparable fit, but we present the mixture with the best χ^2. We can, however, determine which sources had better laboratory fits if the annealed (crystalline) component was included, 61% of those for which high resolution data were available (Figure 4.6). There were an additional two sources for which the crystalline fit was comparable to the polar/apolar fit, ISO-Oph 108 and WL-20W. The sources with a crystalline component and the sources without a crystalline component are scattered throughout the cloud, but there is a cluster of annealed sources just west of the Oph F core. In fact, unlike the

6 μm ice feature, a location near a dense core does not seem to shield sources from the radiation needed for annealing; there are annealed and non-annealed sources close to both the Oph F and Oph B cores as well as annealed and non-annealed sources in less dense regions. There are two sources that have a warm 6 μm ice component and an annealed CO_2 component: WL 20S and ISO-Oph 204, which have Class I and Class II SEDs, respectively. The scatter of sources with a crystalline component throughout the cloud and the two sources with warm H_2O and CO_2 may indicate that the warm ices are located near the YSO rather than in the surrounding molecular cloud, and that the warming is due to the local YSO rather than other nearby objects. There are two sources dominated by cold 6 μm and CO_2 ice features: ISO-Oph 132 and ISO-Oph 144, which have Class II and flat SEDs, respectively. In the case of ISO-Oph 132, the temperature was determined using the 3 μm stretching mode of H_2O. However, for ISO-Oph 144, both warm H_2O and cold H_2O give similar fits at 6 μm, with cold H_2O giving a slightly better reduced χ^2 of 2.572 compared to the reduced χ^2 of 3.277 for warm H_2O. In addition, cold ice for ISO-Oph 144 was chosen by comparing the two fits at 13 μm. Warm H_2O ice overestimates the absorption at 13 μm, but cold H_2O ice does not (see § 4.1.2.1). If the ices are located near the young star, this may be evidence that the temperature of the ice does not depend on the evolutionary state predicted by the SED. If it did, we would expect Class II sources to have warm ice since the YSO is more evolved and more likely to heat the surrounding ice. While we do not have enough data to draw a conclusion in this case, it would interesting for further study. Sources in L1688 fit by warm ice at 6 μm and annealed CO_2 ice (blue squares) or cold 6 μm and CO_2 ice (green triangles) are circled in Figure 4.6. We also put a circle with a line through it on top of the three sources located in L1688 for which the crystalline component composes more than 50% of the CO_2 ice. There are two sources located in L1689 which fit these criteria that are not included in Figure 4.6. ISO-Oph 209 has a crystalline component comprising more than 50% of the CO_2 ice and ISO-Oph 204 has a warm CO_2 and H_2O ice components. Although the two sources closest to the three most massive objects have a crystalline CO_2 component, they are dominated by cold ice at 6 μm. There are also sources that do not have a

crystalline component that are closer to those intermediate-mass YSOs than YSOs that do have a crystalline component. Therefore, it is improbable that the three intermediate-mass sources have a significant effect on the temperature of either the H_2O or CO_2 ice throughout the entire cloud. It is more likely that the annealing is due to the young star itself. If this is the case, we would not expect differences in the CO_2 ice profiles for different low mass star forming regions. Indeed, if we compare the percentage of sources in Taurus that show the signature of annealing: the double-peak structure, with the percentage in Rho Oph, they are similar.

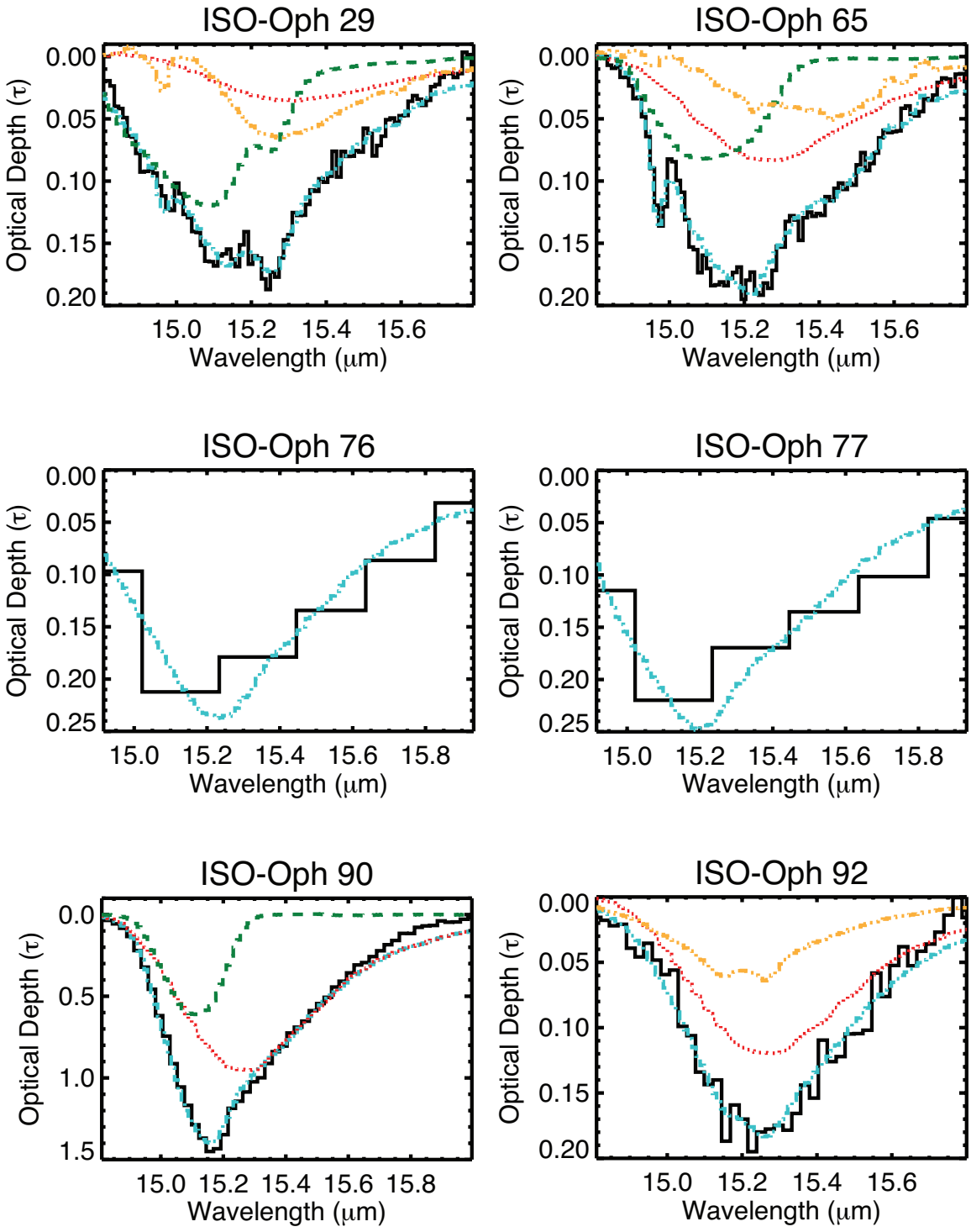

Figure 4.5 Optical depths are shown with best fit laboratory spectra for the bending mode of CO_2. The data are the solid black line. The polar, apolar, and crystalline laboratory components are the red dotted line, the green dashed line, and the orange dot-dot-dashed line, respectively. The sum the components is the total laboratory spectrum, and is shown as the teal dot-dashed line. Only the complete laboratory spectrum is shown for low resolution sources

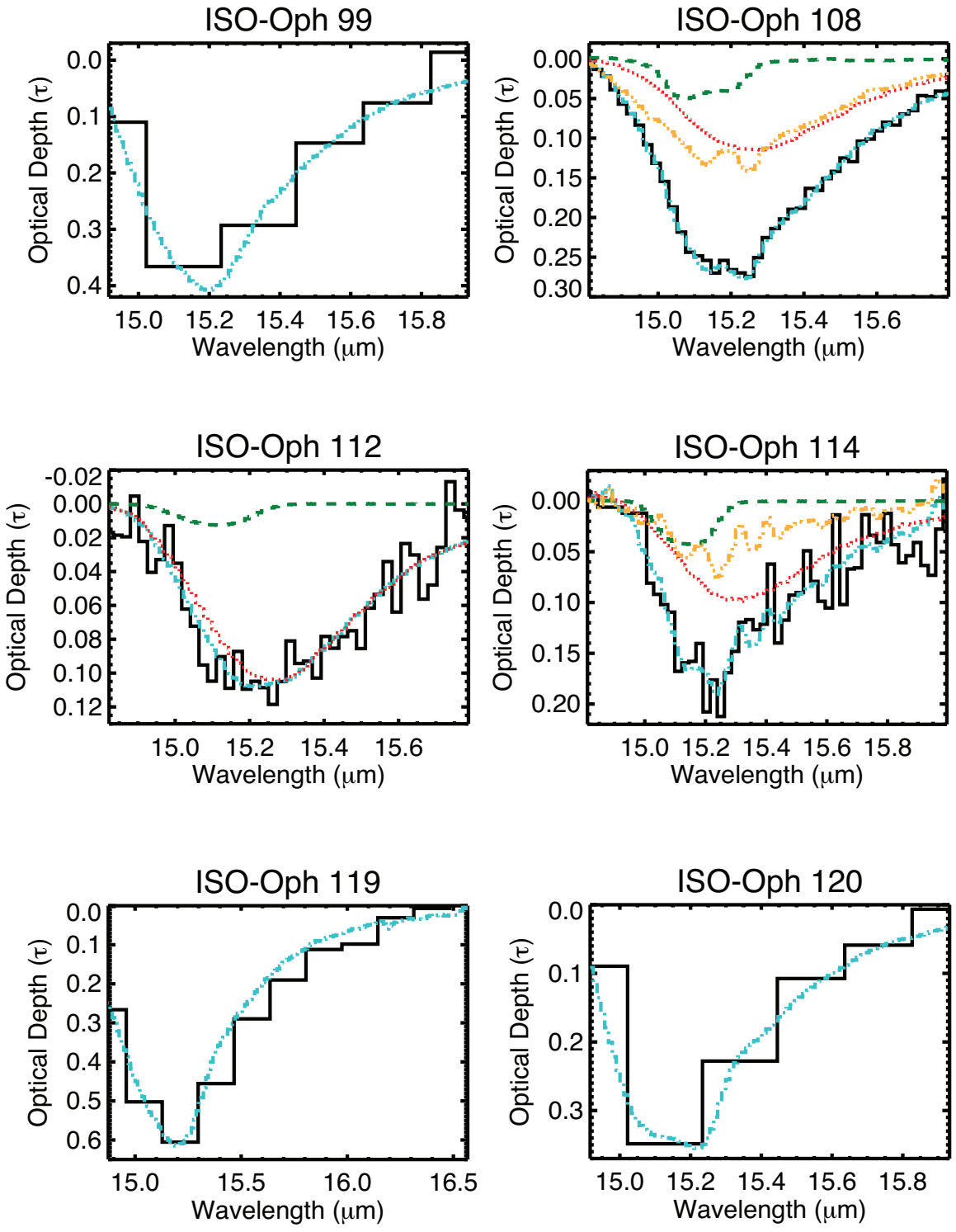

Figure 4.5 Optical depths are shown with best fit laboratory spectra for the bending mode of CO_2. (cont.)

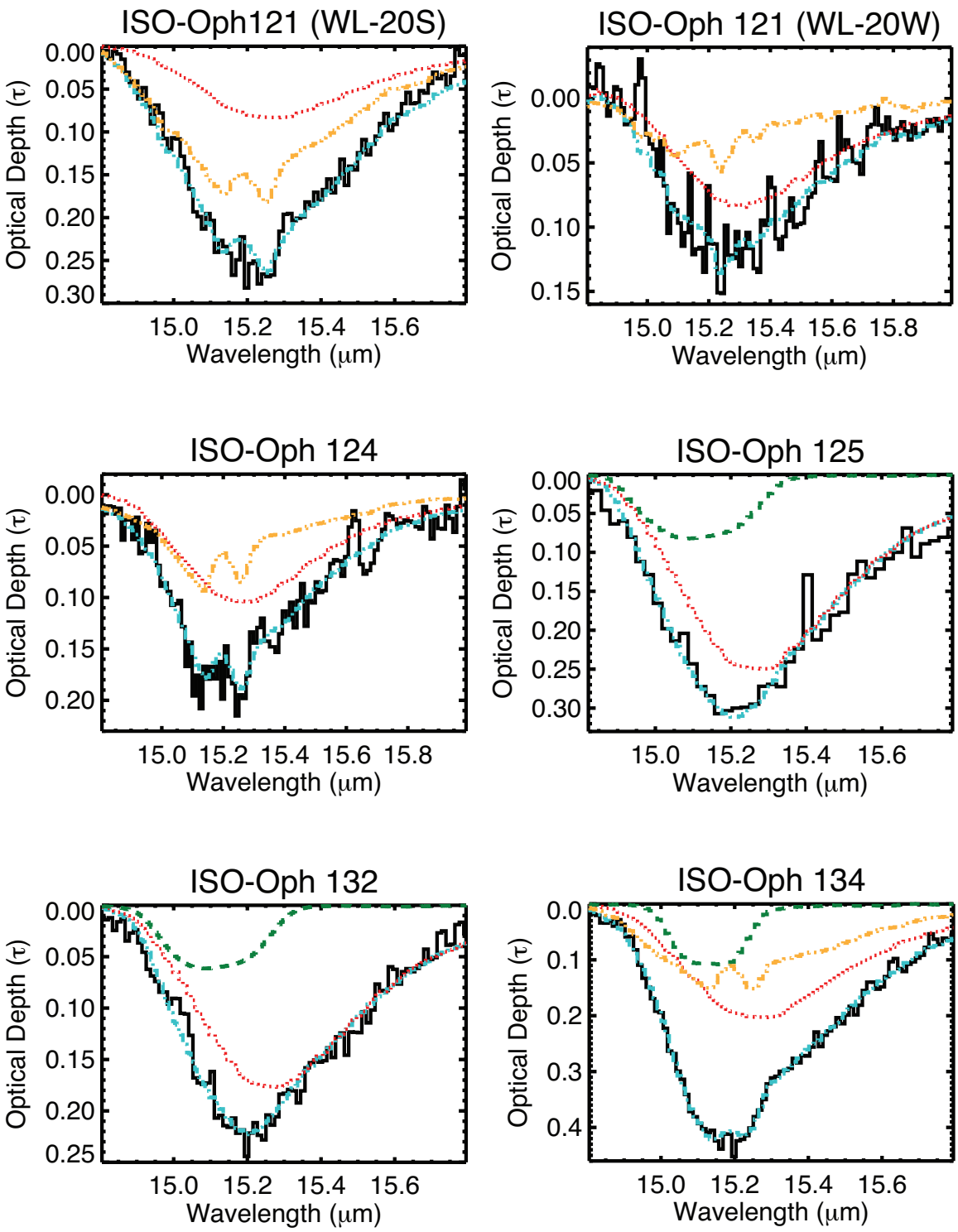

Figure 4.5 Optical depths are shown with best fit laboratory spectra for the bending mode of CO_2. (cont.)

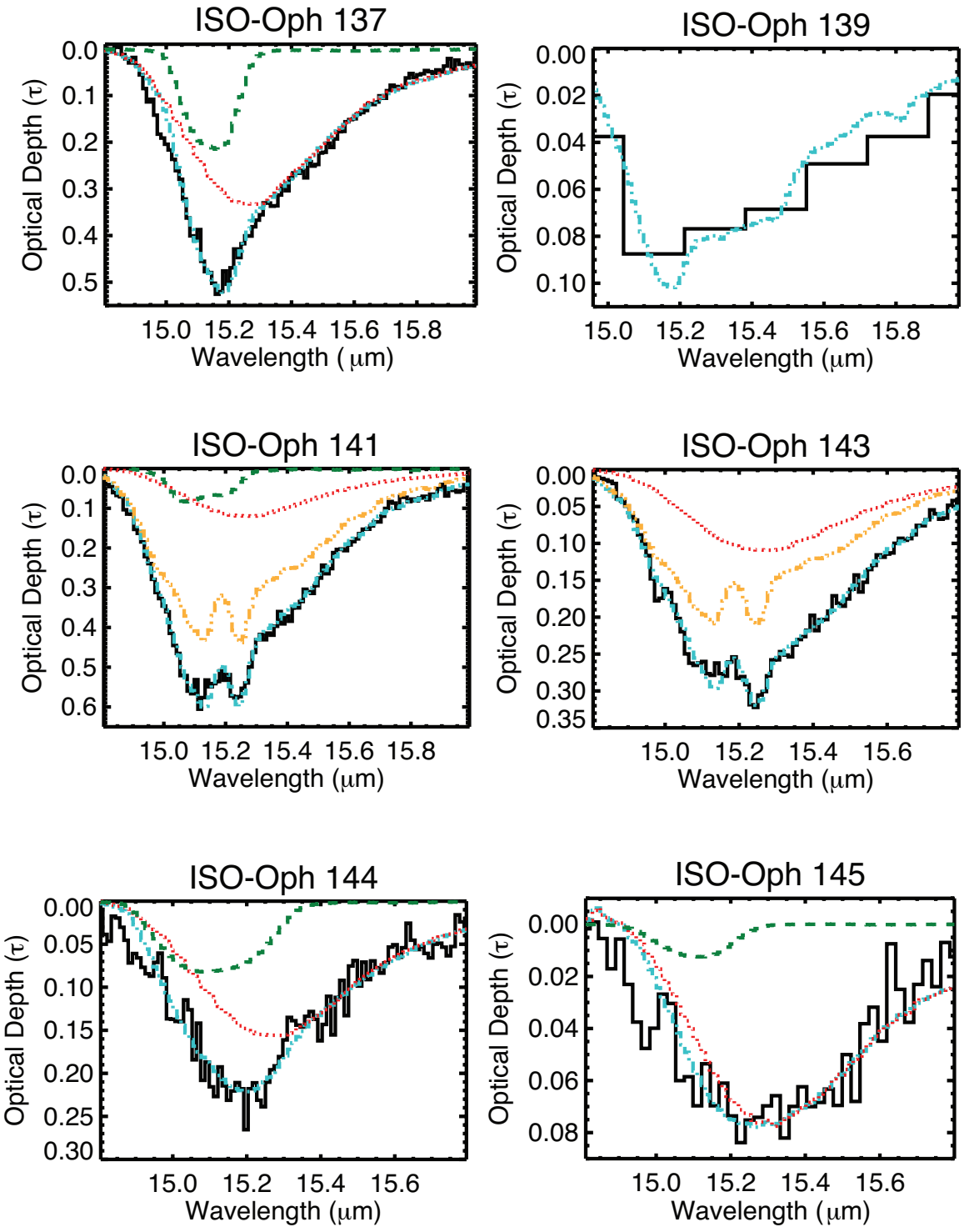

Figure 4.5 Optical depths are shown with best fit laboratory spectra for the bending mode of CO_2. (cont.)

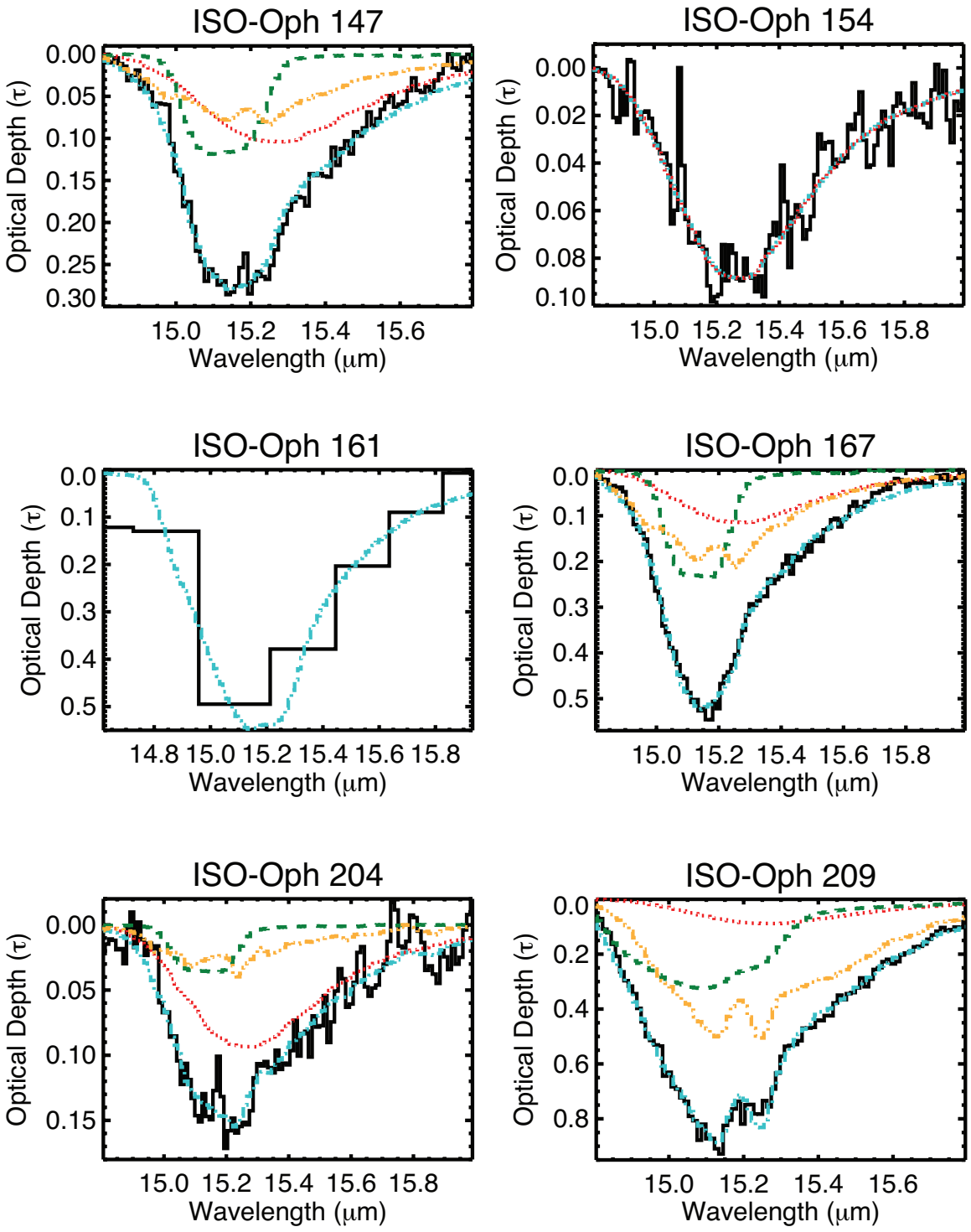

Figure 4.5 Optical depths are shown with best fit laboratory spectra for the bending mode of CO_2. (cont.)

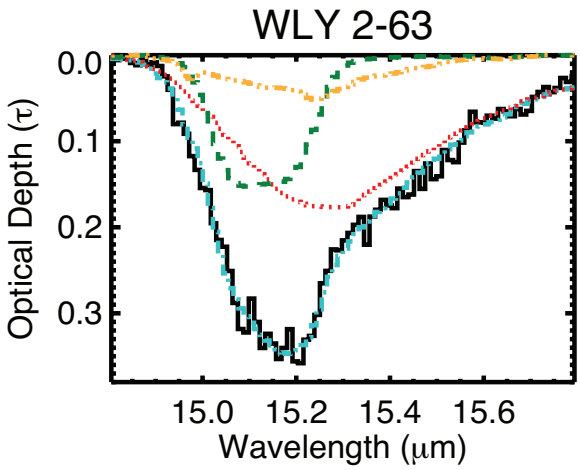

Figure 4.5 Optical depths are shown with best fit laboratory spectra for the bending mode of CO_2. (cont.)

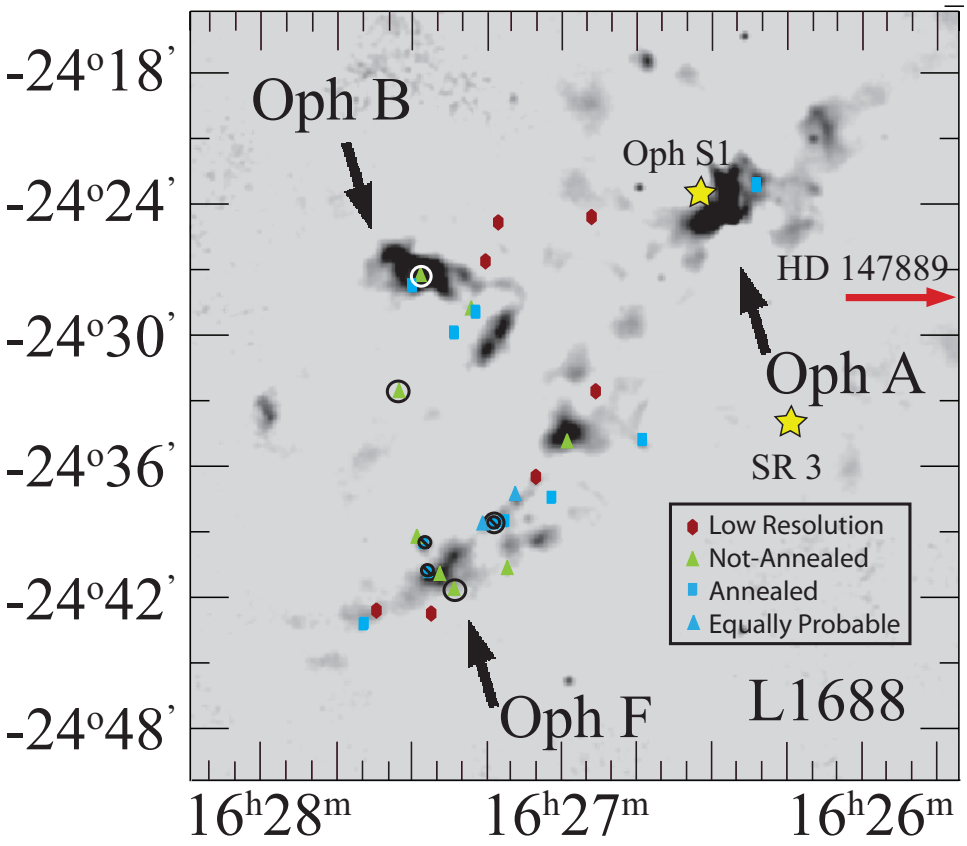

Figure 4.6 Sources which are not annealed sources are the green triangles and sources that have an annealed (crystalline) component are the blue rectangles. Sources for which only low resolution CO_2 data are available are the red hexagons. The source positions are plotted on top of the SCUBA 850 μm map presented in § 4.1.1. Note that there are both annealed and non-annealed sources located radially near dense cores and in regions farther from the dense cores. Sources that have a circle with a line through it overplotted on the blue square have an annealed component >50%. Sources with similar 6 μm and CO_2 ice temperatures–either non-annealed CO_2 and cold H_2O or annealed CO_2 and warm H_2O are circled. There is one source that has an annealed component composing >50% and warm H_2O ice, WL-20S.

4.1.3. Abundance of CO_2. In addition to considering differences in the column densities and profile shapes of H_2O and CO_2, we calculated the abundance of CO_2 for each of our sources, which is presented in Table 4.1. Again, probing different sight lines can give an indication of how molecules are created or destroyed in the solid phase. For example, Oberg et al. (2011) suggested that objects subjected to the most local UV and thermal radiation, massive YSOs,

have the lowest abundance of CO_2 (13%), while sight lines that probe unprocessed material, background objects, have the highest abundance of CO_2 (38%). Low mass YSOs, in which material may be partly processed, fall in the middle (29%) (Oberg et al., 2011). Low mass YSOs in Rho Oph have a weighted mean CO_2 abundance of 18.6%±0.4%. This is similar to the abundance (17.0%±0.1%) toward all low mass YSOs in five star forming regions, Perseus, Corona Australis, Rho Oph, Serpens, and Taurus, using both column densities from this work and previously published column densities, but lower than that toward low mass YSOs found by Oberg et al. (2011). However, Oberg et al. (2011) did not use the Cook et al. (2011) or Zasowski et al. (2009) data in their results, and the Zasowski et al. (2009) data show a lower average abundance than the Oberg et al. (2011) average toward 16 low mass YSOs in Taurus.

Assuming CO_2 and H_2O are linearly correlated and using this work, as well as that in Cook et al. (2011), Zasowski et al. (2009), Pontoppidan et al. (2008), Nummelin et al. (2001), and Bergin et al. (2005) toward low mass YSOs in Perseus, Taurus, Rho Ophiuchi, Corona Australis, and Serpens, we find a strong linear correlation between CO_2 and H_2O, with a slope of 0.26±0.01. This correlation was determined using the Pearson product-moment coefficent, r. It was calculated using the idl function, *correlate.pro*, and only uses the column densities of H_2O and CO_2. It is not weighted with the error in the colunn density. As a general rule, the closer the correlation coefficient is to 1 or -1, the stronger the correlation, which indicates that the data are linearly related. A Pearson r of 0 indicates no correlation between two sets of data. However, the number of data points also has an effect on the strength of the correlation. A correlation coefficient of r = 0.92 for six or more data points has a 2% probability of occuring randomly (see Bevington and Robinson (2003)). Individual CO_2 abundances from this compilation for low mass YSOs range from 7% - 65%, indicating scatter in the data. In spite of this large range, the data show a strong correlation, r = 0.93. The comparison of $N(CO_2)/N(H_2O)$ for our sources in Rho Oph is shown in Figure 4.7. The slope is 0.15±0.04 with r = 0.62, which indicates a strong correlation, but certainly not as strong as the result for low mass YSOs in general. The intercept is zero within the uncertainty, and there is a large amount of scatter present in the data. In fact,

CO_2 abundances range from as little as 8% to as much as 54%. The Zasowski et al. (2009) data also show a tight linear relation between the column densities of H_2O and CO_2 for Taurus, but they do not quantify it. Likewise, Cook et al. (2011) find a strong correlation between CO_2 and H_2O for both YSOs in Taurus and low mass YSOs toward several star forming regions, and report a slope of the correlation line of 0.29 ± 0.01 and 0.28 ± 0.03, respectively.

While our average abundance is consistent with that of Zasowski et al. (2009) and our data show a strong correlation between the column densities of CO_2 and H_2O, this correlation is not as strong as that toward Taurus and the Cook et al. (2011) sample, and it has a shallower slope than that reported by Cook et al. (2011) and a lower abundance than that toward low mass YSOs reported by Oberg et al. (2011). The average abundance of CO_2 toward the single molecular cloud, Rho Oph, is closer to the value cited toward high mass YSOs reported by Oberg et al. (2011), 12-22% than it is toward their value of low mass YSOs, 22-35%. We will compare linear correlations and average abundances toward low mass YSOs in other star forming regions in § 4.1 in order to determine if this lower abundance is unusual or the norm.

Table 4.1. Abundances, $N(CO_2)/N(H_2O)$.

Source	Abundance	Uncertainty
ISO-Oph 29	0.17	0.02
ISO-Oph 65	0.20	0.02
ISO-Oph 76	0.16	0.03
ISO-Oph 77	0.10	0.04
ISO-Oph 92	0.34	0.03
ISO-Oph 99	0.30	0.08
ISO-Oph 112	0.14	0.03
ISO-Oph 114	0.12	0.02
ISO-Oph 119	0.37	0.05
ISO-Oph 120	0.27	0.04
WL-20S	0.24	0.04
ISO-Oph124	0.11	0.02
ISO-Oph125	0.08	0.01
ISO-Oph 132	0.22	0.02
ISO-Oph 134	0.26	0.02
ISO-Oph 137	0.21	0.01
ISO-Oph 139	0.08	0.02
ISO-Oph 141	0.25	0.02
ISO-Oph 143	0.18	0.01
ISO-Oph 144	0.18	0.04
ISO-Oph 145	0.13	0.01
ISO-Oph 147	0.25	0.01
ISO-Oph 154	0.12	0.03
ISO-Oph 161	0.54	0.13
ISO-Oph167	0.25	0.01
WLY2-63	0.25	0.02
ISO-Oph 204	0.21	0.04
ISO-Oph 209	0.24	0.02

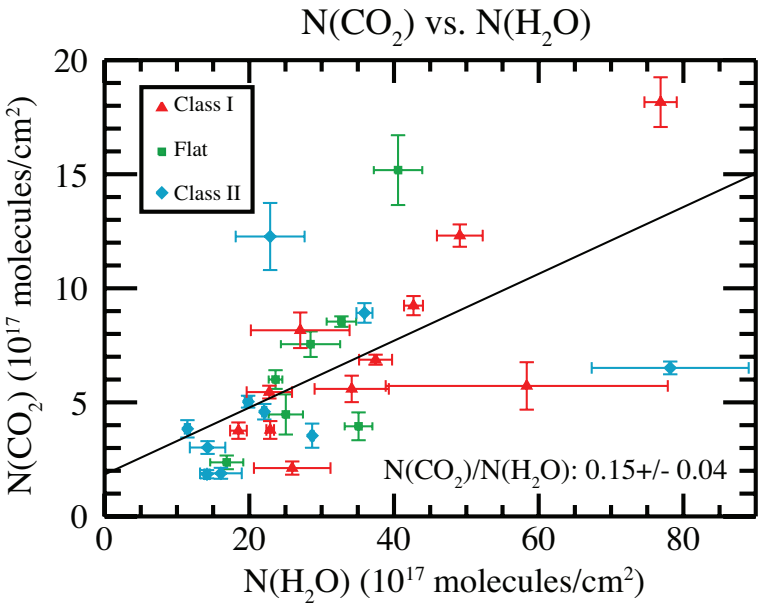

Figure 4.7 This abundance plot shows the column density of CO_2, $N(CO_2)$ versus the column density of H_2O, $N(H_2O)$. A linear least squares fit was performed, and it was found that slope of the correlation line is 0.15 $\pm$0.04. Since H_2O is less volatile than CO_2, one would expect to see a negative y-intercept. The positive intercept in this case is not significant; it is zero within 2σ.

4.1.4. High $N(CO_2)/N(H_2O)$. We found some sources in Rho Oph with a high abundance, and there are other regions (see for example Serpens) with sources that have high abunandces. Thus, we first consider the location of sources with a high abundance, that is, those which lie 3σ above the average abundance, or $N(CO_2)/N(H_2O) > 20\%$, Figure 4.8. Pontoppidan (2006) studied five sources near the Oph-F core, and reported that the abundance increased with radial distance toward the core. This would suggest that the YSOs most abundant in CO_2 are located closest to the center of the dense core. An interesting hypothesis then would be that the coldest, densest regions in the molecular cloud are more efficient at making CO_2. However, our data do not support this hypothesis. As is shown in Figure 4.8, more abundant YSOs do not correlate with proximity to cold dense cores. For example, ISO-Oph 144 and ISO-Oph 147, which are radially located within the Oph B core, have abundances of $\sim$18% and $\sim$25%. In fact, one of the sources with the lowest abundance of $\sim$8%, ISO-Oph 139, is radially located on a dense region in the Oph F core. Its nearest companion, ISO-Oph

137, has an abundance of ∼21%, and is also radially located on a dense region in the same core. The four sources with the highest abundance are circled, ISO-Oph 92 (mid-right), ISO-Oph 99 (mid-left), ISO-Oph 119 (top), and ISO-Oph 161 (lower-left), and are not radially located near the dense cores. Furthermore, the abundances reported by Pontoppidan et al. (2008) for the same sources as the 2006 paper no longer support the correlation with radial distance to the Oph-F core, even though they are within 3σ of the original values. With the new data from Pontoppidan and our larger sample size, we can propose that the abundance of CO_2 is not correlated with radial distance to the cores of Rho Oph.

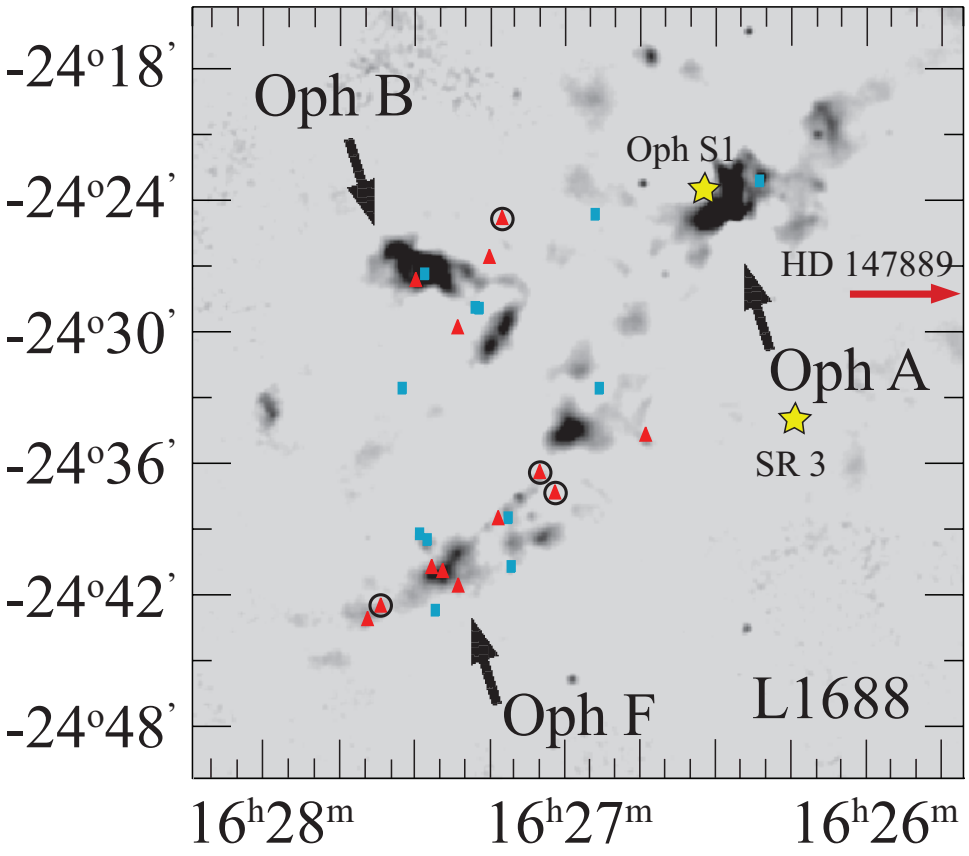

Figure 4.8 YSOs with $N(CO_2)/N(H_2O) > 3\sigma$ (20%) of the average abundance plotted on a map of L1688 in Rho Oph created at 850 μm with SCUBA on JCMT. The dark areas are cold, dense regions. The Oph A, B, and F cores are labeled. The symbols are the same as those in Figure 4.6. The four sources with the highest abundances are circled. Note that sources with a high abundance are not necessarily located near the center of the dark cores.

4.1.5. Evolutionary State. In addition to investigating the abundance with YSO location, we also studied whether the abundance of CO_2 correlates with evolutionary state. Traditionally, the evolutionary state of a YSO is determined by calculating the spectral index, essentially the slope, α_{2-25} between 2-25 μm:

$$\alpha_{2-25} = log\frac{\lambda_2 F_{\lambda 25}}{\lambda_{25} F_{\lambda 2}} / log\frac{\lambda_{25}}{\lambda_2} \tag{6}$$

where $F_{\lambda 25}$ and $F_{\lambda 2}$ are the fluxes at 2 μm (λ_2) and 25 μm (λ_{25}) (McClure et al., 2010). Objects that are still surrounded by an envelope have a spectral index, $\alpha \geq 0.3$, and have SEDs referred to as Class I. Objects that are characterized by a disk but still have a substantial envelope have flat-spectrum SEDs, and $-0.3 \leq \alpha < 0.3$. Class II SEDs have a spectral index, $-2.0 \leq \alpha < -0.3$, and correspond to objects with a substantial disk and very little envelope. The final stage of YSO, one in which very little circumstellar material is left, have $\alpha < -2.0$. At this stage planet formation is mostly complete and the stellar winds clear out the remaining disk, see for example, Lada (1987), Wilking et al. (1989) and Greene et al. (1994). Typically the fluxes at 2 μm and 25 μm are determined using broadband photometry. In the past this was dictated by the limited availability of flux measurements. The important consideration is that the spectral index be determined at wavelengths redder than the peak flux of the SED of the star, the portion of the SED from the dust surrounding the star. Technology has improved and more instruments have been developed, so we now have photometry available for a greater wavelength range, and even a full spectrum in some regions of the infrared. Therefore, we are now able to better characterize the SEDs of YSOs. For objects in Taurus and a few in Rho Oph, the spectral index between 2 μm and 25 μm sufficiently samples the decreasing flux beyond the peak of the SED. However, this is not the case for all objects in Rho Oph. Some of these objects peak at 5 μm. Therefore, McClure et al. (2010) suggested calculating the spectral index between 5 μm and 12 μm, and showed that it is a sufficient method. They categorized the SEDs as being dominated by envelope, disk, or photosphere, similar to the original Class I, Class II, and Class III designations. Figure 4.9 has been adapted from McClure et al. (2010) to show the difference in the slope between 2-25 μm and

5-12 μm for CRBR 2422.8-3423, or ISO-Oph137 in L1688. The importance of characterizing the evolutionary state using an appropriate wavelength range is well demonstrated. In this case, the original method would suggest that this object would be characterized as Class I, or still surrounded by an envelope, whereas the method by McClure et al. (2010) would characterize the object as Class II or possibly Class III, an object surrounded by a disk with little remaining envelope. In this work we calculate the spectral index (Table 4.2) using the method of McClure et al. (2010), from 5 μm to 12 μm but use the traditional ranges to classify the SEDs of our objects as Class I, flat-spectrum, Class II, or Class III. The fluxes at 5 μm and 12 μm were determined using polynomial fit to the continuum in §3. This method is improved, but can still lead to an inaccurate classification. For example, the SED of an object with an edge-on disk and very little envelope, i.e., Class II/III could still have a positive slope beyond 5 μm due to the high extinction from the disk, and thus could be misclassified.

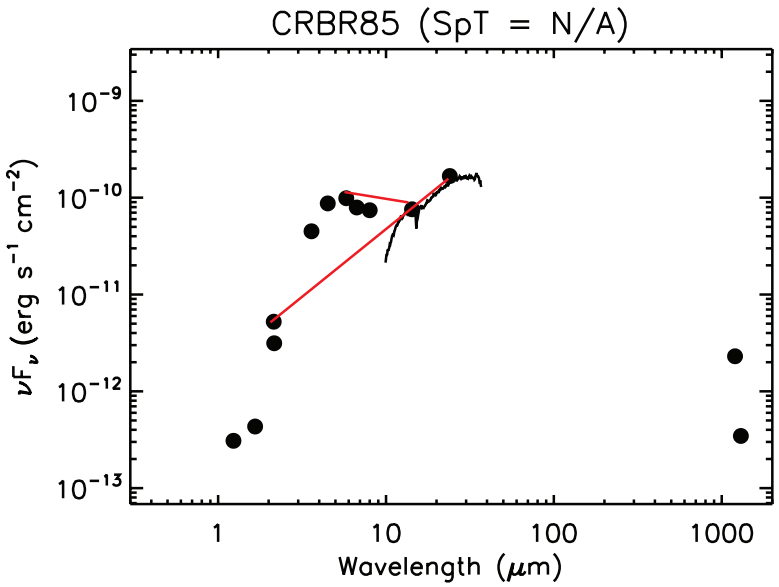

Figure 4.9 This figure showing the SED for CRBR 85 from McClure et al. (2010) has been adapted to show the importance of wavelength choice in the determination of the spectral index. Note that the slope from 2-25 μm is positive, but the slope from 5-12 μm is negative which results in drastic differences in classification. The 2-25 μm slope indicates an embedded Class I source, but the 5-12 μm slope indicates a spectrum dominated by a disk. We have chosen to use the method of McClure et al. (2010) to determine the spectral index, which uses wavelengths beyond the peak of the SED.

Table 4.2. Spectral index, α, from 5-12 μm and visual extinction, A_V.

Source	Spectral Index, α	Uncertainty	Visual Extinction[1], A_V
ISO-Oph 29	1.455	0.001	—
ISO-Oph 65	0.676	0.043	13.7
ISO-Oph 76	0.618	0.061	—
ISO-Oph 77	2.199	0.133	32.8
ISO-Oph 92	-0.482	0.089	—
ISO-Oph 99	2.011	0.035	—
ISO-Oph 108	—	—	41.1
ISO-Oph 112	-0.194	0.080	29.5
ISO-Oph 114	-0.850	0.011	47.5
ISO-Oph 119	-0.084	0.235	39.7
WL-20S	1.964	0.023	—
ISO-Oph 120	-0.269	0.152	24.7
ISO-Oph124	0.279	0.024	31.4
ISO-Oph125	-1.500	0.061	49.2
ISO-Oph 132	-1.226	0.018	25.0
ISO-Oph 134	-0.109	0.058	55.0
ISO-Oph 137	0.464	0.002	—
ISO-Oph 139	1.114	0.059	27.3
ISO-Oph 141	0.573	0.020	44.4
ISO-Oph 143	1.669	0.026	37.8
ISO-Oph 144	0.125	0.126	21.1
ISO-Oph 145	-0.463	0.045	24.7
ISO-Oph 147	-0.815	0.021	24.1
ISO-Oph 154	-0.302	0.044	15.2
ISO-Oph 161	-0.323	0.020	34.8
ISO-Oph167	-0.661	0.004	32.6
WLY2-63	-0.285	0.017	23.3
ISO-Oph 204	-0.645	0.014	12.9
ISO-Oph 209	0.777	0.004	—

[1]Wilking, personal communication

Using the classification described above, we have roughly equal numbers of sources with Class I and Class II SEDs, 11 and 10, respectively. We classify 7 of our sources with flat-spectrum SEDs, and we do not have any sources with Class III SEDs, as is expected since at that stage the bulk of the ice-bearing material has been removed and we chose sources with ice for our sample. We show the dependence of the abundance with respect to the spectral index of the SED of the YSO in Figure 4.10. A horizontal line at 20% marks the 3σ deviation from the weighted mean of the abundance. There is a peak in abundance for YSOs with Flat and early Class II SEDs. It seems that the transition from a flat spectrum to a Class II spectrum may result in an enhancement in CO_2 abundance, although not all YSOs with Flat/Class II spectra produce a higher abundance of CO_2. A comparison of the column density of CO_2 with the spectral index (Figure 4.11) shows a similar trend; some sources with SEDs that show a transition from Flat

to Class II have a higher column density of CO_2. In this case, we propose the activation of an additional formation route. The energy necessary to activate the production of additional CO_2 could come from several mechanisms that are known to occur during the transition from Flat to Class II. These include the onset of deuterium burning and stellar winds.

The trend of higher abundances of CO_2 for YSOs with Flat or Class II SEDs is also illustrated for Taurus in the Zasowski et al. (2009) study and toward several star forming regions in the Cook et al. (2011) study. However, Zasowski et al. (2009) they define their spectral index between 7 μm and 30 μm and Cook et al. (2011) define their spectral index between 2 μm and 25 μm. The Zasowski et al. (2009) study does not have any YSOs with an abundance 3σ above their reported average. However, four of the five sources with the largest abundance have flat SEDs, and the fifth has a Class II SED. For the Cook et al. (2011) study, there are six YSOs that have abundances greater than 3σ above their reported average. Four of those six have Flat SEDs, and two have Class I SEDs. While these other studies seem to support our conclusion that the abundance of CO_2 becomes enhanced during the transition stage between YSOs with a Flat SED and those with a Class II SED, it would be necessary to calculate the spectral index in the manner presented in this study in order to fully draw conclusions.

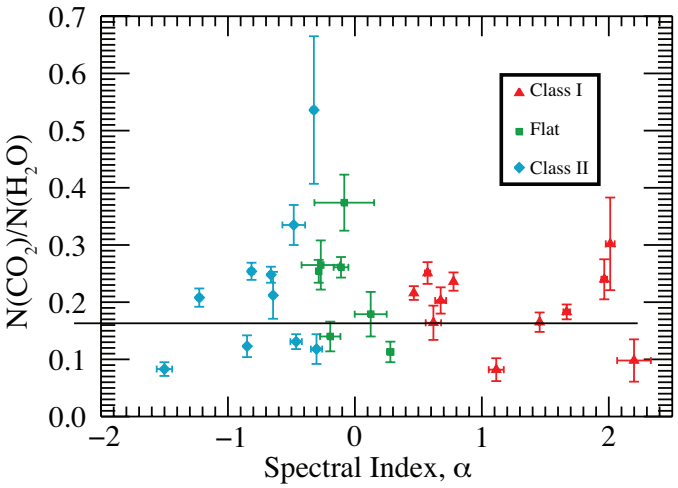

Figure 4.10 The abundance, $N(CO_2)/N(H_2O)$ is plotted on the y-axis, and the spectral index, α_{5-12} is plotted on the x-axis. Sources that fall above the line drawn at 20% have a high abundance ($>3\sigma$ from the average). YSOs with a Class I SED are the red triangles, YSOs with a Flat SED are green squares, and YSOs with Class II SEDS are the blue triangles.

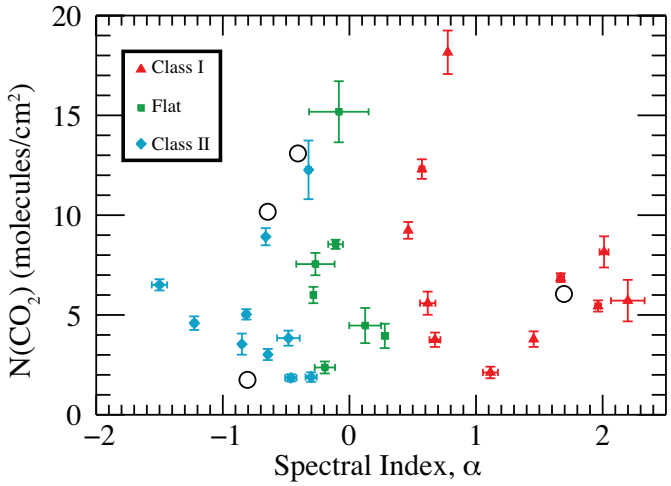

Figure 4.11 The column density of CO_2, $N(CO_2)$, is plotted on the y-axis, and the spectral index, α_{5-12} is plotted on the x-axis. YSOs that have an abundance of CO_2 greater than 20% ($>3\sigma$) are circled. YSOs with a Class I SED are the red triangles, YSOs with a Flat SED are green squares, and YSOs with Class II SEDS are the blue triangles.

4.1.6. Visual Extinction. Finally, we will look for a correlation between abundance and visual extinction, A_V. For objects with known spectral types, visual extinctions were calculated using the method of Erickson et al. (2011). The visual extinction for our sources ranges from $24.1 < A_V < 39.4$ (see Table 4.2). The potential correlation is shown in Figure 4.12. Note that there is significant scatter. Two sources with the lowest abundances, ISO-Oph 77 and ISO-Oph 125, have quite different extinctions, 32.8 and 49.2, respectively, and the source with the greatest abundance, ISO-Oph 161, has a moderate extinction of 34.8. We also considered the SED class of each source, using the same legend as Figure 4.10, and see that the extinction is uncorrelated with class as well. These non-correlations may indicate that a large portion of the H_2O and CO_2 ice is due to cold, unprocessed material in the intervening cloud. We also considered the column density of CO_2 with respect to visual extinction, A_V (Figure 4.13). As expected, the column density of CO_2 does increase with visual extinction. The correlation shows large scatter and does not show a general trend with SED class. Again, the lack of trend with SED class supports the conclusion that most of the CO_2 ice is located in the star-forming cloud material rather than close to the young star.

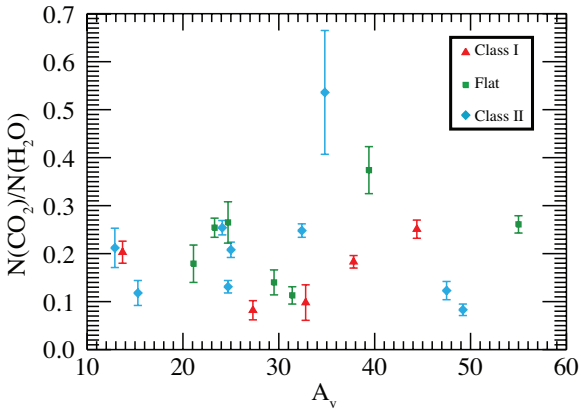

Figure 4.12 The abundance, $N(CO_2)/N(H_2O)$ is plotted on the y-axis, and the visual extinction, A_V is plotted on the x-axis. YSOs with a Class I SED are the red triangles, YSOs with a Flat SED are green squares, and YSOs with Class II SEDs are the blue triangles. Note the lack of correlation between abundance and extinction; r = 0.003.

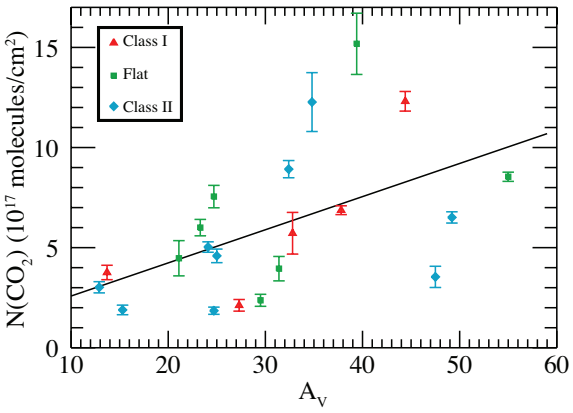

Figure 4.13 The column density of CO_2 is plotted on the y-axis, and the visual extinction, A_V is plotted on the x-axis. YSOs with a Class I SED are the red triangles, YSOs with a Flat SED are green squares, and YSOs with Class II SEDs are the blue triangles. While the column density of CO_2 roughly increases with respect to visual extinction, there is quite a bit of scatter.

4.1.7. CO_2 Component Analysis. Whittet et al. (2009) completed a study of background objects toward Taurus, Serpens, and IC 5146. While their sample includes only a few sources, it indicates that objects with pristine or unprocessed ices contain a large polar component of CO_2 ice, ∼85% and do not have a crystalline component. This is reasonable since unprocessed ices should not be crystalline. We calculated the percentage of each component with respect to the total column density of CO_2 (Table 4.3) so that the three components comprising CO_2 for YSOs in Rho Oph could be compared to that for background objects. As expected, all of our sources contained a polar component of CO_2 (the polar layer forms first on the grain), while six YSOs lacked an apolar component. We note that unlike the results toward background stars reported by Whittet et al. (2009), we have only six sources in which the polar component accounts for >80% of the CO_2 ice absorption and four sources in which the majority of the ice absorption is contributed by the crystalline component, which indicates these ices have undergone processing.

Table 4.3. Percentage of CO_2 components.

Source	Polar (%)	Apolar	Annealed
ISO-Oph 29	21.0	51.0	28.0
ISO-Oph 65	47.9	28.8	23.3
ISO-Oph 90	78.9	21.1	0.0
ISO-Oph 92	67.4	0.0	32.6
ISO-Oph 108	42.9	8.1	49.0
ISO-Oph 112	95.2	4.8	0.0
ISO-Oph 114	61.1	10.2	28.7
WL-20S	33.1	0.0	66.9
WL-20W	65.6	0.0	34.4
ISO-Oph 124	59.4	0.0	40.6
ISO-Oph 125	83.3	16.7	0.0
ISO-Oph 132	83.7	16.3	0.0
ISO-Oph 134	51.7	12.3	36.0
ISO-Oph 137	80.8	19.2	0.0
ISO-Oph 141	21.1	6.5	72.4
ISO-Oph 143	35.9	0.0	64.1
ISO-Oph 144	75.7	24.3	0.0
ISO-Oph 145	94.0	6.0	0.0
ISO-Oph 147	44.9	22.7	32.4
ISO-Oph 154	100.0	0.0	0.0
ISO-Oph167	27.9	25.5	46.6
ISO-Oph 204	67.0	11.5	21.5
ISO-Oph 209	10.6	32.9	56.5
WLY2-63	63.9	24.4	11.7

In addition, a comparison of the column density of each component of the CO_2 ice feature with that of H_2O was performed (Figures 4.14, 4.15, 4.16). We found that only the annealed (crystalline) component seems to be correlated with H_2O, with a slope of 0.16 ± 0.02, and a Pearson correlation coefficient of 0.90. The intercept is zero within the uncertainty. This is in direct contrast to the results of Cook et al. (2011), who report strong correlations between polar and apolar CO_2 and H_2O, and a weak correlation between crystalline CO_2 and H_2O. Although our sample size is small, we note that the sources with the largest column densities of both H_2O and crystalline CO_2 have Class I SEDs and that in general, those with Class II SEDs have a lower column density of both H_2O and crystalline CO_2.

There are two methods to create the double-peaked structure indicative of crystalline CO_2 (Pontoppidan et al., 2008): distillation of the apolar component, in which a CO_2:CO mixture is heated, sublimating the CO and leaving the CO_2, or a segregation process in which CO_2 is segregated from H_2O in the polar mantle. The former can proceed at low temperatures, 20 K - 30 K, while the latter needs higher temperatures, 50 K - 80 K (Pontoppidan et al., 2008). As was noted above,

several of our sources do not have an apolar CO_2 component, and all but one of those has a crystalline CO_2 component. If distillation were the primary method for crystallization, we would expect many low mass YSOs to have a crystalline component. We propose a scenario in which both distillation and segregation are responsible for crystallization. If we start near the YSO, we have a region that is too warm for ice. As we move farther away from the YSO, we might expect a warm polar and annealed ices, in which case segregation would be responsible for the crystallization. Increasing the radial distance would decrease the temperature, but we could still have warm polar ice and also warm apolar ice. CO would sublimate from the grain and distillation would be responsible for any crystalline ice. Finally, farthest from the YSO would be the cold polar and apolar ices.

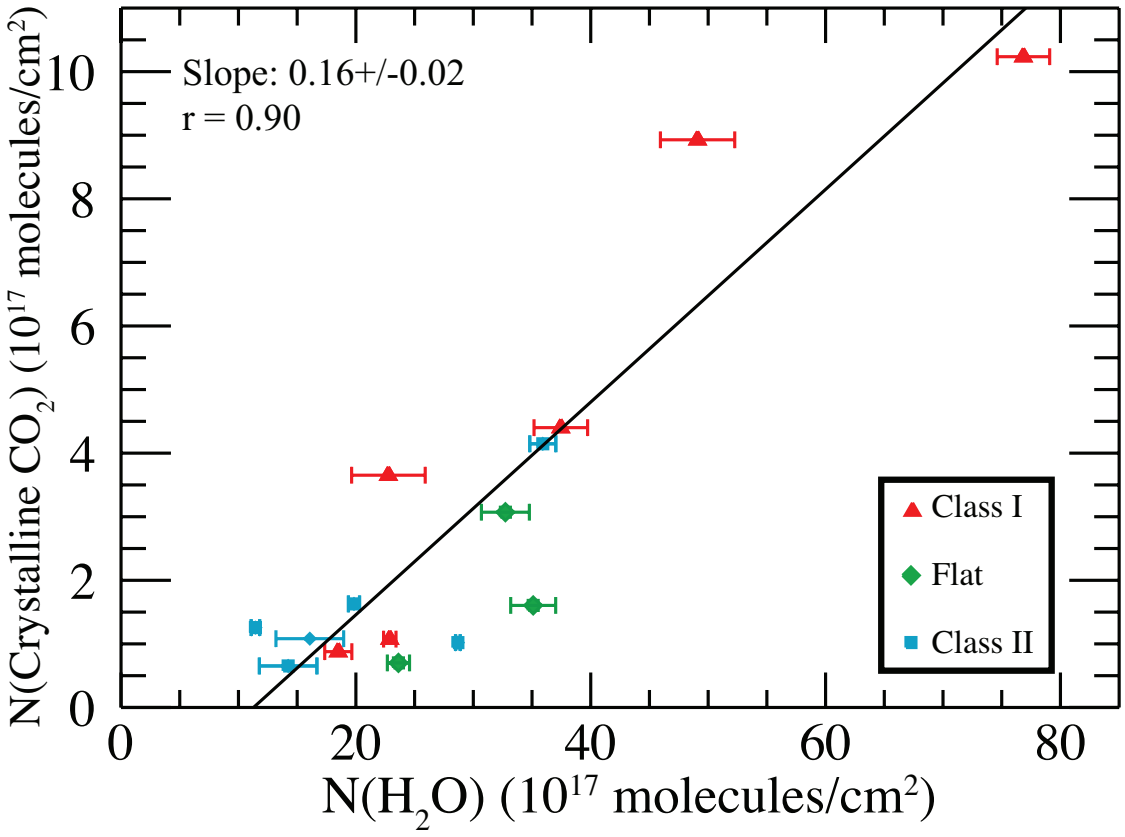

Figure 4.14 The column density of the crystalline component of the CO_2 ice feature versus the column density of water is shown by source. Red triangles are sources with Class I SEDs, green squares have Flat SEDs, and the blue diamonds are YSOs with Class II SEDs. Note there is a tight correlation (r = 0.90) with a slope of 0.16±0.02.

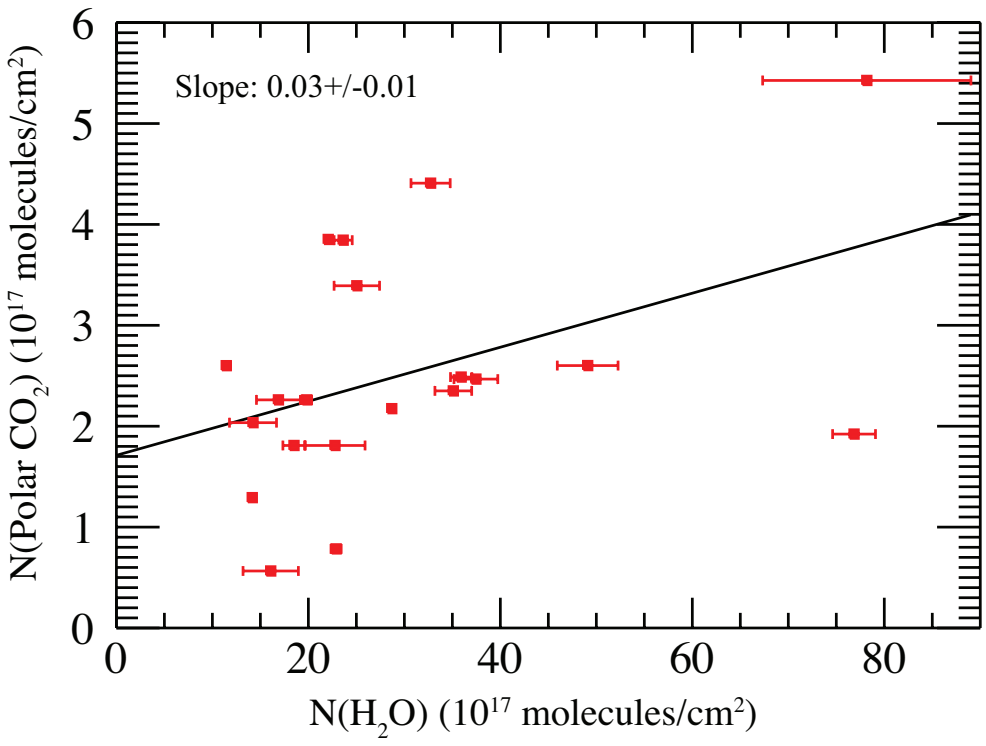

Figure 4.15 The column density of the polar component of the CO_2 ice feature versus the column density of water is shown by source. As can be seen from the large scatter, there is little correlation between the column densities and a low abundance of CO_2. We found a slope of 0.03±0.01, and a Pearson correlation coefficient of 0.42.

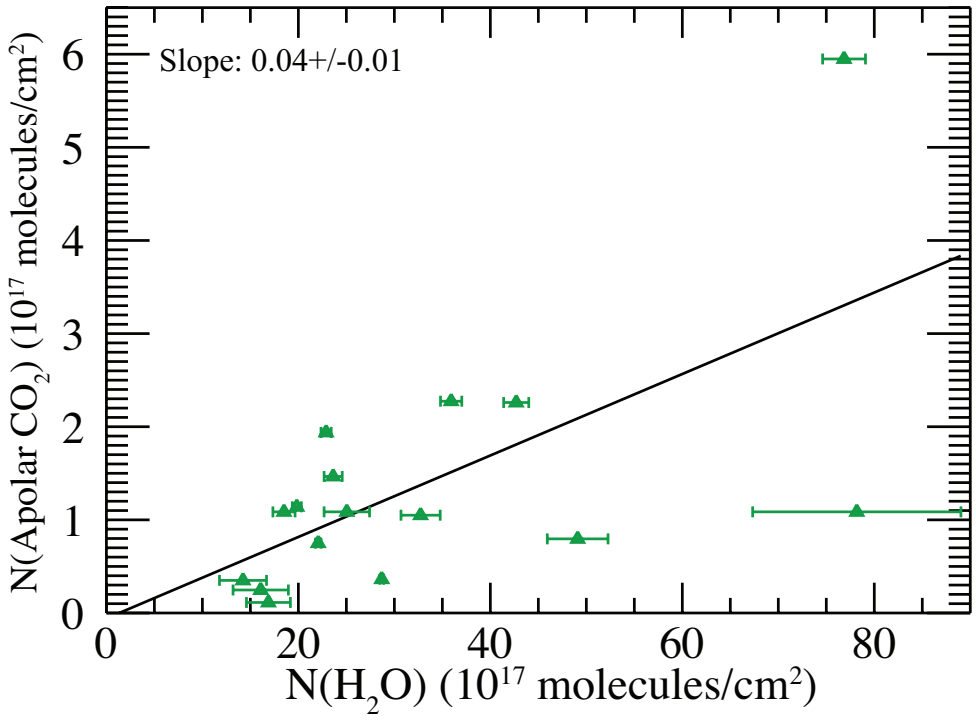

Figure 4.16 The column density of the apolar component of the CO_2 ice feature versus the column density of water is shown by source. Despite the large scatter, there is a weak correlation, r = 0.63. However, without the two outliers with $N(H_2O) > 60$, the correlation is only r = 0.48. We found a steeper slope than that of the polar component, but lower than that of the crystalline component: 0.04 ± 0.01.

In this section we have investigated the correlation between CO_2 ice and H_2O, SED class, visual extinction, and nearby intermediate-mass young stars. The locations of YSOs with warm or annealed ices and those with cold ices vary throughout the Rho Oph region, and do not depend on proximity to intermediate mass YSOs. In addition, the abundance of CO_2 does not increase with radial distance to dense cores, nor does it correlate with visual extinction. The average abundance for this work is similar to that of Zasowski et al. (2009), but less that that reported by Oberg et al. (2011). The column density of CO_2 correlates with

H_2O which suggests that the polar component of CO_2 may form in tandem with H_2O, as it does in quiescent regions. However, there are a significant number of sources in Rho Oph that show a characteristic double-peaked structure in the CO_2 ice consistent with heating, which creates crystalline ice. The low column density of the apolar component supports the method of distillation, or CO sublimation from the apolar CO:CO_2 layer leaving behind crystallized CO_2 rather than CO_2 being segregrated from H_2O in the polar layer. In addition, if sources with Class I SEDs are more efficient at producing crystalline CO_2 ice through distillation, the apolar ice would reside close to the young star. We also found that a few YSOs with Flat or Class II SEDs show the largest abundances of total CO_2. We believe these larger abundances of CO_2 are the result of the activation of an additional formation route that is unrelated to the process of crystallization.

4.2. INTERCLOUD CORRELATIONS

With the data from Zasowski et al. (2009), Cook et al. (2011), and others, we are able to make a cloud-to-cloud comparison. Previously published column densities for low mass YSOs toward each star forming region are presented in the corresponding section on that star forming region and those for Rho Oph are in Table 4.4. A summary of the average CO_2 abundance for each region and the linear correlation information is presented in Table 4.5. While most of the Taurus column densities (see Table 4.6) are from Zasowski et al. (2009), several of the YSOs in Taurus have column densities measured by multiple authors (see Nummelin et al. (2001), Bergin et al. (2005), Pontoppidan et al. (2008), and Cook et al. (2011)). In cases with multiple published values for a single source, the weighted mean was used to determine the column density. For the four YSOs with multiple measurements, the column densities of H_2O found by Zasowski et al. (2009) are larger. The percent differences between the Zasowski et al. (2009) sources and the previously published data for the same source range from 20-73%. Note that we scaled the values of Zasowski et al. (2009) by 1.5/1.1 to account for the different band strength used for the CO_2 column density. In addition, eleven of the column densities for CO_2 from Cook et al. (2011) were previously published, and all are greater than previous values, with percent differences ranging from 13-45%. This

study contains three YSOs with column densities published by Cook et al. (2011), and two of the three have lower CO_2 column densities than those reported by Cook et al. (2011). The only YSO for which Cook et al. (2011) report a lower CO_2 column density is ISO-Oph 125. H_2O and CO_2 column densities from this study for which previous data have been published do not show a systematic difference, some have larger column densities and some have lower column densities. Our percent differences from previously published values range from 4-75% for H_2O, and 0.4-48% for CO_2. This study and that of Zasowski et al. (2009) used the 6 μm feature to determine the H_2O column density, while the H_2O column densities used by Cook et al. (2011) and Pontoppidan et al. (2008) were found with the 3 μm feature.

Using the compiled data, we found that H_2O and CO_2 have a strong correlation in Taurus, with a slope of 0.11 ± 0.03 and a Pearson correlation coefficient of 0.67 (Figure 4.17). This slope is not as steep as our slope for YSOs in Rho Oph, shown as the 0.15 ± 0.04 line, but more comparable to Rho Oph than to low-mass YSOs in general. The weighted average of reported CO_2 abundances for Taurus, 0.150 ± 0.003, is lower than that for Rho Oph (0.174 ± 0.002), but still comparable. Given the higher H_2O column density toward four previously-published sources, the use of the 6 μm feature by Zasowski et al. (2009) may systematically overestimate the column density of H_2O at 6 μm toward some sources. They are not the first authors to suggest this possibilty (see Gibb et al. (2004) and Pontoppidan et al. (2008)). If that is, in fact, the case, then the abundances reported by Zasowski et al. (2009) toward Taurus and the abundances reported toward Rho Oph reported here could be lower than if the 3 μm H_2O ice feature was used. Oberg et al. (2011) also note the CO_2 abundance is low toward Taurus, but cite that as unusual, rather than the norm. While the data available for Taurus and Rho Oph provide us with the best statistics because of the number of sources, comparing these abundances toward other molecular clouds is necessary to determine if the large scatter and low abundance in Taurus and Rho Oph are typical or atypical.

Table 4.4. Published column densities toward low-mass YSOs in Rho Ophiuchi.

Source	N(H_2O) (10^{17} molecules/cm^2)	N(CO_2) (10^{17} molecules/cm^2)	Abundance	Reference
ISO-Oph 29	15.30±3.00	3.28±0.06	21.4±4.2%	1
ISO-Oph 65	22.10±3.00	4.34±0.05	19.6±2.7%	1
ISO-Oph 112	—	2.69±0.09	—	1
WL 20	—	5.02±0.06	—	1
ISO-Oph 124	36.50±5.00	4.05±0.08	11.1±1.5%	1
ISO-Oph 125	35.5±5	4.91±0.51	13.8±2.4%	1,2
ISO-Oph 132	19.50±2.00	4.49±0.05	23.0±2.4%	1
ISO-Oph 134	41.70±6.00	9.33±0.08	22.4±3.2%	1
ISO-Oph 137	45±5	13.5±0.2	30.0±3.4%	1,2
ISO-Oph 137	45.00±5.00	10.54±0.06	23.4±2.6%	1
ISO-Oph 141	31.50±4.00	12.26±0.12	38.9±5.0%	1
ISO-Oph 143	34.00±4.00	6.92±0.08	20.4±2.4%	1
ISO-Oph 144	17.90±2.60	4.87±0.09	27.2±4.0%	1
ISO-Oph 145	12.80±2.00	2.35±0.12	18.4±3.0%	1
ISO-Oph 147	17.00±2.00	5.86±0.11	34.5±4.1%	1
ISO-Oph 167	22.10±3.00	9.32±0.07	42.2±5.7%	1
WLY2-63	20.4±3	7.82±0.4	38.3±6.0%	1,2
IRS 63	20.40±3.00	6.84±0.05	33.5±4.9%	1

[1]Pontoppidan et al. (2008)

[2]Cook et al. (2011)

Table 4.5. Summary of abundances and correlations.

Region	Linear Correlation	Average Abundance
Rho Oph	0.15±0.04, r = 0.62	18.6±0.4% (this work) 17.3±0.2% (all)
Taurus YSOs	0.11±0.03, r = 0.67	15.0±0.3%
Taurus background objects	0.18±0.02, r = 0.96	19.0±1%
Serpens YSOs	0.29±0.05, r = 0.94	36±%
Corona Australis	0.19±0.05, r = 0.90	30±1%
Perseus	0.30±0.02, r = 0.91	19.8±0.9%
Background Objects toward Serpens and Isolated Cores		32-41% (Oberg et al., 2011)
High Mass YSOs		12-22% (Oberg et al., 2011)

Table 4.6. Column densities toward low-mass YSOs in Taurus.

Source	N(H_2O) (10^{17} molecules/cm^2)	N(CO_2) (10^{17} molecules/cm^2)	Abundance	Reference
DF Tau	—	9.22±0.65	—	1,2
DG Tau B	26.3±2.6	7.49±0.74	28.5±4.0%	1,2
	26.30±2.60	5.40±0.06	20.5±2.0%	1
	56.5±6	5.78±1.02	10.2±2.1%	3
Elias 18	14±1.4	6.65±0.47	47.5±5.8%	1,2
	14±1.4	5.2±0.4	37.1±4.7%	4
HL Tau	13.57±1.357	1.9± 0.1	14.0±1.6%	5
	19.1±2	1.90±0.87	10.0±4.7%	3
IC2087 IR	21.3±2	5.66±0.86	26.6±4.7%	3
IRAS 04016+2610	59.1±2	14.02±1.03	23.7±1.9%	3
IRAS 04108+2803A	29±3	3.76±0.84	13.0±3.2%	3
IRAS 04108+2803B	44.4±2	6.72±0.83	15.1±2.0%	3
IRAS 04154+2823	8.75±0.8	4.47±1.27	51.1±15.2%	1,2
	10.7±2	2.82±1.00	26.3±10.5%	3
IRAS 04169+2702	43.3±2	5.96±0.84	13.8±2.0%	3
IRAS 04181+2654A	25±2	7.67±0.24	30.7±2.6%	1,2
	36.3±2	5.64±0.80	15.5±2.4%	3
IRAS 04181+2654B	41.8±4	8.89±1.50	21.3±4.1%	3
IRAS 04239+2436	44.4±2	7.63±1.08	17.2±2.6%	3
IRAS 04295+2251	28.2±3	3.61±0.80	12.8±3.2%	3
IRAS 04361+2547	73.8±3	4.93±0.98	6.7±1.4%	3
IRAS 04365+2535	53.1±2	11.01±0.70	20.7±1.5%	3
IRAS 04381+2540	79.2±2	12.74±1.19	16.1±1.6%	3
ITG 25B	16±1.6	4.63±0.57	28.9±4.6%	1,2
L1489	47.00± 2.80	16.20±0.09	34.5±2.1%	1
	47±2.8	19.3±1.7	41.1±4.4%	1,2
L1551 IRS 5	—	13.7±0.61	—	1,2
	109±2	11.89±1.92	10.9±1.8%	3
MHO-3	—	3.57±0.33	—	1,2
TMC-1A	—	17.52±0.62	—	1,2
V410 X-ray 2	—	6.85±0.24	—	1,2

[1]Pontoppidan et al. (2008)

[2]Cook et al. (2011)

[3]Zasowski et al. (2009)

[4]Nummelin et al. (2001)

[5]Bergin et al. (2005)

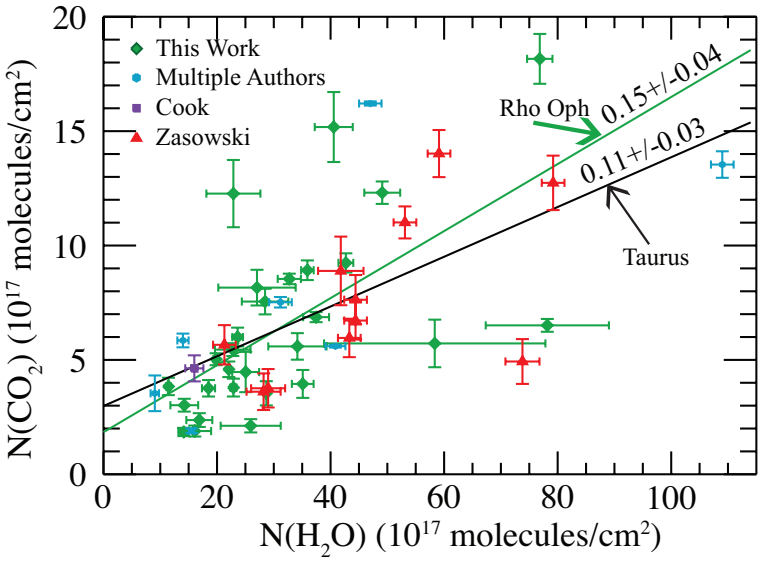

Figure 4.17 The column density of CO_2, N(CO_2) is plotted versus the column density of H_2O, N(H_2O) for YSOs in Taurus compiled from the literature. Zasowski et al. (2009) data are the red triangles, Cook et al. (2011) data are the purple squares. A weighted mean was taken for sources with multiple published values (see Nummelin et al. (2001), Bergin et al. (2005), Pontoppidan et al. (2008), Zasowski et al. (2009), and Cook et al. (2011)). Rho Oph YSOs from this study are also included (green diamonds).

4.2.1. Perseus. We will first look at YSOs in Perseus, a nearby low-mass star forming region (Jørgensen et al., 2006). The distance is uncertain. DeZeeuw et al. (1999) reported a distance of 320 pc using parallax measurements, while Cernis (1990) suggested a distance of 200-250 pc using extinction studies. The correlation between the column densities of CO_2 and H_2O (Figure 4.18) was determined using the data of Pontoppidan et al. (2008) (Table 4.7). This relationship shows a tighter correlation than either Taurus or Rho Oph, with a correlation coefficient of r = 0.98. The slope of the correlation line is 0.30±0.02, steeper than the slopes we found for Rho Oph and Taurus. The average abundance is 19.8%±0.9%, which is lower than the average value reported by Oberg et al. (2011) of ∼29% toward low mass YSOs, but consistent with the average abundances we found for Rho Oph and Taurus. In addition, all of the sources contain a larger polar CO_2 component with respect to total CO_2 than YSOs in Rho Oph, ranging from 52% to 82%. A high polar component suggests the H_2O and polar CO_2 formed together, with reaction 3.3 (Garrod and Pauly, 2011). We emphasize that these

results only include eight YSOs. Jørgensen et al. (2006) found over 350 YSOs toward Perseus. It is necessary to complete a study with more YSOs to obtain sufficient statistics and confirm the above values.

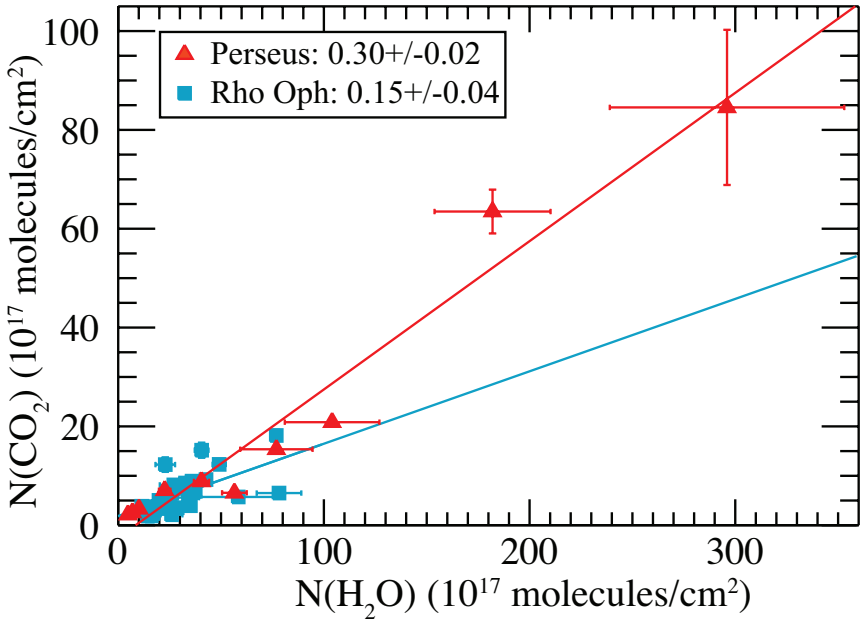

Figure 4.18 The column density of CO_2, $N(CO_2)$ is plotted versus the column density of H_2O, $N(H_2O)$ for Perseus (red triangles). Rho Oph YSOs from this study are also included (blue squares). There is noticably less scatter than for either Taurus or Rho Oph, and the slope of the correlation line is 0.30 ± 0.02. Each of the sources consists of a polar component of at least 50% of the total CO_2.

Table 4.7. Column densities toward low-mass YSOs in Perseus.

Source	N(H_2O) (10^{17} molecules/cm^2)	N(CO_2) (10^{17} molecules/cm^2)	Abundance	Reference
L1448 IRS 1	4.70±1.60	2.14±0.01	45.5±15.5%	1
L1448 NA	—	40.92± 0.35	—	1
L1455 SMM 1	182.00±28.20	63.48±4.43	34.9±5.9%	1
RNO 15	6.90±0.60	2.57±0.05	37.2±3.3%	1
IRAS 03254	40.50±3.70	8.86±0.10	21.9±2.0%	1
IRAS 03271	76.90±17.60	15.37±0.09	20.0±4.6%	1
B1-a	104.00±23.00	20.85±0.14	20.0±4.4%	1
B1-c	296.00±57.00	84.55±15.70	28.6±7.6%	1
IRAS 03439	10.10±0.90	3.32±0.06	32.9±3.0%	1
IRAS 03445	22.60±2.80	7.07±0.09	31.3±3.9%	1

[1]Pontoppidan et al. (2008)

4.2.2. Corona Australis. Corona Australis, or CrA, is another nearby star forming region that is ∼130 pc away (Marraco and Rydgren, 1981). Like Rho Oph, the most massive stars in the cluster have spectral types of A and B (Peterson et al., 2011). The correlation of the column density of CO_2 with the column density of H_2O for CrA using published data was determined using the column densities for low mass YSOs in CrA presented in Table 4.8 and is 0.19±0.05, with a correlation coefficient of r = 0.90 (see Figure 4.19). Again, Rho Oph is plotted for comparison as the squares. However, unlike Rho Oph, Taurus, and Perseus, the average abundance is 30%±1%, but does agree with the average abundance toward all low mass YSOs reported by Oberg et al. (2011). The correlation coefficient is similar to that of Perseus, 0.90, but again, there are only five YSOs to consider. Also like Perseus, the column density of polar component reported by Pontoppidan et al. (2008) and Cook et al. (2011) toward these sources ranges from 49% to 83% of the total CO_2 column density. Again, we note that further observations of this region are necessary in order to substantiate the results presented here. These studies may be more difficult than those toward Perseus, as it is estimated that CrA has only about 40 YSOs (Peterson et al., 2011).

Table 4.8. Column densities toward low- and intermediate-mass YSOs in Corona Australis.

Source	$N(H_2O)$ (10^{17} molecules/cm^2)	$N(CO_2)$ (10^{17} molecules/cm^2)	Abundance	Reference
R CrA IRS 5	37.60±2.80	14.28± 0.13	38.0±2.8%	1
	37.6±2.8	18.26±0.22	48.6±3.7%	1,2
Rcra IRS 7A	109.00±19.20	19.64±0.12	18.0±3.2%	1
R CrA IRS 7a	109±19	23.5±0.23	21.6±3.8%	1,2
Rcra IRS 7B	110.00±19.70	26.74±0.22	24.3±4.4%	1
IRAS 32	52.60±18.80	18.70±0.21	35.6±12.7%	1
R CrA	3±0.3	0.9±0.1	30.0±4.5%	3,4

[1]Pontoppidan et al. (2008)

[2]Cook et al. (2011)

[3]Nummelin et al. (2001)

[4]Tanaka et al. (1994)

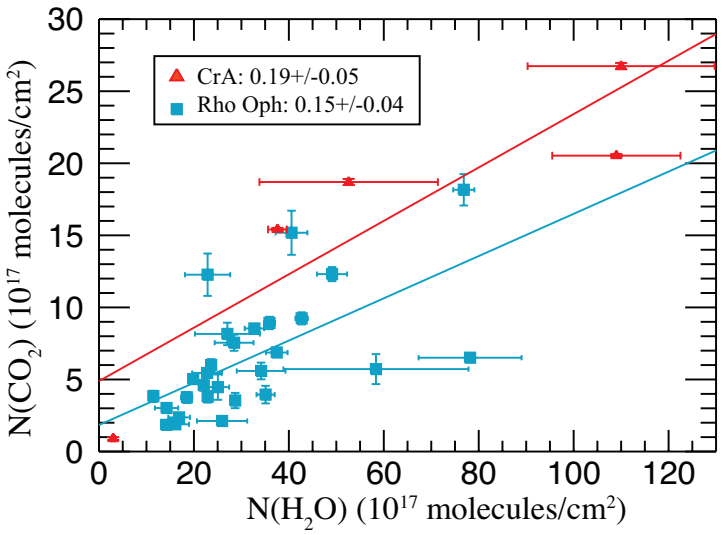

Figure 4.19 The column density of CO_2, $N(CO_2)$ is plotted versus the column density of H_2O, $N(H_2O)$ for Corona Australis (red triangles). Rho Oph YSOs from this study are also included (blue squares). The slope of the correlation line is 0.19±0.05, and the correlation coefficient indicates a stronger correlation than that of Taurus or Rho Oph. However, note that data are available for only five YSOs toward this region. This average abundance is greater than the result we present toward Rho Oph but consistent with the result presented toward low mass YSOs by Oberg et al. (2011).

4.2.3. Serpens. Finally, we will compare the abundance and scatter in Rho Oph with the Serpens star forming region. Straizys et al. (1996) estimate Serpens to be 259 pc away using extinction estimates, but Dzib et al. (2010) report a much farther distance of 415±25 pc using parallax measurements from the binary system EC 95. Serpens is particularly interesting because it was the first report of a background star with a larger abundance of CO_2, 33% toward CK 2 (Knez et al., 2005). There is a tight correlation between CO_2 and H_2O (Figure 4.20), r = 0.94, with a slope of 0.29±0.05, even though there are only seven sources for which data is available (see Table 4.9). YSOs toward Serpens have the highest average abundance of each of the previously described star forming regions, 35%±2%. In addition, these sources also have a larger polar CO_2 component with respect to total CO_2 than many of the Rho Oph sources, ranging from 61% to 77%, but a smaller polar component than that found toward background objects, 85% (Whittet et al., 2009). The high abundance toward background objects and YSOs in Serpens indicate this regions is unique and produces either more CO_2 or less H_2O than other regions.

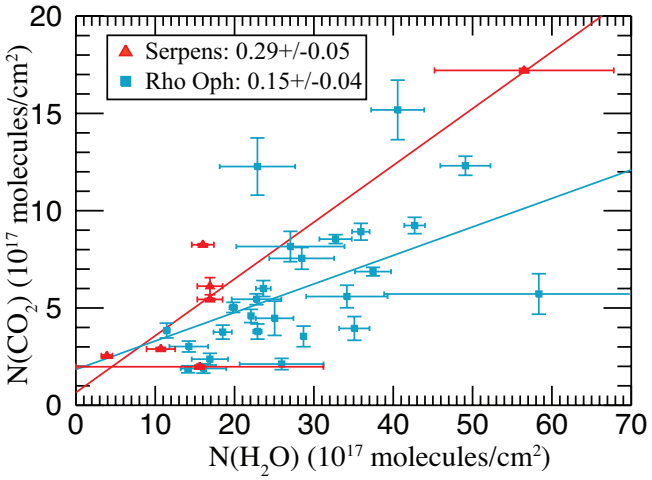

Figure 4.20 The column density of CO_2, N(CO_2) is plotted versus the column density of H_2O, N(H_2O) for Serpens (red triangles). Rho Oph YSOs from this study are also included (blue squares). The slope of the correlation line is 0.29±0.05, and the Pearson correlation coefficient is 0.94, indicating a strong correlation.

Table 4.9. Column densities toward low mass YSOs in Serpens.

Source	N(H_2O) (10^{17} molecules/cm^2)	N(CO_2) (10^{17} molecules/cm^2)	Abundance	Reference
CK 1	16.9±1.6	6.12±0.44	36.2±4.3%	1,2
EC 74	10.70±1.8	2.89±0.08	27.0±4.6%	2
EC 82	3.90±0.70	2.54±0.04	65.1±11.7%	2
SVS 4-5	56.50±11.40	17.21±0.10	30.5±6.1%	2
EC 90	16.90±1.60	5.44±0.05	32.2±3.1%	2
SVS 4-10	16.00±1.40	8.25±0.05	51.6±4.5%	2

[1]Cook et al. (2011)

[2]Pontoppidan et al. (2008)

Lastly, a comparison with pristine, unprocessed material provides a baseline for the abundance of CO_2. As such, we have compared CO_2 abundance values, and found less scatter than there is toward Rho Oph. CO_2 abundance values still range from 12-45%. If we consider the correlation between the column densities of CO_2 and H_2O, Figure 4.21, we find a slope of 0.45±0.05, and a tight correlation, r = 0.92. The average abundance, however, is 22%±1%. This average abundance is higher than that for Taurus and Rho Oph, consistent with that of Perseus, and lower than that of CrA or Serpens. This average abundance is also lower than that reported by Oberg et al. (2011), but they cite the Taurus data as being unusually low and do not include it in their analysis. The column density values for background objects are presented in Table 4.10.

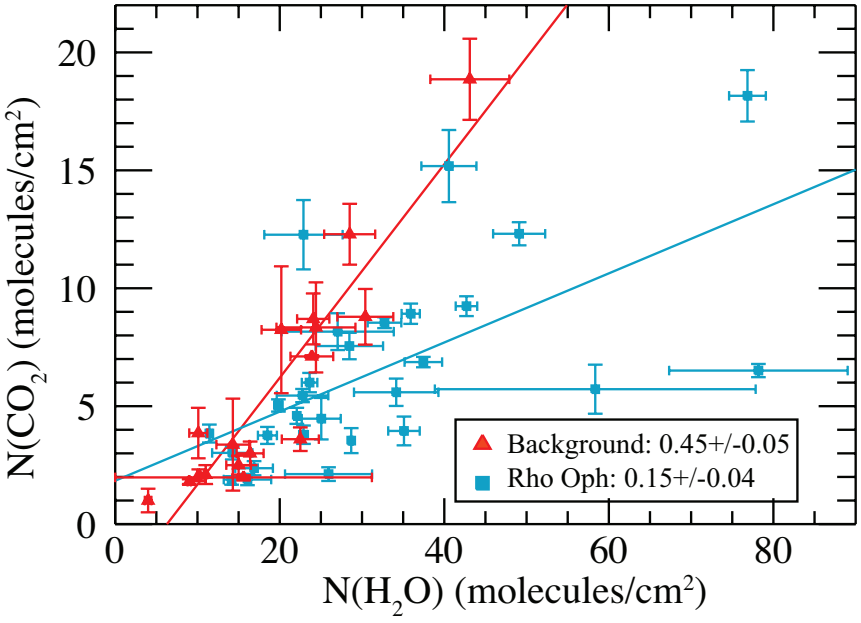

Figure 4.21 The column density of CO_2, N(CO_2) is plotted versus the column density of H_2O, N(H_2O) for background objects (red triangles). Rho Oph YSOs from this study are also included (blue squares). There is is a strong correlation, and the abundance of CO_2 with respect to H_2O is higher than that toward any mass YSOs, 45%±5%.

Table 4.10. Column densities toward background objects.

Source	N(H_2O) (10^{17} molecules/cm^2)	N(CO_2) (10^{17} molecules/cm^2)	Abundance	Region	Reference
120145986508586	24.4±4.8	8.34±1.91	34.2±10.3%	DC 297.7-2.8	1
181704291802540	14.3±2	3.37±1.95	23.6±14.0%	L328	1
181709570814136	28.5±3.1	12.29±1.29	43.1±6.5%	L429-C	1
181726900438406	43.1±4.8	18.86±1.72	43.8±6.3%	L 483	1
19201622+1136292	10.1±1.1	3.86±1.07	38.2±11.4%	CB 188	1
21240517+4959100	20.19±2.4	8.24±2.69	40.8±14.2%	L1014	1
18300061+0115201	30.4±3.4	8.79±1.18	28.9±5.1%	Serpens	1
CK 2	24.07±1.96	8.70±1.08	36.2±5.4%	Serpens	2,3
CK 4	15.60±15.60	1.98±0.09	12.7±12.7%	Serpens	2
04393886+2611266	23.9±2.6	7.11±0.05	29.7±3.2%	Taurus	1
042630.7+243637	16.4±1.64	3±0.5	18.3±3.6%	Taurus	3
043213.2+242910	22.5±2.25	3.6± 0.5	16.0±2.7%	Taurus	3
043728.2+261024	4±0.4	1±0.5	25.0±12.7%	Taurus	3
043926.9+255259	15±1.5	2.5±0.4	16.7±3.1%	Taurus	3
Elias 13	11±0.19	2.1pm40.4	19.1±3.7%	Taurus	4
Elias 16	10.16±0.17	2.07±0.25	20.4±2.4%	Taurus	3,4,5
Elias 3	9±0.2	1.8±0.1	20.0±1.2%	Taurus	5

[1]Boogert et al. (2011)

[2]Pontoppidan et al. (2008)

[3]Whittet et al. (2009)

[4]Nummelin et al. (2001)

[5]Bergin et al. (2005)

In summary, we have compared the abundance of CO_2 with respect to H_2O and the degree to which the column densities of H_2O and CO_2 are linearly related between Rho Oph, four other star-forming regions, and background objects. Using column densities published from several studies, Taurus has the lowest abundance and more scatter in the data than the studies for other regions. This may be due, in part, systematic differences in the column densities reported by Zasowski et al. (2009) and Cook et al. (2011) and previously published values. Zasowski et al. (2009) noted that their H_2O column densities may represent an upper limit, as the composition of the 6 μm feature is not fully understood (Gibb et al. (2004) and Pontoppidan et al. (2008)). Since most of the Taurus data are from Zasowski et al. (2009), this would lower the average abundance toward Taurus. The lower average abundance toward Taurus and larger scatter than that toward all low mass YSOs are similar to the lower abundance and large scatter we found for Rho Oph. Perseus shows an average abundance similar to Rho Oph and Taurus, but a tighter correlation between the column densities of CO_2 and H_2O with a steeper

slope. Corona Australis has higher average abundance than Rho Oph, Taurus, and Perseus, and a tight correlation between the column densities of CO_2 and H_2O with a slope similar to that of Rho Oph. Finally Serpens has the highest average abundance and a strong correlation between the column densities of CO_2 and H_2O with the steepest sloep of the five star forming regions. YSOs toward Rho Oph, on average, have a lower abundance of the polar CO_2 component than Serpens, CrA, and Perseus. This may be an explanation for the scatter seen in Rho Oph. A possibility for the tight correlation in Serpens, CrA, and Perseus may simply be a lack of statistics. Further study of these regions is necessary to confirm the tight correlation and abundance.

5. THE GV TAU BINARY SYSTEM

5.1. INTRODUCTION

GV Tau (Haro 6-10, IRAS 04263+2426) is an unusual young T Tauri binary system partly embedded in the L1524 molecular cloud. It is one of a small number of young binaries for which the primary (GV Tau S) is optically visible and the infrared companion (IRC, GV Tau N), located 1.″2 to the north, is strongly extincted. The spectral energy distribution (SED) of the primary is flat or rising in the 1–100 μm range, suggesting that it is a class I object (Koresko et al., 1999). Leinert and Haas (1989) found that GV Tau N was generally brighter than the primary at wavelengths longer than $\sim$4 μm. It has also been found that the system is variable, particularly in the near infrared, and on timescales as short as a month (Leinert et al., 2001; Koresko et al., 1999). Leinert et al. (2001) found that the primary became redder as it became fainter at K. Also, the depth of the 3 μm ice band was found to vary with time, and their results suggested that an increase in optical depth corresponded to a decrease in K brightness. Both of these measurements are consistent with the dominant mechanism of the variability of GV Tau S being due to inhomogeneities in circumstellar material that result in changes in extinction. The behavior for GV Tau N is more complex and suggests the possibility of variable accretion mechanisms (Leinert et al., 2001).

The system shows a parsec-scale Herbig-Haro flow with a well-defined axis, as well as other smaller flows (Devine et al., 1999). One of those smaller flows was associated with GV Tau N, however, it has been proposed by Wilking et al. (2012) that this outflow comes from a yet unobserved companion to GV Tau S. If confirmed, the system would then be comprised of three objects. Near-infrared emission images suggest the presence of a flattened circumbinary envelope with a semi-major axis of $\sim$1000–1500 AU seen nearly edge-on as the source of the observed polarization and part of the extinction toward both objects (Ménard et

al., 1993). We note that their observations do not exclude the additional presence of circumstellar disks around one or both objects.

We report high-resolution near-infrared detections of CO, HCN, and C_2H_2 toward GV Tau N. For the primary, CO was detected in absorption, but HCN and C_2H_2 were not. As we previously discussed our observations and data reduction in §2, we begin with the results of analysis for HCN, C_2H_2, and CO, along with upper limits for CH_4 in §5.2. We conclude with a discussion of these results in §5.3.

5.2. MOLECULAR ABSORPTIONS TOWARD GV TAU

5.2.1. CO Gas Spectra. **5.2.1.1. GV Tau N.** The infrared companion, GV Tau N, was observed at M band in March 2003, but was not placed in the slit during the K-band observations. The IRC was resolved and ^{13}CO was detected, though C^{18}O was not. We estimate that the ^{12}CO column density is $\sim$11.8x10^{18} cm^{-2}, assuming that the ^{12}CO/^{13}CO ratio toward the two objects is the same. This assumption seems reasonable, given that the ^{12}CO lines toward GV Tau N are about half as strong as those toward GV Tau S, and in order to bring N(^{12}CO) for GV Tau N in agreement with the primary, the ^{12}CO/^{13}CO ratio would have to be a factor of two higher. Future observations of the overtone CO lines toward the IRC are planned to directly measure ^{12}CO.

5.2.1.2. GV Tau S. For GV Tau S, the fundamental ro-vibrational lines of ^{12}CO, ^{13}CO, and C^{18}O near 4.67 μm and the overtone bands near 2.3 μm were observed in absorption in March and August 2003, respectively (Figure 2.14). Absorption line studies have the advantage of measuring physical conditions in a pencil-beam column of gas along the line of sight to the emitting source, usually the star and inner accretion disk. This allows us to sample a long path length through the edge-on circumbinary envelope and circumstellar disk. The rotational temperatures and column densities of the different bands and isotopes of CO were derived using a population analysis and are presented in Figure 5.1 and Table 5.1. The overall rotational temperature found for CO toward GV Tau S is $\sim$220 K. This is also similar to the warm ($\sim$100 K) temperatures we find toward other flared disk systems (Rettig et al., 2006) and implies that the gas is located in the

inner, potentially planet forming (∼10 AU or so) region of the circumstellar disk rather than in the more distant interstellar or circumbinary material. The column density of ^{12}CO was found to be (5.9 ± 1.2) x 10^{18} cm^{-2} based on an analysis of the overtone lines, which are optically thin. The fundamental lines of CO are optically thick and require a curve of growth analysis.

We found ^{12}CO/^{13}CO to be 54 ± 15, consistent with that measured toward Orion A (Langer and Penzias, 1990, 67 ± 3) and that found toward the young star HL Tau (Brittain et al., 2005, 76 ± 9). The ^{12}CO/C^{18}O ratio is 420 ± 170, somewhat lower than toward Orion (Langer and Penzias, 1990, ∼660), HL Tau (Brittain et al., 2005, 800 ± 200), and the canonical interstellar value of 560 ± 25 found by Wilson and Rood (1994). We would expect the isotopic abundance ratios to reflect the isotopic composition of the dense cloud unless influenced by a mechanism such as selective dissociation (Lyons and Young, 2005), which may occur since the isotopomers are not self-shielded as effectively as ^{12}CO. This effect does not seem to be evident toward GV Tau.

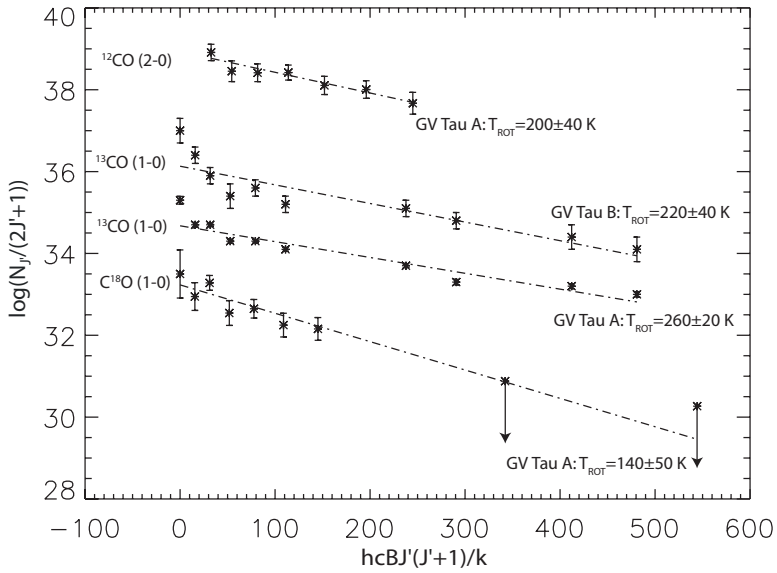

Figure 5.1 Population diagram of the ^{12}CO (2-0), ^{13}CO (1-0) and C^{18}O (1-0) lines.

Table 5.1. Column densities and rotational temperatures for molecules.

Molecule	Column Density (10^{16} cm^{-2})	T_{rot} (K)	Abundance Relative to ^{12}CO (%)
GV Tau N			
^{12}CO	$\sim$1180[a]	200±40	—
^{13}CO	11	260±20	0.93
C^{18}O	1.4±0.5	140±50	0.12
HCN	3.7±0.3	$115^{+11}/_{-10}$	0.31
C_2H_2	$7.3^{+0.1}/_{-0.2}$	$170^{+19}/_{-16}$	0.62
CH_4	<2.2	—	<0.19
GV Tau S			
^{12}CO	590±120	—	—
^{13}CO	5.5	220±40	0.93[a]
HCN	<0.48	—	<0.08

[a]Assuming ^{12}CO/^{13}CO ratio is the same as for GV Tau N

5.2.2. HCN Gas. 5.2.2.1. GV Tau N. Rather strong absorption lines due to the HCN (100-000) band near 3.0 μm were detected toward GV Tau N. Spectral extracts are shown in Figure 2.15. The geocentric Doppler shifted positions (+49 km/s) of the HCN absorption lines and the specific identifications are indicated by solid ticks. We performed a rotational analysis on absorption features that were at transmittance >80%, were not blended with C_2H_2 transitions (also indicated in Figure 2.15), and were clear of contamination from stellar absorption features as determined from a comparison to the similar spectral type high-resolution Arcturus spectrum of Hinkle et al. (1995). There were a total of 10 lines that satisfied these criteria, ranging from J=0-7.

Einstein A's and line positions were taken from the ab initio line list calculated by Harris et al. (2002), which expanded on previous line lists and improved accuracy by using the most accurate potential energy surface and dipole moment surface information available. The population diagram is shown in Figure 5.2. The Doppler shifted positions and equivalent widths used are given in Table 5.2. We note that the lines in our analysis are optically thin for most reasonable values of the intrinsic line widths (b). For example, the R6 line is optically thin ($\tau < 1$) for all b > 1.7 km/s. For R1, $\tau > 1$ is achieved only for b < 0.9 km/s. Brittain et al. (2005) found b = 1.3±0.1 km/s for CO toward HL Tau. Lahuis et al. (2006) found that no good fit can be made to the C_2H_2 and CO profiles for b <

2 km/s. Boogert et al. (2002) find that 0.8<b<1.5 km/s toward L1489 to explain the CO observations. If we make a reasonable assumption that b>1 km/s, then our absorptions are optically thin. This is also supported by the linearity of the population diagram. From this, we derive a rotational temperature of 115^{+11}_{-10} K and a total HCN column density of (3.7±0.3) x 10^{16} cm^{-2} toward GV Tau N. Comparing this to the CO column density (section 3.1) provides an HCN/CO ∼ 0.31%

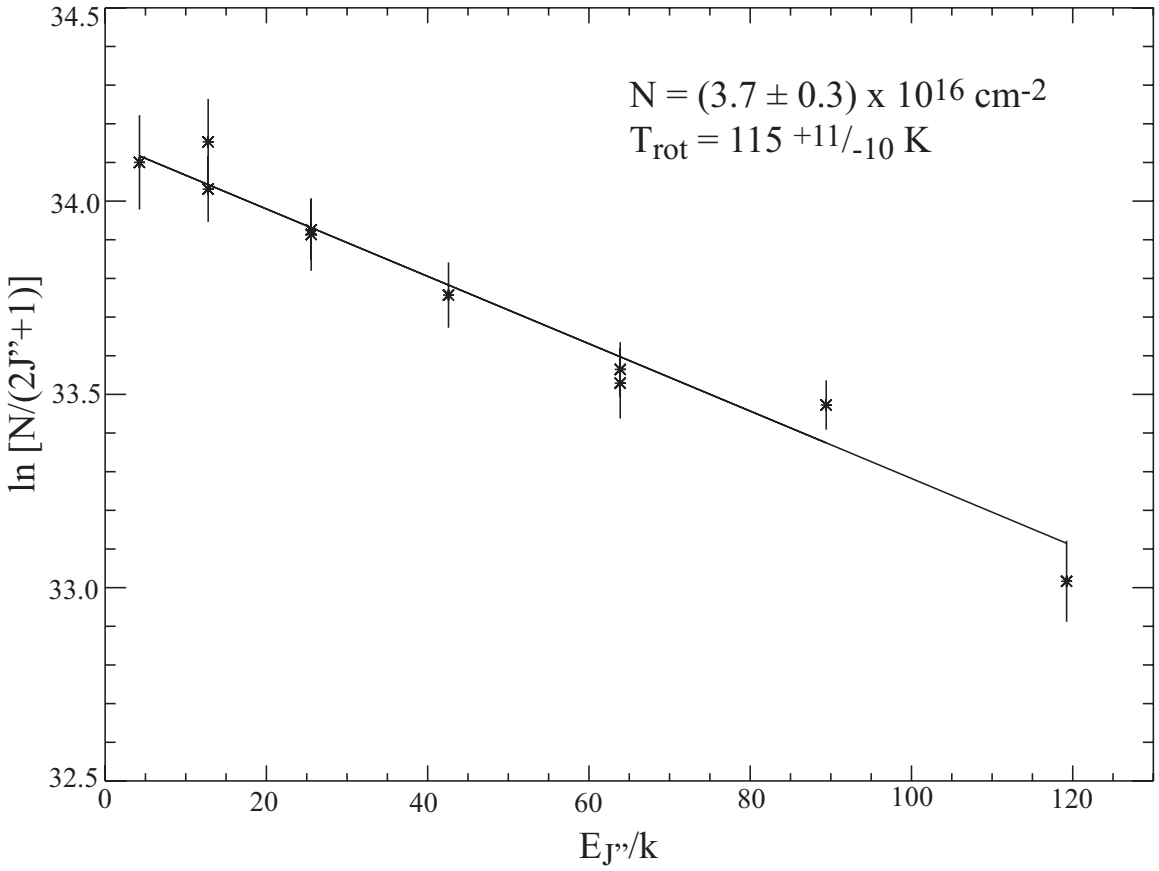

Figure 5.2 Population diagram for HCN absorption toward GV Tau N.

Table 5.2. HCN line positions and equivalent widths.

Line ID	ν_{rest} (cm^{-1})	ν_{shift} (cm^{-1})	v_{rad} (km s^{-1})	%T	W±dW (cm^{-1})
P7	3290.35	3289.81	49	0.91	0.0154(0.0016)
P5	3296.49	3295.92	52	0.91	0.0184(0.0016)
P4	3299.53	3299.01	48	0.95	0.0183(0.0016)
P3	3302.53	3302.02	48	0.97	0.0162(0.0015)
P2	3305.54	3304.97	52	0.98	0.0136(0.0015)
R1	3317.33	3316.77	50	0.95	0.0128(0.0016)
R2	3320.22	3319.69	48	0.98	0.0179(0.0015)
R3	3323.09	3322.54	50	0.89	0.0212(0.0016)
R5	3328.78	3328.25	47	0.95	0.0222(0.0016)
R6	3331.59	3331.07	47	0.98	0.0236(0.0015)

5.2.2.2. GV Tau S. Interestingly, HCN absorption was not seen toward the primary star. If we assume the same T_{rot} as found for GV Tau N (115 K), the 3-sigma upper limit for the HCN column density toward GV Tau S, 4.8 x 10^{15} cm^{-2}, is about a factor of 8 lower than GV Tau N. The estimated CO column density toward GV Tau N is a factor of two higher than toward GV Tau S. If we assume that the CO absorption originates in the inner circumstellar disk of each object, then the resulting difference in HCN column densities implies that HCN is at least a factor of four less abundant toward the primary. This result is important. The fact that the HCN column density is significantly lower toward the primary is a strong constraint that argues for the HCN being located in the warm inner disk of the IRC, rather than in the interstellar medium or the circumbinary material that surrounds both objects.

This result may suggest that there are significant compositional differences between the inner disk (∼10 AU or so) material toward the two objects. However, we point out that caution must be used when comparing GV Tau N to GV Tau S. There is no a priori reason to assume the gas temperature is the same toward both objects if the gas is associated with a circumstellar disk rather than the circumbinary material. The primary was not located in the slit during our KL2 observation (Table 2.4), therefore only the J<8 transitions of HCN were covered by our observations. Due to the fact that only low J lines were sampled toward the primary, the upper limit is less constrained for higher temperatures. For example, if we assume T=400 K, then the upper limit for N(HCN) becomes ∼1.1x10^{17} cm^{-2}.

5.2.3. CH_4 Gas. We attempted to detect CH_4 in our KL, order 25 setting, which covered several transitions. With a geocentric Doppler shift of +49 km/s during the observations, the lines should have been shifted out of the telluric features to transmittances ranging from ∼60% for P2 up to ∼80% for R0 and P1 to 86% for R1. From this, we calculated a 3-sigma upper limit for the CH_4 column density of <2.2 x 10^{16} cm^{-2} using the methodology discussed in Gibb et al. (2004) and assuming the same rotational temperature as that found for HCN (115 K). When compared with the HCN and CO we find that CH_4/HCN < 60% and CH_4/CO < 0.19%. This is not as well constrained as the gas phase CH_4/CO ratio found for HL Tau (Gibb et al., 2004), but it is still substantially smaller than the overall CH_4/CO ratio found for comets (Gibb et al., 2003) and somewhat lower than reported for CH_4/CO (ice+gas) for massive YSOs by Boogert et al. (1997, 1998).

5.2.4. C_2H_2 Gas. There are two comparably strong bands of acetylene in the 3 μm region: the ν_3 band centered at 3294.84 cm^{-1} and the $\nu_2 + (\nu_4 + \nu_5)^0_+$ band centered at 3281.90 cm^{-1} (see Jacquemart et al. (2003) and references therein). Typically the ν_3 band is 1100 times stronger than the combination mode, but a Fermi resonance between the two bands causes the combination band to become slightly stronger than the ν_3 band (Vander Auwera et al., 1993).

From the analysis of the 3 μm spectra (Figure 2.15), a number of unblended lines of C_2H_2 are detected at relatively good transmittance (>80%). The positions of individual C_2H_2 lines are indicated in Figure 5.1 (dot-dash ticks). We analyzed 15 unblended lines with high transmittance from the $\nu_2 + (\nu_4 + \nu_5)^0_+$ band and 4 lines of the ν_3 band to determine the column density (Figure 5.3, Table 5.3). We also checked for possible contamination due to stellar photospheric features by comparison with an Arcturus spectrum. The rotational temperature analysis yielded a $T_{rot} = 170^{+19}_{-16}$ K, which is consistent with those found for HCN and CO within the uncertainty, and a total column density of $(7.3^{+0.1}_{-0.2})$ x 10^{16} cm^{-2}. These values are consistent with the non-detection of the ν_3 P18 line, which is at 97% transmittance and unblended. The predicted equivalent width of P18, based on the fit in Figure 5.3, is 0.0011 cm^{-1}, within the 1-sigma noise limit of 0.0014 cm^{-1}.

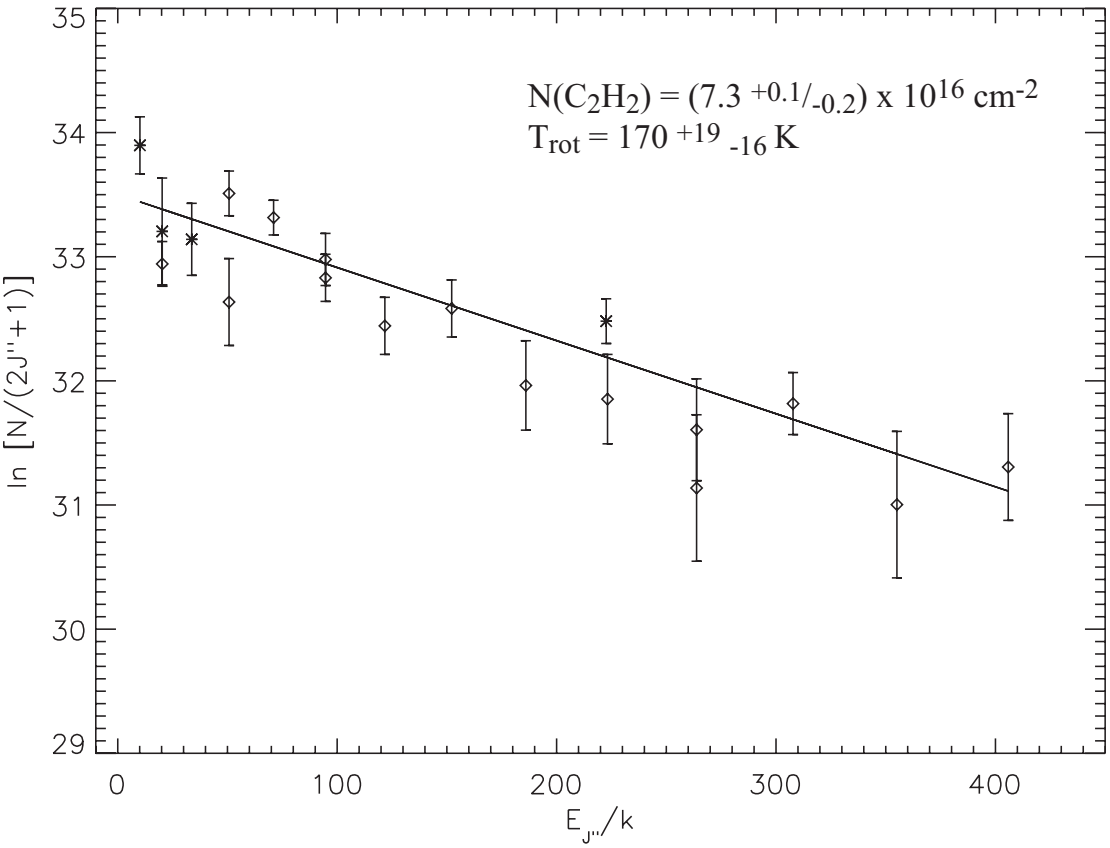

Figure 5.3 Population diagram for C_2H_2 absorption toward GV Tau N. Asterisks are data points from the ν_3 branch, diamonds are from the $\nu_2 + (\nu_4 + \nu_5)^0_+$ branch.

Table 5.3. C_2H_2 line positions and equivalent widths.

Line ID	ν_{rest} (cm^{-1})	ν_{shift} (cm^{-1})	%T	W±dW (cm^{-1})
ν_3 band				
R4	3306.48	3305.94	0.96	0.0067(0.0020)
P2	3290.13	3289.59	0.86	0.0058(0.0014)
P3	3287.75	3287.22	0.96	0.0044(0.0019)
P11	3268.48	3267.94	0.97	0.0077(0.0014)
$\nu_2 + (\nu_4 + \nu_5)^0_+$ band				
R15	3318.35	3317.81	0.90	0.0037(0.0016)
R12	3311.71	3311.17	0.88	0.0041(0.0017)
R10	3307.22	3306.68	0.95	0.0049(0.0018)
R7	3300.42	3299.88	0.91	0.0084(0.0016)
R5	3295.84	3295.31	0.95	0.0124(0.0014)
R3	3291.23	3290.69	0.86	0.0047(0.0016)
P5	3270.05	3269.52	0.94	0.0044(0.0016)
P6	3267.66	3267.12	0.94	0.0105(0.0015)
P7	3265.26	3264.72	0.78	0.0088(0.0018)
P8	3262.84	3262.31	0.95	0.0059(0.0014)
P9	3260.43	3259.89	0.84	0.0077(0.0017)
P11	3255.56	3255.03	0.84	0.0046(0.0017)
P12	3253.12	3252.59	0.95	0.0025(0.0014)
P13	3250.66	3250.13	0.98	0.0053(0.0013)
P14	3248.20	3247.67	0.95	0.0026(0.0015)
P18	3251.09	3250.56	0.97	<0.0014

5.3. DISCUSSION

We investigated the composition of several organic molecules toward the binary T Tauri system GV Tau. Such species as HCN, C_2H_2, and CH_4 are key to understanding the chemical compositions and evolution of the volatile material that becomes incorporated into the planet forming regions of disks around young stars. We detected HCN and C_2H_2 toward the IRC and provide upper limits for the primary. This is only the second reported detection of these species in the gas phase toward a low mass T Tauri star. The first reported detection of these molecules was via Spitzer IRS observations toward IRS 46 in the ρ Ophiuchi cloud (Lahuis et al., 2006). The warm temperatures ($\sim$400 K for HCN and $\sim$800 K for C_2H_2) suggested a possible disk origin for the absorptions, but were not definitive as Lahuis et al. (2006) could not distinguish whether the gas was located in the disk or a jet.

5.3.1. Location of the Gas Toward GV Tau. In February 2006, HCN was detected toward the IRC (GV Tau N, Fig. 2.15). However for GV Tau S, which was observed simultaneously, the lack of a detection suggests a significant lower total column density, assuming the same rotational temperature. Similarly, the

CO spectra toward GV Tau N and GV Tau S are significantly different, suggesting a factor of two difference in column density, resulting in a factor of at least four lower abundance toward the primary. This result is a strong indication that the HCN is located close to GV Tau N, within the circumstellar flared disk, and not associated with the primary (and thus not in the circumbinary material). The warm rotational temperatures of ∼100-200 K determined for HCN, C_2H_2, and CO also suggest a location in the inner region of the disk that surrounds GV Tau N rather than in the circumbinary envelope. A jet origin can likely be eliminated as the Doppler shifts of stellar photospheric absorption lines agree with those found for the intervening molecular material to within ∼5 km/s. We derive a heliocentric radial velocity of 21±5 km/s for CO and 19.5±3.4 km/s for HCN. This is similar the heliocentric Doppler shift of 13.4±3.8 km/s reported by White and Hillenbrand (2004) using high resolution optical spectra of stellar emission lines. The combination of velocity information, significantly different compositions toward closely spaced objects, and warm rotational temperatures argue that the HCN, C_2H_2, and CO are located in the disk of GV Tau N.

If we assume that the near-infrared variability toward GV Tau is due primarily to cooler material in the outer disk or circumbinary envelope rather than the warm material where the CO, HCN, and C_2H_2 absorptions originate, as suggested by the 3 μm ice feature variability, then we can compare our column densities of HCN and C_2H_2 to CO (see Table 5.1). We must be cautious with such an interpretation, however, since our CO (2 and 5 μm) observations and our 3 μm observations were taken at different times and the sources are both highly variable in the infrared over short time scales. This could affect the amount of gaseous material in the line of sight. For example, tidal interactions between the two stars, which are only separated by about 170 AU, may affect the gas structure close to the stars. Perhaps the temperature and density structures of the inner disks differ resulting in dissimilar chemical evolution. It may also be possible that an inner circumstellar disk of the primary is more inclined than the nearly edge-on GV Tau N and that we are seeing warm CO in the flared disk. This conclusion is supported by recent work by Roccatagliata et al. (2011), who reported that the southern companion, GV Tau S, is oriented almost face on, while GV Tau N is seen edge

on. The molecules in disk atmospheres are less protected from energetic photons than those in the midplane, leading to higher photodissociation rates. Collisional dissociation in the inner disk may act to remove hydrogen atoms from molecules like C_2H_2 and HCN. Also, the increased production of ions in disk atmospheres and the resulting ion-molecule chemistry will further modify the composition. The extent to which these processes occur is dependent on the local ionizing radiation field, temperature, and density (see papers by Willacy et al. (1998); Markwick et al. (2002); Aikawa et al. (1999, 2002) for discussion of chemistry in protoplanetary disks). Hence, the chemistry is dependent on radial and vertical distances in the disk and our measurements are correspondingly dependent on viewing geometry. Additional observations to simultaneously measure CO and HCN toward GV Tau are planned to address this issue and to investigate the possibility of variations in column densities of gaseous species.

5.3.2. Compositional Comparisons. It is interesting to compare our results for GV Tau N to those found toward other young stars, models of chemistry in protoplanetary disks, and comets in our own solar system. Assuming that CO, HCN, and C_2H_2 originate in the same region, we found a C_2H_2/HCN ratio of $\sim$2.0 toward GV Tau N and HCN/CO $\sim$ 0.31% and C_2H_2/CO $\sim$ 0.62%. C_2H_2/HCN was found to be $\sim$0.6 toward IRS 46 (Lahuis et al., 2006), another low mass object, assuming that both species originate in the same region. The 13-14 μm Q-branches and band heads of C_2H_2 and HCN were studied by ISO (Lahuis and van Dishoeck, 2000) toward massive YSOs. In general, C_2H_2/HCN for the warm component was found to be $\sim$40-50% toward most objects. Interestingly, HCN was found to be more abundant ($\sim$2.5%) toward IRS 46 compared to CO (this is a lower limit). This can be seen graphically in Figure 5.4. In that figure, C_2H_2/HCN is indicated by asterisks while the abundances of C_2H_2 and HCN relative to CO (in %) are indicated by filled squares and diamonds, respectively.

Markwick et al. (2002) modeled molecular distributions of abundant species in the inner 10 AU of protostellar disks surrounding T Tauri stars. Gibb et al. (2004) measured an upper limit for CH_4/CO toward HL Tau that was significantly lower than predicted by the model. The same was found for GV Tau N, where $CH_4/CO < 0.0019$ is much smaller than the CH_4/CO $\sim$1 predicted by Markwick

through most of the inner disk. However, we find that HCN/CO, C_2H_2/CO, and C_2H_2/HCN ratios toward GV Tau N are in general agreement with the range of abundances found in Markwick et al. (2002) (see Figure 5.4). Our rotational temperatures (∼100-200 K) are also consistent with the midplane temperatures in the inner ∼5 AU of the protoplanetary disk in the Markwick model. We note, however that we are likely sampling a region above the midplane, possibly in a disk atmosphere, which may be heated by various mechanisms such as viscous accretion, X-rays, or an X-wind (see Glassgold et al. (2004) for a discussion of disk heating). This would move the location of the gas outward by an amount depending on the local environment. Nonetheless, the similarity in abundances between Markwick et al. (2002), GV Tau, and IRS 46 is interesting and should be pursued further.

Another interesting comparison is with comets in our own solar system. Comets are generally considered to be the most pristine objects in the solar system and are thought to have formed in the giant-planet region (from ∼5-30 AU). Infrared spectroscopy has routinely measured abundances of CO, HCN, and C_2H_2 toward comets for the last decade (see Mumma et al. (2003) and references therein). HCN and C_2H_2 abundances measured in comets (compared to water) are fairly consistent over the Oort cloud population measured to date and the C_2H_2/HCN ratio is found to be typically ∼0.9-1.1, reasonably consistent with the C_2H_2/HCN ratios of 0.6 and 2.0 found for IRS 46 and GV Tau, respectively. The CO abundance in comets has been found to be highly variable, likely as a result of thermal history and processing of comets in the protoplanetary disk. The resulting HCN/CO and C_2H_2/CO ratios range from ∼0.01-0.16. The HCN/CO and C_2H_2/CO ratios found in GV Tau and IRS 46 are consistent with those found for CO rich comets. It is possible that the more volatile CO was preferentially lost in comets for which the HCN/CO or C_2H_2/CO ratios are high. If we assume that the comets with the greatest abundance of CO more closely represent the initial volatile abundance of the giant-planet forming region of the solar nebula, the resulting C_2H_2/HCN, C_2H_2/CO, and HCN/CO ratios agree to within a factor of two with those found for GV Tau N, IRS 46, massive YSOs, and several of the Markwick model results.

Also of interest is CH_4, another particularly volatile molecule for which the abundance (relative to water) has been observed to be highly variable in comets (by over an order of magnitude). While the magnitude of the abundance variation is similar to that found for CO in comets, the two molecules are not correlated (Gibb et al., 2003). In comets CH_4/CO is found to vary from ∼0.05–0.8, much higher than in HL Tau (<0.0002 in the gas phase) or GV Tau N (<0.0019), and lower than the CH_4/CO∼1 found by Markwick et al. (2002). CH_4/HCN is found to vary from ∼2–5 among comets yet is <0.6 toward GV Tau N. The reasons for these compositional differences are unknown and more work must be done to characterize volatiles toward comets and low mass star forming regions.

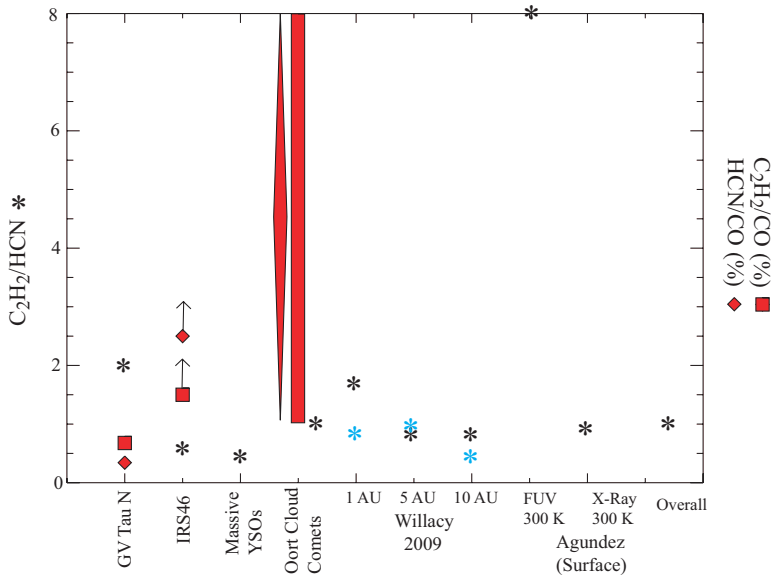

Figure 5.4 Figure comparing abundances toward GV Tau N, IRS 46, Massive YSOs, Oort Cloud Comets, and the chemical models of Willacy and Woods (2009) and Markwick et al. (2002). Black asterisks indicate the C_2H_2/HCN ratio from Markwick et al. (2002) while the blue asterisks are the ratios from Willacy and Woods (2009). We also note that those ratios are comparable to those reported by Walsh et al. (2010). Filled squares and diamonds indicate the abundances relative to CO of C_2H_2 and HCN, respectively.

5.4. CONCLUSION

We have measured column densities and rotational temperatures for CO, HCN, and C_2H_2 and an upper limit for CH_4 toward GV Tau N. We find that

the absorptions are consistent with an origin in the inner region of a protoplanetary disk. This conclusion is further strengthened by the lack of absorptions due to organic species toward the primary, GV Tau S, though gas phase CO is present. The upper limit for HCN toward the primary may suggest compositional differences between the two objects, though a different temperature or viewing geometry cannot be ruled out. We note that GV Tau is variable in the near-infrared, likely due to inhomogeneities in the circumbinary material or outer disk. Future observations at M and L band are planned to test whether the variability affects the column densities and abundances of the gas phase species reported in this paper.

We find that the abundances of HCN and C_2H_2 relative to each other and to CO are similar to those found among the comet population, that found toward low mass object IRS 46 by Lahuis et al. (2006), and consistent with the disk model by Markwick et al. (2002). CH_4, on the other hand, appears to be underabundant in the young stars sampled to date when compared to comets in our own solar system. This exciting result illustrates the feasibility of detecting minor volatile constituents toward low mass young stars from the ground, a study which is vitally important to understanding how our own system evolved.

6. DISCUSSION AND FUTURE WORK

6.1. DISCUSSION

In the introduction we proposed several questions regarding chemistry and molecular evolution in star forming regions. We looked at ices in the envelope and disk surrounding young stars and gases in the disk of the young star system GV Tau to probe answers to these questions.

The first question we asked was "What effect does nearby radiation (or a lack thereof) have on molecule formation?" We first looked at the formation of CO_2 in the solid phase toward the mixed-mass star forming region, Rho Ophiuchi. A comparison of the abundance of CO_2 ice with respect to H_2O ice for objects near intermediate-mass young stars and those near dense cores to those more distant from potential influences was completed. That comparison did not show a trend in abundance when compared to the distance from the intermediate mass young stars or dense cores. While sources close to the intermediate-mass young stars show an annealed CO_2 component, there are other sources that are more distant that also have crystalline CO_2, and sources that are at an intermediate distance that do not have crystalline CO_2. Therefore, a likely scenario is that the ice profiles are dominated by the local YSO rather than the intermediate young star. We also compared the abundances of CO_2 in Rho Oph to other star forming regions and toward background objects, and found similar average abundances toward Rho Oph, Taurus, Perseus, and background objects (17%-22%), but larger abundances toward Serpens and Corona Australis (30%-35%). Further comparisons are necessary to determine the circumstances responsible for this difference in abundance. We also found similar average abundances of CO_2 toward background objects, however, the percentage of the polar, apolar, and crystalline components of CO_2 differed for quiescent background objects and low mass YSOs. About 61% of our low mass YSOs had a crystalline component, while

there is no crystalline component visible toward background objects (see Bergin et al. (2005), Whittet et al. (2009), and Boogert et al. (2011)) and Whittet et al. (2009) report that 85% of the CO_2 ice is polar. The percentage of studied sources with the distinct double-peak structure that is indicative of crystalline CO_2 is roughly equal for Rho Oph and Taurus. The presence of crystalline CO_2 toward some YSOs that are not near energetic objects and the lack of crystalline CO_2 toward background objects suggests the heating necessary for crystallization may be due primarily to local affects from the actual YSO.

We also asked, "Are simple molecules formed in the gas phase, or are grain surface reactions necessary?" It is widely known that CO forms in the gas phase and freezes onto grains (see, for example, Pontoppidan et al. (2008)). However, other molecules such as H_2O, CH_3OH, and CO_2 predominately form ices on the grain via grain surface reactions (Tielens and Hagen, 1982). In this study, we found that some objects with Flat and Class II SEDs have greater abundances of CO_2. This may be the result of the activation of an additional formation route of CO_2 in some objects transitioning from envelope and disk to objects with a disk but an envelope that has been heavily dispersed. In addition, we found that the CO_2 absorption features in our sample can be described by mixtures of polar and apolar ices, polar and annealed ices, or polar, apolar, and annealed ices. This agrees with the accepted description of the formation of ices: ices form in layers on the grain, a polar layer followed by an apolar layer, and finally heating occurs, crystallizing portions of either or both layers. This layered formation answers the question with regard to forming ices on the grain, "If they are formed on the grain, is it in a polar environment (with H_2O) or an apolar environment?" This result simply confirms previous studies; ices form in layers on grain mantles, a polar layer and then an apolar layer.

Most solid ices form or condense at temperatures less than $\sim$150 K, corresponding to a location in the outer region of the midplane of the disk and in the envelope surrounding the YSO. In the inner portion of the midplane, the warm molecular layer, and the upper portion (photodissociation region) of the flared disk, molecules are present in the gas phase. We reported just the second the detection of the organic molecules HCN and C_2H_2 in the gas phase toward a low

mass YSO. In addition, CO was detected toward the same object, the infrared companion of GV Tau, GV Tau N. Rotational temperatures for those species ranged from ∼100 K - 200 K, consistent with temperatures predicted for the inner 5 AU of the midplane of the disk by Markwick et al. (2002). However, we note that it is also possible for the gas to be located in the region above the midplane, possibly a disk atmosphere. Heating of this gas by various mechanisms such as viscous accretion, X-rays, or an X-wind would result in a gas location futher outward in the disk, the distance determined by an amount depending on the local environment. However, the similarity in abundances of HCN and C_2H_2 relative to each other and CO between GV Tau, IRS 43 (Lahuis et al., 2006), the disk model by Markwick et al. (2002) and comets is an interesting result and should be further studied. Understanding where and how these molecules form has important implications for the evolution of our solar system.

Of course, the ultimate goal is to study other star forming regions and young stars in order to learn about the evolution of our solar system. We inquired about the environment in which our solar system formed. Was it in the presence of other stars? If so, was it a region like Rho Oph, where there are intermediate stars? Or did it form in relative isolation like stars in Taurus? This is, in fact, an open question. Recent studies of meteorites that have found evidence of several short-lived nuclides, such as ^{41}Ca, ^{26}Al, and ^{60}Fe that were present in the early solar system (Goswami et al., 2000). There are two possible causes for these short-lived nuclides. It is possible that the abundance of heavy elements found in meteorites were injected into the early protostellar cloud from nearby supernova explosions (Goswami et al., 2000). This would imply that our solar system formed in the presence of high mass stars, and that the molecular cloud was a mixed-mass region of star formation, perhaps similar to Rho Ophiuchi. If this is the case, the abundance of nuclides in our solar system provides a constraint of the timescale during which the protostellar cloud collapsed into a disk and formed planets. Alternatively, it is possible that the heavy elements found in meteorites formed in the protostellar cloud from the collision of energetic particles, such as cosmic rays, with the dust and gas with the protostellar cloud and/or protostellar nebula (Goswami et al., 2000). This suggestion that these radionuclides formed in situ

rather than being injected would indicate that our natal molecular cloud may have been one with low mass star formation similar to Taurus, but it does not exclude high mass stars in the same region. Therefore, we have compared the abundances and mixtures of CO_2 ice in Rho Oph with several different star forming regions, as well as high mass YSOs and background objects to look for unique diagnostic characteristics. We found that the two regions for which we have data for the most YSOs, Taurus and Rho Oph, show a linear correlation between the column densities of CO_2 and H_2O. While there is a correlation, there is scatter in the data, much more than toward background objects, YSOs in Corona Australis, YSOs in Serpens, and all low-mass YSOs in the five star forming regions. In addition, we found similar average abundances of CO_2 ice with respect to H_2O ice toward our YSOs in Rho Oph and compiled published values toward Taurus, Perseus, and low mass YSOs. The average abundances agree with the values cited by Oberg et al. (2011) for high mass YSOs, but not for low mass YSOs or background objects. We note, however, that our sample includes data that is not included in the Oberg et al. (2011) values: this work, Zasowski et al. (2009), Whittet et al. (2007), and Whittet et al. (2009). Finally, the abundance of CO_2 ice with respect to H_2O ice for Corona Australis and Serpens is greater than that for Rho Oph, Taurus, Perseus, and all low-mass objects toward the five star forming regions. The scatter, small differences in abundance between star forming regions, and differences in the amount of crystalline, or processed, CO_2 as compared to background sources are likely due to the local YSO rather than the general conditions of the molecular cloud. Characterization of other volatiles is necessary to determine the evolution of simple ices in star forming regions.

6.2. FUTURE WORK

Some of those volatiles reside in the 5-8 μm region, and include molecules such as CH_4, NH_3, CH_3OH, and the unknown carrier of the 6.8 μm absorption feature. In this section we will provide two discussions; the first will describe the molecules we can study with the Spitzer spectra presented in this work and the second will propose future observations that will improve the data quality and try to illucidate some long-standing questions.

6.2.1. Molecules in the Spectral Range of the Spitzer Space Telescope. The data that have been presented in this dissertation can be used to characterize several additional ice absorptions. For example, there is an absorption at 6.8 μm caused by an unknown carrier. Originally, this band was attributed to CH_3OH (Tielens and Allamandola, 1987). However, with the launch of ISO, it was found that CH_3OH was unable to account for the full absorption feature, nor was a second proposed carrier, NH_4^+ (Keane et al., 2001). Keane et al. (2001) proposed that the feature could be decomposed into two components, a long wavelength component characterized by the profile present in Mon R2:IRS3 (component 2), and a short wavelength component characterized by the profile of NGC 7538:IRS9 with the profile of Mon R2:IRS3 removed since the long wavelength portion of this component can be described by component 2. This modified component is referred to as component 1. They attributed these two components to thermal processing of a single species, but did not find a conclusive carrier. Boogert et al. (2008) also included an analysis of this feature, using a similar decomposition as Keane et al. (2001), which they refer to as the components C3 and C4. They found that the C4 component is present toward both background objects and YSOs, and suggested the carrier is NH_4^+, as described by Schutte and Khanna (2003). They proposed that the C4 component is the result of heating the sample, shifting the C3 component to the C4 position, but noted that the high temperatures needed to cause this shift were not present in many of the sources in their sample. Clearly, the mystery of the 6.8 μm feature has yet to be solved. For our Rho Oph data, this feature could be extracted by subtracting the best laboratory fit for absorption at 6 μm that contains H_2O, H_2CO, and HCOOH from the optical depth of each source, and then applying the methods used by Keane et al. (2001) and Boogert et al. (2008) to characterize the short and long wavelength components.

There are other minor species in the spectral range of the Spitzer Space Telescope. These include the C=O stretch modes of $HCOO^-$ at 7.25 μm and 7.41 μm, the C-H deformation mode of HCOOH at 7.25 μm, the C-H ν_4 deformation mode of CH_4at 7.70 μm, the CH_3OH C-H_3 rock mode and C-O stretch mode at 8.9 μm and 9.75 μm, respectively, and the umbrella mode of NH_3 at 9.35 μm (see D'Hendecourt and Allamandala (1986), Schutte et al. (1999), and Boogert

et al. (1997) for absorption positions at band strengths). Analysis techniques for characterizing these molecular species are described in Boogert et al. (2008), Oberg et al. (2008), and Bottinelli et al. (2010).

6.2.2. Future Observations. First, as was mentioned in § 4.2, increasing the number of observations of YSOs toward Perseus, Corona Australis, and Serpens is essential to confirm the tighter correlation between H_2O and CO_2. This study, as well as a comparison between the 3 μm stretching mode and 6 μm bending mode of H_2O are the first suggestion for future work. The comparison of H_2O modes is necessary because of the inability of H_2O, H_2CO, and HCOOH to account for the full absorption at 6 μm toward some YSOs. Gibb and Whittet (2002) have suggested the additional absorption is due to organic refractory material. Boogert et al. (2008) propose a portion of this excess could be explained by HCOOH or by using an enhanced band strength of CO_2 rich ices discussed by Knez et al. (2005). A future study involving a direct comparison of the stretching and bending modes of H_2O ice toward several star forming regions could help answer this question. At this time, there is no space-based telescope with the capability of covering both the 3 μm and 6 μm water ice features. However, EXES on the Straospheric Observatory for Infrared Astronomy (SOFIA) does contain the bending mode in its spectral grasp, at a much higher resolving power than IRS on Spitzer, $\sim$4000 in its low resolution mode, and the 3 μm mode is observable from the ground. In addition, there are two instruments (NIRSpec and MIRI) proposed for use on the James Webb Space Telescope, JWST, which would cover both H_2O ice modes. Observations of the 3 μm stretching mode from space would be particularly exciting since it would eliminate the problem of H_2O absorption from our atmosphere. The current launch date for the JWST is 2014.

In addition to providing higher resolution data of the 6 μm H_2O ice feature that can be compared with the 3 μm stretching mode, observations with either of SOFIA or JWST would provide better resolution of the 5-8 μm complex. Given the low resolving power of the SL mode of IRS on the Spitzer Space Telescope ($\sim$60) higher resolution data could really elucidate the spectral region. Using information from the EXES website[1], all but six of our Rho Oph sources would be

[1] $http://www.sofia.usra.edu/Science/instruments/instruments_exes.html$

detectable with 15 minutes of integration time. At the edge of the spectral range of EXES lies the stretching mode of CO at 4.67 μm. A study similar to those of Pontoppidan et al. (2008) and Cook et al. (2011) comparing CO and CO_2 ices toward our Rho Oph sources would be a useful diagnostic as far as determining whether distillation or segregation is responsible for the crystalline CO_2 ice we see toward YSOs. The same comparison could be made with JWST, with the added benefit of including the C-H stretching modes of CH_3OH at 3.53 μm and 3.95 μm, the C-O stretch of CO_2 at 4.27 μm, the ^{13}C-O stretch mode of $^{13}CO_2$ at 4.38 μm, and the CN stretch of "XCN" at 4.62 μm, (see D'Hendecourt and Allamandala (1986), Gerakines et al. (1995), and Schutte and Greenberg (1997) for absorption positions and bandstrengths).

It is evident that this study only begins to characterize the evolution of volatiles during the star formation process. Instruments such as ISO and Spitzer have revolutionized spectroscopy and are partly responsible for the introduction of a new field, Astrochemistry. Even since then, technology has improved and we have other instruments to carry on the legacies of ISO and Spitzer. The use of SOFIA and the launch of the JWST will further transform our knowledge of chemistry in the interstellar medium and could provide great progress toward understanding the formation of our own solar system.

APPENDIX: PERMISSION FOR FIGURES

Permission from Dr. D.C.B. Whittet for Figures 1.1 and 1.2

Hi Kari,

You are welcome to reproduce those figures!

Doug Whittet

Permission from Dr. D. Semenov for Figure 1.3

Dear Kari (if I may),

sure, go ahead! I'm always pleased to hear that someone finds my work useful :) Good luck with preparing your thesis and PhD defense!

Cheers, Dima

Permission from Dr. K. Willacy for Figure 1.3

Hi Kari

Yes that is fine with me

Karen

Permission from Laurie Hatch for Figure 2.13

Hi Kari,

You are welcome to call me Laurie, and I'm glad you like the images!

What is your dissertation topic? (I'm married to an astronomer ... :)

I'm happy to provide these images for your dissertation. What approximate size and print resolution do you need (i.e., 5"x7"-ish at 300ppi)? I realize you might not know precisely until you have the high resolution files placed in your layout to see how everything fits.

But I suggest you err on the high side resolution-wise as you probably know it is better to resize the files down than up.

In addition, do you wish to use these images in an associated powerpoint presentation, or to post them on the web as a part of your dissertation? If the latter, I usually do not allow posting of files on the web in excess of 500 pixels in the longest dimension, although exceptions are sometimes made. I shall provide separate, dedicated files for powerpoint or for online use which are optimized for those respective applications, and which have my visual and digitally embedded watermarks. Please do not generate your own powerpoint or web files from provided hi-res print files, rather, send me the required pixel dimensions and I'll prepare suitable files with embedded copyright credit and digital watermarks. If such images are used on the web, please send me the URL(s). Along with the photographs, please include a copyright and credit notice: ©LaurieHatch.com
I ask that you not forward this information to colleagues or other inquirers; rather; they should contact me directly about image use.

My Academic Image Use Caveats are located in a private, invitation-only gallery on my otherwise publicly accessible website:

http://lauriehatch.com/Image.asp?ImageID=1269904&AKey=6Q457TBG

If you've not already done so, you might check the Keck Gallery on my website to see if there are other images which you prefer or would like to use in addition to those requested.

Thank you for your interest,

Laurie

Permission from Dr. E.L. Gibb for figures & tables in §5

Kari,

I give you permission to reproduce the figures and tables from Gibb et al., 2007, ApJ, 660, 1572-1579 in your dissertation.

Dr. Gibb

BIBLIOGRAPHY

Abergel, A., Bernard, J. P., Boulanger, F., Cesarsky, C., D'esert, F.X., Falgarone, E., Lagache, G., and 15 co-authors, "ISOCAM Mapping of the ρ Ophiuchi Main Cloud," *Astronomy & Astrophysics*, Vol. 315, pp. L329-L332.

Adams, F. C. 2010, "The Birth Environment of the Solar System," *Annual Review of Astronomy and Astrophysics*, Vol. 48, pp. 47-85.

Adams, W. S. 1941, "Some Results with the Coudé Spectrograph of the Mount Wilson Observatory," *The Astrophysical Journal*, Vol. 93, pp. 11-27.

Aikawa, Y., Umebayashi, T., Nakano, T., & Miyama, S. M. 1999, "Evolution of Molecular Abundances in Proto-Planetary Disks With Accretion Flow," *The Astrophysical Journal*, Vol. 519, No. 2, pp. 705-725.

Aikawa, Y., van Zadelhoff, G. J., van Dishoeck, E. F., & Herbst, E. 2002, "Warm Molecular Layers in Protoplanetary Disks," *Astronomy & Astrophysics*, Vol. 386, No. 2, pp. 622-632.

André, P., Ward-Thompson, D., Barsony, M. 1993, "Submillimeter Continuum Observations of ρ Ophiuchi A: The Candidate Protostar VLA 1623 and Prestellar Clumps," *The Astrophysical Journal*, Vol. 406, pp. 122-141.

Armitage, P. J. 2011, "Dynamics of Protoplanetary Disks," *Annual Review of Astronomy and Astrophysics*, Vol. 49, pp. 195-236.

Bachiller, R. 1996, "Bipolar Molecular Outflows From Young Stars and Protostars," *Annual Review of Astronomy and Astrophysics*, Vol. 34, pp. 111-154.

Bates, D. R. & Spitzer, L. 1951, "An International Review of Spectroscopy and Astronomical Physics," *The Astrophysical Journal*, Vol. 113, No. 3, pp. 441-463.

Bell, M. B., Feldman, P. A., Watson, J. K. G, McCarthy, M. C., Travers, M. J., and two co-authors 1999, "Observations of Long C_nH Molecules in the Dust Cloud TMC-1," *The Astrophysical Journal*, Vol. 518, No. 2, pp. 740-747.

Bergin, E. A., Melnick, G. J., Gerakines, P. A., Neufeld, D. A., Whittet, D. C. B. 2005, "Spitzer Observations of CO_2 Ice Toward Field Stars in the Taurus Molecular Cloud," *The Astrophysical Journal*, Vol. 627, pp. L33-L36.

Bevington, P. R. and Robinson, D. K., *Data Reduction and Error Analysis for the Physical Sciences (Third Edition)*, McGraw-Hill Higher Eduction: New York, New York (2003).

Boogert, A. C. A., Schutte, W. A., Helmich, F. P., Tielens, A. G. G. M., & Wooden, D. H. 1997, "Infrared Observations and Laboratory Simulations of Interstellar CH_4 and SO_2," *Astronomy & Astrophysics*, Vol. 317, pp. 929-941.

Boogert, A. C. A., Helmich, F. P., van Dishoeck, E. F., Schutte, W. A., Tielens, A. G. G. M., & Whittet, D. C. B. 1998, "The Gas/Solid Methane Abundance Ratio Toward Deeply Embedded Protostars," *Astronomy & Astrophysics*, Vol. 336, pp. 352-358.

Boogert, A. C. A., Tielens, A. G. G. M., Ceccarelli, C., Boonman, A. M. S., van Dishoeck, E. F.,and 3 co-authors 2000, "Infrared Observations of Hot Gas and Cold Ice Toward the Low Mass Protostar Elias 29," *Astronomy & Astrophysics*, Vol. 360, pp. 683-698.

Boogert, A. C. A., Hogerheijde, M. R., & Blake, G. A. 2002, "High-Resolution 4.7 micron Keck/NIRSPEC Spectra of Protostars. I. Ices and Infalling Gas in the Disk of L1489 IRS," *The Astrophysical Journal*, Vol. 568, No. 2, pp. 761-770.

Boogert, A. C. A., Ehrenfreund, P. 2004, "Interstellar Ices," *The Astrophysics of Dust*, ASP Conference Series, Vol. 309, pp. 547-572.

Boogert, A. C. A., Pontoppidan, K. M., Knez, C., Lahuis, F., Kessler-Silacci, J., and 21 coauthors 2008, "The c2d Spitzer Spectroscopic Survey of Ices Around Low-Mass Young Stellar Objects. I. H_2O and the 5-8 μm Bands," *The Astrophysical Journal*, Vol. 678, No. 2, pp. 985-1004.

Boogert, A. C. A., Huard, T.L., Cook, A. M., Chiar, J. E., Knez, C., Decin, L., Blake, G. A., Tielens, A. G. G. M., and van Dishoeck, E.F. 2011, "Ice and Dust in the Quiescent Medium of Isolated Dense Cores," *The Astrophysical Journal*, Vol. 729:92, pp. 1-16.

Bottinelli, S., Boogert, A. C. A., Bouwman, J., Beckwith, M., van Dishoeck, E. F., Oberg, K.I., et al.2010, "The c2d Spitzer Spectroscopic Study of Ices Around Low-Mass Young Stellar Objects. IV. NH_3 and CH_3OH," *The Astrophysical Journal*, Vol. 718, pp. 1100-1117.

Brittain, S. D., Rettig, T. W., Simon, T., Kulesa, C., DiSanti, M. A., & Dello Russo, N. 2003, "CO Emission from Disks Around AB Aurigae and HD 141569: Implications for Disk Structure and Planet Formation Timescales," *The Astrophysical Journal*, Vol. 588, No. 1, pp. 535-544.

Brittain, S. D., Rettig, T. W., Simon, T., & Kulesa, C. 2005, "CO Line Emission and Absorption from the HL Tauri Disk–Where Is All the Dust?" *The Astrophysical Journal*, Vol. 626, No. 1, pp. 283-291.

Cami, J., Bernard-Salas, J., Peeters, E., Malek, S. E. 2010 "Detection of C_{60} and C_{70} in a Young Planetary Nebula," *Science*, Vol. 329, No. 5996, pp. 1180-1182.

Carpenter, J. M., Heyer, M. H., Snell, R. L., 2000 "Embedded Stellar Clusters in the W3/W4/W5 Molecular Cloud Complex," *The Astrophysical Supplement Series*, Vol. 130, No. 2, pp. 381-402.

Cernis, K. 1990, "Interstellar Extinctin in the Vicinity of the Reflection Nebula NGC 1333 in Perseus," *Astrophysics and Space Science*, Vol. 166, No. 2, pp. 315-330.

Cheung, A. C., Rank, D. M., Townes, C. H., Thornton, D. D., and Welch, W. J. 1969 "Detection of Water in Interstellar Regions by its Microwave Radiation," *Nature*, Vol. 221, pp. 626-628.

Chiar, J. E., Adamson, A. J., Pendleton, Y, J., Whittet, D. C. B., Caldwell, D. A., & Gibb, E. L. 2002, "Hydrocarbons, Ices, and "XCN" in the Line of Sight toward the Galactic Center," *The Astrophysical Journal*, Vol. 570, No. 1., pp. 198-209.

Chiar, J. E., Pendleton, Y. J., Allamandola, L. J., Boogert, A. C. A., Ennico, K., Greene, T. P. and 11 co-authors 2011, "Ices in the Quiescent IC 5146 Dense Cloud," *The Astrophysical Journal*, Vol. 731, pp. 9-22.

Cook, A. M., Whittet, D. C. B., Shenoy, S. S., Gerakines, P. A., White, D. W., and Chiar, J. E. 2011, "The Thermal Evolution of Ices in the Environments of Newly Formed Stars: The CO_2 Diagnostic," *The Astrophysical Journal*, Vol. 730, pp. 124-138.

Cox, P. 1989, "The Line of Sight Towards AFGL 961: Detection of the Libration Band of Water Ice at 13.6 μm," *Astronomy & Astrophysics*, Vol. 225, pp. L1-L4.

Cuppen, H. M., Ioppolo,S., Romanzin, C., Linnartz, H. 2010, "Water Formation at Low Temperatures by Surface O_2 Hydrogenation II: The Reaction Network," *Physical Chemistry Chemical Physics*, Vol. 12, pp. 12077-12088.

Cushing, M. C., Vacca, M. D., Rayner, J.T. 2004, "Spextool: A Spectral Extraction Package for SpeX, a 0.8-5.5 Micron Cross-Dispersed Spectrograph," *The Publications of the Astronomical Society of the Pacific*, Vol. 116, pp. 362-376.

de Graauw, Th., Whittet, D. C. B., Gerakines, P. A., Bauer, O. H., Beintema, D. A., and 27 co-authors 1996, "SWS Observations of Solid CO_2 in Molecular Clouds," *Astronomy & Astrophysics*, Vol. 315, pp. L345-L348.

Devine, D., Reipurth, B., Bally, J., & Balonek, T. J. 1999, "A Giant Herbig-Haro Flow from Haro 6-10," *The Astronomical Journal*, Vol. 117, No. 6, pp. 2931-2940.

De Zeeuw, P. T., Hoogerwerf, R., Bruijine, J. H. J., Brown, A. G. A., and Blaauw, A. 1999, "A Hipparcos Census of Nearby OB Associations," *The Astronomical Journal*, Vol. 117, No. 1, pp. 354-399.

DiSanti, M. A., Mumma, M. J., Dello Russo, N., & Magee-Sauer, K. 2001, "Carbon Monoxide Production and Excitation in Comet C/1995 O1 (Hale-Bopp): Isolation of Native and Distributed CO Sources," *Icarus*, Vol. 153, pp. 361-390.

D'Hendecourt, L. B., Allamandola, L. J., and Greenberg, J. M. 1985, "Time Dependent Chemistry in Dense Molecular Clouds. I - Grain Surface Reactions, Gas/Grain Interactions and Infrared Spectroscopy," *Astronomy & Astrophysics*, Vol. 152, No. 1, pp. 130-150.

D'Hendecourt, L. B. and Allamandola, L. J. 1986, "Time Dependent Chemistry in Dense Molecular Clouds. III - Infrared Band Cross Sections of Molecules in the Solid State at 10 K," *Astronomy and Astrophysics Supplement Series*, Vol. 64, No. 3, pp. 453-467.

Douglas, A. E. & Herzberg, G. 1941, "CH^+ in Interstellar Space and in the Laboratory," *The Astrophysical Journal*, Vol. 94, pp. 381.

Dulieu, F., Amiaud, L., Fillion, J.-H., Matar, E., Momeni, A., and two co-authors 2010, "Experimental Evidence for Water Formation on Interstellar Dust Grains by Hydrogen and Oxygen Atoms," *Astronomy & Astrophysics*, Vol. 512, A30.

Dullemond, C. P. and Monnier, J. D. 2010, "The Inner Regions of Protoplanetary Disks," *Annual Reviews of Astronomy and Astrophysics*, Vol. 48, pp. 205-239.

Dunham, T. 1937, "Interstellar Neutral Potassium and Neutral Calcium," *Publications of the Astronomical Society of the Pacific*, Vol. 49, pp. 26-28.

Dzib, S., Loinard, L., Mioduszewski, A. J., Boden, A. F., Rodriguez, L. F., and Torres, R. M. 2010, "VLBA Determination of the Distance to the Nearby Star-Forming Regions. IV. A Preliminary Distance to the Proto-Herbig AeBe Star EC 95 in the Serpens Core," *The Astrophysical Journal*, Vol. 718, No. 2, pp. 610-619.

Eddington, A. S. 1926, "Bakerian Lecture. Diffuse Matter in Interstellar Space," *Proceedings of the Royal Society of London Series A*, Vol. 111, pp. 424-456.

Eddington, A. S. 1937, "Interstellar Matter," *The Observatory*, Vol. 60, pp. 99-103.

Ehrenfreud, P., Kerkhof, O., Schutte, W. A., Boogert, A. C. A., Gerakines, P. A., and 5 co-authors 1999, "Laboratory Studies of Thermally Processed H_2O:CH_3OH:CO_2 Ice Mixtures and their Astrophysical Implications," *Astronomy & Astrophysics*, Vol. 350, pp. 240-253.

Ehrenfreund, P., & Charnley, S. B. 2000, "Organic Molecules in the Interstellar Medium, Comets, and Meteorites: A Voyage from Dark Clouds to the Early Earth," *Annual Review of Astronomy and Astrophysics*, Vol. 38, pp. 427-483.

Erickson, K. L., Wilking, B. A., Meyer, M. R., Robinson, J. G., and Stephenson, L. N. 2011, "The Initial Mass Function and Disk Frequency of the ρ Ophiuchi Cloud: An Extinction-Limited Sample," *The Astronomical Journal*, Vol. 142, pp. 140-138.

Foing, B. H. & Ehrenfreund, P. 1997 "New Evidences for Interstellar C_{60}^{+}," *Astronomy & Astrophysics*, Vol. 317, pp. L59-62.

Fournier, J., Deson, J., Vermeil, C., Pimentel, G. C. 1979 "Fluorescence and Thermoluminescence of N_2O, CO, and CO_2 in an Argon Matrix at Low Temperature," *The Journal of Chemical Physics*, Vol. 70, pp. 5726-5730.

Gagné, M., Skinner, S. L., Daniel, K. J. 2004, "Simultaneous *Chandra* and Very Large Array Observations of Young Stars and Protostars in ρ Ophiuchus Cloud Core A," *The Astrophysical Journal*, Vol. 613, pp. 393-415.

Garrod, R. T. and Pauly, T. 2011, "On the Formation of CO_2 and Other Interstellar Ices," *The Astrophysical Journal*, Vol. 735, pp. 15-32.

Gehrz, R. D., Roellig, T. L., Werner, M. W., Fazio, G. G., Houck, J. R., Low, F. J. and four co-authors 2007, "The NASA Spitzer Space Telescope," *Review of Scientific Instruments*, Vol. 78, pp. 011302-1-011302-38.

Gerakines, P. A., Schutte, W. A., Greenberg, J. M., van Dishoeck, E. F. 1995, "The Infrared Band Strengths of H_2O, CO, and CO_2 in Laboratory Simulations of Astrophysical Ice Mixtures," *Astronomy & Astrophysics*, Vol. 296, pp. 810-818.

Gerakines, P. A., Schutte, W. A., Ehrenfreund, P. 1996, "Ultraviolet Processing of Interstellar Ice Analogs. I. Pure Ices." *Astronomy & Astrophysics*, Vol. 312, pp. 289-305.

Gerakines, P. A., Whittet, D. C. B., Ehrenfreund, P., Boogert, A. C. A., Tielens, A. G. G. M., and 6 co-authors 1999, "Infrared Space Observatory with the Observations of Solid Carbon Dioxide in Molecular Clouds," *The Astrophysical Journal*, Vol. 522, No. 1, pp. 357-377.

Gibb, E. L., Whittet, D. C. B., Schutte, W. A., Boogert, A. C. A., Chiar, J. E., Ehrenfreund, P., and five co-authors 2000, "An Inventory of Interstellar Ices Toward the Embedded Protostar W33A," *The Astrophysical Journal*, Vol. 536, pp. 347-356.

Gibb, E.L. and Whittet, D. C. B. 2002, "The 6 Micron Feature in Protostars: Evidence for Organic Refractory Material," *The Astrophysical Journal*, Vol. 566, pp. L113-L116.

Gibb, E. L., Mumma, M. J., Dello Russo, N., DiSanti, M. A., & Magee-Sauer, K. 2003, "Methane in Oort Cloud Comets," *Icarus*, Vol. 165, No. 2, pp. 391-406.

Gibb, E. L., Brittain, S. D., Rettig, T. W., Kulesa, C., & Simon, T. 2004, "The Upper Limit for CH_4 in the Protostellar Disk Toward HL Tauri," *The Astrophysical Journal*, Vol. 610, pp. L113-L116.

Gibb, E. L.; Whittet, D. C. B.; Boogert, A. C. A.; Tielens, A. G. G. M. 2004, "Interstellar Ice: The Infrared Space Observatory Legacy," *Astrophysical Journal Supplement Series*, Vol. 151, pp. 35-73.

Gibb E. L., Van Brunt K. A., Brittain, S. D., and Rettig, T. W. 2007, "Warm HCN, C_2H_2, and CO in the Disk of GV Tau", *The Astrophysical Journal*, Vol. 660, pp. 1572-1579.

Gillett, F. C. & Forrest, W. J. 1973, "Spectra of the Becklin-Neugebauer Point Source and the Kleinmann-Low Nebula from 2.8 to 13.5 microns," *The Astrophysical Journal*, Vol. 179, pp. 483-491.

Glassgold, A. E., Najita, J., & Igea, J. 2004, "Heating Protoplanetary Disk Atmospheres," *The Astrophysical Journal*, Vol. 615, No. 2, pp. 972-990.

Goodrich, R. W. 1986, "New Observations of Herbig-Haro Objects and Related Stars," *The Astronomical Journal*, Vol. 92, No. 4, pp. 885-894.

Goswami, J., and Vanhala, H. *Protostars and Planets IV, ed. V. Mannings, A. P. Boss, S. S. Russell*, University of Arizona Press: Tucson, Arizona (2000), pp. 963-994.

Greene, T. P., Wilking, B. A., André, P., Young, E. T., and Lada, C. J. 1994, "Further Mid-Infrared Study of the ρ Ophiuchi Cloud Young Stellar Population: Luminosities and Masses of Pre-Main-Sequence Stars," *The Astrophysical Journal*, Vol. 434, pp. 614-626.

Grim, R. J. A. and d'Hendecourt, L. B. 1986, "Time-Dependent Chemistry in Dense Molecular Clouds IV. Interstellar Grain Surface Reactions Inferred From a Matrix Isolation Study," *Astronomy and Astrophysics*, Vol. 167, pp. 161-165.

Haas, M. R., Davidson, J. A., Erickson, E. F., eds. 1995, "Airborne Astronomy Symp. Galactic Ecosystem: From Gas to Stars to Dust," *ASP Conference Series*, Vol. 73, pp. 591-812.

Hagen, W., Tielens, A. G. G. M., & Greenberg, J. M. 1981, "The Infrared Spectra of Amorphous Solid Water and Ice I_c between 10 and 140 K," *Chemical Physics*, Vol. 56, No. 3., pp. 367-379.

Haisch, K. E., Lada, E. A., and Lada, C. J. 2001, "Disk Frequencies and Lifetimes in Young Clusters," *The Astrophysical Journal*, Vol. 553, No. 2, pp. L153-L156.

Harris, G. J., Polyansky, O. L., & Tennyson, J. 2002, "Opacity Data for HCN and HNC from a new AB Initio Line List," *The Astrophysical Journal*, Vol. 578, pp. 657-663.

Hasegawa, T. I., Herbst, E., and Leung, C. M. 1992, "Models of Gas-Grain Chemistry in Dense Interstellar Clouds with Complex Organic Molecules," *Astrophysical Journal Supplement Series*, Vol. 82, No. 1, pp. 167-195.

Higdon, S. J. U., Devost, D., Hidgon, J. L., Brandl, B. R., Houck, J. R., and 6 co-authors 2004, "The SMART Data Analysis Package for the Infrared Spectrograph on the Spitzer Space Telescope," *Publications of the Astronomical Society of the Pacific*, Vol. 116, pp. 975-984.

Hinkle, K., Wallace, L., & Livingston, W. 1995, "Infrared Atlas of the Arcturus Spectrum, 0.9-5.3 microns," *Publications of the Astronomical Society of the Pacific*, Vol. 107, pp. 1042-1046.

Hudgins, D. M., Sandford, S. A., Allamandola, L. J., and Tielens, A. G. G. M. 1993, "Mid- and Far-Infrared Spectroscopy of Ices - Optical Constants and Integrated Absorbances," *Astrophysical Journal Supplement Series*, Vol. 86, No. 2, pp. 713-870.

Houck, J. R.; Roellig, T. L.; van Cleve, J.; Forrest, W. J., Herter, T., and 30 coauthors 2004, "The Infrared Spectrograph (IRS) on the *Spitzer Space Telescope*," *The Astrophysical Journal Supplement Series*, Vol. 154, pp. 18-24.

Ioppolo, S., Cuppen, H. M., Romanzin, C., Van Dishoeck, E. F., and Linnartz, H. 2008, "Laboratory Evidence for Efficient Water Formation in Interstellar Ices," *The Astrophysical Journal*, Vol. 686, pp. 1474-1479.

Ioppolo, S., Cuppen, H. M., Romanzin, C., van Dishoeck, E. F., and Linnartz, H. 2010, "Water Formation at Low Temperatures by Surface O_2 Hydrogenation I: Characterization of Ice Penetration," *Physical Chemistry Chemical Physics*, Vol. 12, Issue 38, pp. 12065-12076.

Ioppolo, S., van Boheemen, Y., Cuppen, H. M., van Dishoeck, E. F., and Linnartz, H. 2011 "Surface Formation of CO_2 Ice at Low Temperatures," *Monthly Notices of the Royal Astronomical Society*, Vol. 413, pp. 2281-2287.

Jacquemart, D., Mandin, J. -Y., Dana, V., Claveau, C., Vander Auwera, J., Herman, M., Rothman, L. S., Régalia-Jarlot, L., & Barbe, A. 2003, "The IR Acetylene Spectrum in HITRAN: Update and New Results," *Journal of Quantitative Spectroscopy & Radiative Transfer*, Vol. 82, pp. 363-382.

Johnstone, D., Wilson, C. D., Moriarty-Schieven, G., Joncas, G., Smith, G., Gregersen, E., and one co-author 2000, "Large-Area Mapping at 850 Microns. II. Analysis of the Clump Distribution in the ρ Ophiuchi Molecular Cloud," *The Astrophysical Journal*, Vol. 545, pp. 327-339.

Jørgensen, J. K., Harvey, P. M., Evans II, N. J., Huard, T. L., Allen, L. E., Porras, A., and 16 co-authors 2006, "The Spitzer c2d Survey of Large, Nearby, Interstellar Clouds. III. Perseus Observed with IRAC," *The Astrophysical Journal*, Vol. 645, pp. 1246-1263.

Keane, J. V., Boogert, A. C. A., Tielens, A. G. G. M., Ehrenfreund, P., Schutte, W. A. 2001 "Bands of Solid CO_2 in the 2-3 μm Spectrum of S 140:IRS1," *Astronomy & Astrophysics*, Vol. 375, pp. L43-L46.

Keane, J. V., Tielens, A. G. G. M., Boogert, A. C. A., Schutte, W. A., and Whittet, D. C. B. 2001 "Ice Absorption Features in the 5-8 μm Region Toward Embedded Protostars," *Astronomy & Astrophysics*, Vol. 376, pp. 254-270.

Kemper, F., Vriend, W. J., Tielens, A. G. G. M., 2004, "The Absence of Crystalline Silicates in the Diffuse Interstellar Medium," *The Astrophysical Journal*, Vol. 609, pp. 826-837.

Kenyon, S. J., Dobrzycka, D., Hartmann, L., 1994,"A New Optical Extinction Law and Distance Estimate for the Taurus-Auriga Molecular Cloud," *Astronomical Journal*, Vol. 108, No. 5, pp. 1872-1880.

Kessler, M. F., Steinz, J. A., Anderegg, M. E., Clavel, J., Drechsel, G., and 6 co-authors 1996, "The Infrared Space Observatory (ISO) Mission," *Astronomy & Astrophysics*, Vol. 315, pp. L27-L31.

Kessler M. F., Muller T. G., Leech K., Arviset, C., Garcia-Lario, P., and 4 co-authors 2003, *The ISO Handbook, Volume I - Mission & Satellite Overview*, ESA SP-1262.

Knez, C., Boogert, A. C. A., Pontoppidan, K. M., Kessler-Silacci, J., van Dishoeck, E. F., Evans II, N. J., and three co-authors 2005, "Spitzer Mid-Infrared Spectroscopy of Ices Toward Extincted Background Stars," *The Astrophysical Journal*, Vol. 635, pp. L145-L148.

Knude, J. and Hog, E. 1998, "Interstellar Reddening from the HIPPARCOS and TYCHO Catalogues. I. Distances to Nearby Molecular Clouds and Star Forming Regions," *Astronomy & Astrophysics*, Vol. 338, pp. 897-904.

Koresko, C. D., Blake, G. A., Brown, M. E., Sargent, A. I., & Koerner, D. W. 1999, "Imaging the Haro 6-10 Infrared Companion," *The Astrophysical Journal*, Vol. 525, No. 1, pp. L49-L52.

Kunde, V. G., & Maguire, W. C. 1974, "Direct Integration Transmittance Model," *Journal of Quantitative Spectroscopy and Radiative Transfer*, Vol. 14, No. 8, pp. 803-817.

Lada, C. J., 1987, "Star Formation: From OB Associations to Protostars," *Interntaional Astronomical Union Sympsium, Star Forming Regions*, Vol. 115, pp. 1-18.

Lada, C. J., & Lada, E. A. 2003, "Embedded Clusters in Molecular Clouds,"*Annual Review of Astronomy & Astrophysics*, Vol. 41, pp. 57-115.

Lahuis, F., & van Dishoeck, E. F. 2000, "ISO-SWS Spectroscopy of Gas-Phase C_2H_2 and HCN Toward Massive Young Stellar Objects," *Astronomy & Astrophysics*, Vol. 355, pp. 699-712.

Lahuis, F., van Dishoeck, E. F., Boogert, A. C. A., Pontoppidan, K. A., Blake, G. A., & 6 co-authors 2006, "Hot Organic Molecules Toward a Young Low-Mass Star: A Look at Inner Disk Chemistry," *The Astrophysical Journal*, Vol. 636, No. 2, pp. L145-L148.

Langer, W. D., & Penzias, A. A. 1990, "$^{12}C/^{13}C$ Isotope Ratio Across the Galaxy From Observations of $^{13}C^{18}O$ in Molecular Clouds," *The Astrophysical Journal*, Vol 357, pp. 477-492.

Leinert, Ch., Beck, T. L., Ligori, S., Simon, M., Woitas, J., & Howell, R. R. 2001, "The Near-Infrared and Ice-Band Variability of Haro 6-10," *Astronomy & Astrophysics*, Vol. 369, pp. 215-221.

Leinert, Ch., & Haas, M. 1989, "Detection of an Infrared Companion to Haro 6-10," *The Astrophysical Journal*, Vol. 342, pp. L39-L42.

Lindblad, B. 1935, "A Condensation Theory of Meteoric Matter and its Cosmological Significance," *Nature*, Vol. 135, pp. 133-135.

Lombardi, M., Lada, C. J., Alves, J. 2008 "Hipparcos Distance Estimates of the Ophiuchus and the Lupus Cloud Complexes," *Astronomy & Astrophysics*, Vol. 480, No. 3, pp. 785-792.

Lyons, J. R., and Young, E. D. 2006, "CO Self-Shielding as the Origin of Oxygen Isotope Anomalies in the Early Solar Nebula," *Nature*, Vol. 435, No. 7040, pp. 317-320.

Maréchal, Y. 1987, "IR Spectra of Carboxlyic Acides in the Gas Phase: A Quantitative Reinvestigation," *Journal of Chemical Physics*, Vol. 87, pp. 6344-6353.

Markwick, A. J., Ilgner, M., Millar, T. J., & Henning, Th. 2002, "Molecular Distributions in the Inner Regions of Protostellar Disks," *Astronomy & Astrophysics*, Vol. 385, pp. 632-646.

Marraco, H. G. and Rydgren, A. E. 1981, "On the Distance and Membership of the R Cr A T Association," *The Astronomical Journal*," Vol. 86, No. 1, pp. 62-68.

Matar, E., Congui, E., Dulieu, F., Momeni, A., Lemaire, J. L. 2008, "Mobility of D Atoms on Porous Amorphous Water Ice Surfaces Under Interstellar Conditions," *Astronomy & Astrophysics*, Vol. 492, No. 1, pp. L17-L20.

Mathis, J. S., Rumpl, W., and Nordsieck 1977, "The Size Distribution of Interstellar Grains," *The Astrophysical Journal*, Vol. 217, pp. 425-433.

McClure, M. K., Furlan, E., Manoj, P., Luhman, K. L., Watson, D. M., and 12 coauthors 2010, "The Evolutionary State of the Pre-Main Sequence Population in Ophiuchus: A Large Infrared Spectrograph Survey," *The Astrophysical Journal Supplement Series*, Vol. 188, pp. 75-122.

McKellar, A. 1940, "Evidence for the Molecular Origin of Some Hitherto Unidentified Interstellar Lines," *Astronomical Society of the Pacific*, Vol. 52, pp. 187-192.

McLean, I. S., Becklin, E. E., Bendriksen, O., Brims, G., Canfield, J., and 10 co-authors 1998, "Design and Development of NIRSPEC: a Near-Infrared Echelle Spectrograph for the Keck II Telescope," *Proceedings SPIE*, Vol. 3354, pp. 566-578.

Ménard, F., Monin, J.-L., Angelucci, F., & Rouan, D. 1993, "Disks Around Pre-Main-Sequence Binary Systems - The Case of Haro 6-10," *The Astrophysical Journal*, Vol. 414, No. 2, pp. L117-L120.

Menella, V., Palumbo, M. E., Baratta, G. A. 2004, "Formation of CO and CO_2 Molecules by Ion Irradiation of Water-Ice Covered Hydrogenated Carbon Grains," *The Astrophysical Journal*, Vol. 615, pp. 1073-1080.

Menten, K. M., Reid, M. J., Forbrich, J., Brunthaler, A. 2007, "The Distance to the Orion Nebula," *Astronomy & Astrophysics*, Vol. 474, No. 2, pp. 515-520.

Miyauchi, N., Hidaka, H., Chigai, T., Nagaoka, A., Watanabi, N., Kouchi, A. 2008, "Formation of Hydrogen Peroxide and Water from Reaction of Cold Hydrogen Atoms with Solid Oxygen at 10 K," *Chemical Physics Letters*, Vol. 456, No. 1-3, pp. 27-30.

Mokrane, H., Chaabouni, H., Accolla, M., Congiu, E., Dulieu, F., Chehrouri, M., and one co-author 2009, "Experimental Evidence for Water Formation Via Ozone Hydrogenation on Dust Grains at 10 K, " *The Astrophysical Journal Letters*, Vol. 705, No. 2, pp. L195-L198.

Mumma, M. J., DiSanti, M. A., Dello Russo, N., Magee-Sauer, K., Gibb, E., & Novak, R. 2003, "Remote Infrared Observations of Parent Volatiles in Comets: A Window on the Early Solar System," *Advances Space Research*, Vol. 31, No. 12, pp. 2563-2575.

Nummelin, A., Whittet, D. C. B., Gibb, E. L., Gerakines, P. A., Chiar, J. E. 2001, "Solid Carbon Dioxide in Regions of Low-Mass Star Formation," *The Astrophysical Journal*, Vol. 558, pp. 185-193.

Oba, Y., Miyauchi, N., Hidaka, H., Chigai, T., Watanabe, N., Kouchi, A. 2009, "Formation of Compact Amorphous H_2O Ice by Codeposition of Hydrogen Atoms with Oxygen Molecules on Grain Surfaces," *The Astrophysical Journal*, Vol. 701, No. 1, pp. 464-470.

Oba, Y., Watanabe, N., Kouchi, A., Hama, T., Pirronello, V. 2010, "Experimental Study of CO_2 Formation by Surface Reactions of Non-Energetic OH Radicals with CO Molecules," *The Astrophysical Journal Letters*, Vol. 712, pp. L174-L178.

Oberg, K. I., Boogert, A. C. A., Pontoppidan, K. M., Blake, G. A., Evans, N. J., Lahuis, F., et al.2008, "The c2d Spectroscopic Survey of Ices Around Low-Mass Young Stellar Objects. III. CH_4," *The Astrophysical Journal*, Vol. 678, pp. 1032-1041.

Oberg, K. I., Boogert, A. C. A., Pontoppidan, K. M., van den Broek, S., van Dishoeck, E. F., Bottinelli, S., and two co-authors 2011, "The Spitzer Ice Legacy: Ice Evolution From Cores to Protostars," *The Astrophysical Journal*, Vol. 740, pp. 109-124.

Oort, J.H. & van de Hulst, H. C., 1946, "Gas and Smoke in Interstellar Space," *Bulletin of the Astronomical Institutes of the Netherlands*, Vol. 10, No. 376, pp. 187-204.

Ostlie, D. A., & Carroll, B. W., *An Introduction to Modern Stellar Astrophysics*, 2nd Edition, Pearson Addison-Weasley: San Francisco, California (2007).

Peterson, D. E., Garatti, A. C., Bourke, T. L., Forbrich, J., Gutermuth, R. A., Jørgensen, J. K., and 11 co-authors 2011, "The Spitzer Survey of Interstellar Clouds in the Gould Belt. III. A Multi-Wavelength View of Corona Australis," *The Astrophysical Journal Supplement Series*, Vol. 193, Article 43 (43 pages).

Pontoppidan, K. M., Dartois, E., van Dishoeck, E. F., Thi, and W.-F., d'Hendecourt, L. 2003, "Detection of Abundant Solid Methanol Toward Young Low Mass Stars," *Astronomy & Astrophysics*, Vol. 404, L17-L20.

Pontoppidan, K. A. 2006, "Spatial Mapping of Ices in the Ophiuchus-F Core," *Astronomy & Astrophysics*, Vol. 453, No. 3, pp. L47-50.

Pontoppidan, K. A., Boogert, A. C. A., Fraser, H. J., van Dishoeck, E. F., Blake, G. A., Lahuis, F., and 3 co-authors 2008, "The c2d Spitzer Spectroscopic Survey of Ices Around Low-Mass Young Stellar Objects. II. CO_2," *The Astrophysical Journal*, Vol. 678, pp. 1005-1031.

Porras, A., Christopher, M., Allen, L., Di Francesco, J., Megeath, S. T., Myers, P. C. 2003, "A Catalog of Young Stellar Groups and Clusters within 1 Kiloparsec of the Sun," *The Astronomical Journal*, Vol. 126, No. 4, pp. 1916-1924.

Rayner, J. T., Toomey, D. W., Onaka, P. M., Denault, A. J., Stahlberger, W. E., and three co-authors 2003, "SpeX: A Medium-Resolution 0.8-5.5 Micron Spectrograph and Imager for the NASA Infrared Telescope Facility," *The Publications of the Astronomical Society of the Pacific*, Vol. 115, No. 804, pp. 362-382.

Rettig, T. W., Brittain, S. D., Simon, T., Gibb, E. L., Balsara, D. S., Tilley, D. A., & Kulesa, C. 2006, "Dust Stratification in Young Circumstellar Disks," *The Astrophysical Journal*, Vol. 646, pp. 342-350.

Roccatagliata, V., Ratzka, T., Henning, T., Wolf, S., Leinert, C., and Bouwman, J. 2011, "Multi-wavelength Observations of the Young Binary System Haro 6-10: The Case of Misaligned Disks," *Astronomy and Astrophysics*, Vol. 534, pp. A33:1-13.

Romanzin, C., Ioppolo, S. Cuppen, H. M., van Dishoeck, E. F., Linnartz, H. 2011, "Water Formation by Surface O_3 Hydrogenation," *Journal of Chemical Physics*, Vol. 134, No. 8, pp. 084504-084504-7.

Roser, J. E., Vidali, G., Manicó, G., Pirronello, V. 2001 "Formation of Carbon Dioxide by Surface Reactions on Ices in the Interstellar Medium," *The Astrophysical Journal*, Vol. 555, L61-L64.

Rothman, L. S., Jacquemart, D., Barbe, A., Benner, C. D., Birk, M., Brown, L. R. and 24 co-authors 2005, "The HITRAN 2004 Molecular Spectroscopic Database," *Journal of Quantitative Spectroscopy & Radiative Transfer*, Vol. 96, pp. 139-204.

Ruffle, D. P., Herbst, E. 2001, "New Models of Interstellar Gas-Grain Chemistry - III. Solid CO_2," *Monthly Notices of the Royal Astronomical Society*, Vol. 324, pp. 1054-1062.

Schreyer, K., Henning, Th., van der Tak, F. F. S., Boonman, A. M. S., van Dishoeck, E. F. 2002, "The Young Intermediate-Mass Stellar Object AFGL 490 - A Disk Surrounded by a Cold Envelope," *Astronomy & Astrophysics*, Vol. 394, pp. 561-583.

Schutte, W. A., Allamandola, L. J., and Sandford, S. A. 1993, "An Experimental Study of the Organic Molecules Produced in Cometary and Interstellar Ice Analogs by Thermal Formaldehyde Reactions," *Icarus*, Vol. 104, No. 1, pp. 118-137.

Schutte, W. A., Tielens, A. G. G. M., Whittet, D. C. B., Boogert, A. C. A., Ehrenfreund, P., de Graauw, Th., and two co-authors 1996, "The 6.0 and 6.8 μm Absorption Features in the Spectrum of NGC 7538:IRS9," *Astronomy and Astrophysics*, Vol. 315, pp. L333-L336.

Schutte, W. A. and Greenberg, J. M. 1997, A&A, 317, L43.

Schutte, W. A., Boogert, A. C. A., Tielens, A. G. G. M, Whittet, D. C. B., Gerakines, P. A., Chiar, J. E., and four co-authors 1999, "Weak Ice Absorption Features at 7.24 μm and 7.41 μm in the Spectrum of the Obscured Young Stellar Object W33A*," *Astronomy & Astrophysics*, Vol. 343, pp. 966-976.

Schutte, W. A. and Khanna, R. K. 2003, "The Origin of the 6.85 μm Band Near Young Stellar Objects. The Ammonium Ion (NH_4^+) Revisited," *Astronomy & Astrophysics*, Vol. 398, pp. 1049-1062.

Semenov, D., Chakraborty, S., Thiemens, M. "Chemical and Isotopic Evolution of the Solar Nebula and Protoplanetary Disks," *Protoplanetary Dust: Astrochemical and Cosmochemical Perspectives*, Cambridge University Press: New York (2010).

Smith, J. D. T., Draine, B. T., Dale, D. A., Moustakas, J., Kennicutt, Jr., R. C., and 14 co-authors 2007, "The Mid-Infrared Spectrum of Star-forming Galaxies: Global Properties of Polycyclic Aromatic Hydrocarbon Emission," *The Astrophysical Journal*, Vol. 656, pp. 770-791.

Snow, T. P., Destree, J. D., Welty, D. E. 2008, "A Study of the ρ Ophiuchi Cloud: Mapping the Distribution and the Motions of Interstellar Gas," *The Astrophysical Journal*, Vol. 679, No. 1, pp. 512-530.

Straizys, V., Cernis, K., and Bartasiute, S. 1996, "Interstellar Extinction in the Area of the Serpens Cauda Molecular Cloud," *Baltic Astronomy*, Vol. 5, pp. 125-147.

Swings, P., Rosenfeld, L. 1937, "Considerations Regarding Interstellar Molecules," *The Astrophysical Journal*, Vol. 86, pp. 483-486.

Tanaka, M., Nagata, T., Sato, S., Yamamoto, T. 1994, "The Nature of CO and H_2O Ices in the Corona Australis Molecular Cloud," *The Astrophysical Journal*, Vol. 430, No. 2, pp. 779-785.

Teixeira, T. C. and Emerson, J. P. 1999, "Determining the Extinction Through Dark Clouds," *Astronomy and Astrophysics*, Vol 351, pp. 303-308.

Tielens, A. G. G. M. and Hagen, W. 1982, "Model Calculations of the Molecular Composition of Interstellar Grain Mantles," *Astronomy & Astrophysics*, Vol. 114, pp. 245-260.

Tielens, A. G. G. M. and Allamandola, L. J. 1987, *Physical Processes in Interstellar Clouds*, pp. 333

Vacca, W. D., Cushing, M. C., Rayner, J. T. 2003, "A Method of Correcting Near-Infrared Spectra for Telluric Absorption," *The Publications of the Astronomical Society of the Pacific*, Vol. 115, No. 805, pp. 389-409.

van de Hulst, H. C. 1946, "The Solid Particles in Interstellar Space," *Recherches Astronomiques de l'Observatoire d'Utrect*, Vol. 11, pp. 2.i-50.

van den Ancker M. E., Wesselius P. R., Tielens, A. G. G. M. 2000, "ISO Spectroscopy of Young Intermediate-mass Stars in the BD+40°4124 Group," *Astronomy & Astrophysics*, Vol. 355, pp. 194-210.

van den Ancker, M. E., "ISO Observations of Pre-Main-Sequence Vega-Type Stars", *The Publications of the Astronomical Society of the Pacific*, Vol. 219, pp. 242-254.

Vandenbussche, B., Ehrenfreund, P., Boogert, A. C. A., van Dishoeck, E. F., Schutte, W. A., Gerakines, P. A., and six co-authors 1999, "Constraints on the Abundance of solid O_2 in Dense Clouds from ISO-SWS and Ground-Based Observations," *Astronomy & Astrophysics*, Vol. 346, pp. L57-L60.

Vander Auwera, J., Hurtmans, D., Carleer, M., and Herman, M. 1993, "The ν_3 Fundamental in C_2H_2," *Journal Molecular Spectroscopy*, Vol. 157, pp. 337-357.

van Dishoeck, E.F. and Blake, G.A. 1998, "Chemical Evolution of Star-Forming Regions," *Annual Reviews of Astronomy and Astrophysics*, Vol. 36, pp. 317-368.

van Dishoeck, E. F., 2004, "ISO Spectroscopy of Gas and Dust: From Molecular Clouds to Protoplanetary Disks," *Annual Reviews of Astronomy and Astrophysics*, Vol. 42, pp. 119-167.

Walsh, C., Millar, T. J., and Nomura, H. 2010, "Chemical Processes in Protoplanetary Disks," *The Astrophysical Journal*, Vol. 722, pp. 1607-1623.

Werner, M. W.; Roellig, T. L.; Low, F. J.; Rieke, G. H., Rieke, M., Hoffman, W. H., and 20 coauthors 2004, "The Spitzer Space Telescope Mission," *Astrophysical Journal Supplement Series* Vol. 154, pp. 1-9.

White, G. J., Liseau, R., Men'shchikov, A. B., Justanonot, K., Nisini, B., Benedettini, M., Caux, E., and ten co-authors 2000, "An Infrared Study of the L1551 Star Formation Region," *Astronomy & Astrophysics*, Vol. 364, pp. 741-762.

White, R. J., & Hillenbrand, L. A. 2004, "On the Evolutionary Status of Class I Stars and Herbig-Haro Energy Sources in Taurus-Auriga," *The Astrophysical Journal*, Vol. 616, pp. 998-1032.

White, D. W.; Gerakines, P. A.; Cook, A. M.; & Whittet, D. C. B. 2009, "Laboratory Spectra of the CO_2 Bending-Mode Feature in Interstellar Ice Analogs Subject to Thermal Processing," *Astrophysical Journal Supplement Series*, Vol. 180, pp. 182-191.

Whittet, D. C. B., *Dust in the Galactic Environment (2nd Edition)*, Institute of Physics Publishing: Philadelphia, Pennsylvania (2003).

Whittet, D. C. B., Shenoy, S. S., Bergin, E. A., Chiar, J. E., Gerakines, P. A., Gibb, E. L., et al.2007, "The Abundance of Carbon Dioxide Ice in the Quiescent Intracloud Medium," *The Astrophysical Journal*, Vol. 655, pp. 332-341.

Whittet, D. C. B., Cook, A. M., Chair, J. E., Pendleton, Y. J., Shenoy, S. S., and Gerakines, P. A. 2009, "The Nature of Carbon Dioxide Bearing Ices in Quiescent Molecular Clouds," *The Astrophysical Journal*, Vol. 695, No. 1, pp. 94-100.

Wilking, B. A., Lada, C. L., Young, E. T. 1989, "IRAS Observations of the ρ Ophiuchi Infrared Cluster: Spectral Energy Distributions and Luminosity Function," *The Astrophysical Journal*, Vol. 340, pp. 823-852.

Wilking, B. A., Gagne, M., Cook, L. A. 2008, "Handbook of Star Formation Regions: Star Formation in the ρ Ophiuchi Molecular Cloud," *Astronomical Society of the Pacific*, Vol. II, pp. 1-30.

Wilking, B. A., Marvel, K. B., Claussen, M. J., Gerling, B. M., Wootten, A., Gibb, E. L. 2012, "A Proper Motion Study of the Haro 6-10 Outflow: Evidence for a Subarcsecond Binary," *The Astrophysical Journal*, Vol. 753, pp. 143.

Willacy, K., Klahr, H. H., Millar, R. J., & Henning, Th. 1998, "Gas and Grain Chemistry in a Protoplanetary Disk," *Astronomy & Astrophysics*, 338, 995-1005.

Willacy, K., Langer, W., Allen, M., and Bryden, G. 2006, "Turbulence-Driven Diffusion in Protoplanetary Disks: Chemical Effects in the Outer Regions," *The Astrophysical Journal*, Vol. 644, pp. 1202-1213.

Willacy, K., Woods, P. M. 2009, "Deuterium Chemistry in Protoplanetary Disks. II. The Inner 30 AU," *The Astrophysical Journal*, Vol. 703, pp. 479-499.

Williams, J. P., Cieza, L. A. 2011, "Protoplanetary Disks and Their Evolution," textitAnnual Reviews of Astronomy and Astrophysics," Vol. 49, pp. 67-117.

Wilson, T. L., & Rood, R. 1994, "Abundances in the Interstellar Medium," *Astronomy & Astrophysics*, Vol. 32, pp. 191-226.

Woon, D.E. 2002, "Modelling Gas-Grain Chemistry with Quantum Chemical Cluster Calculations. I. Heterogeneous Hydrogenation of CO and H_2CO on Icy Grain Mantles," *The Astrophysical Journal*, Vol. 569, pp. 541-548.

Zasowski, G., Kemper, F., Watson, D. M., Furlan, E., and 4 coauthors, 2009, "Spitzer Infrared Spectrograph Observations of Class I/II Objects in Taurus: Composition and Thermal History of the Circumstellar Ices," *Astrophysical Journal*, Vol. 694, No. 1, pp. 459-478.

VITA

Kari Anne Wojtkowski was born in 1977 in St. Louis, MO to David and Susan Wojtkowski. She graduated from Hillsboro High School in 1995 as the Valedictorian of her class. She went to University of Missouri - Rolla (now Missouri University of Science and Technology) and graduated Magna Cum Laude with a Bachelor of Science in Physics in May 1999. From there, she continued her studies in Physics at the University of Missouri - St. Louis, where she earned a Master of Science in May 2001. Kari was supported at the University of Missouri - St. Louis with a NASA Missouri Space Grant Consortium fellowship in her pursuit of a Ph.D. She was the recipient of the Outstanding Graduate Teaching Award in 2001 and a Sigma Xi Grants-in-Aid of Research Award in 2007. She has presented posters at several professional conferences, including American Astronomical Society meetings and Spitzer Space telescope meeting "Reionization to Exoplanets: Spitzer's Growing Legacy." In addition to those professional conferences, she also participated in local conferences such as Sigma Xi night at the Missouri Botanical Gardens, Midwest Astrochemistry Consortium meetings, University of Missouri - St. Louis Graduate Fairs, and Joint UMSL-Rolla Joint Physics meetings. Her poster presentation placed in the top three at the UMSL-Rolla Joint Meeting in 2007 and the UMSL Graduate Fair in 2011. While pursuing her graduate degree, Kari has taught courses such as Introductory Astronomy, College Physics II, Earth Science, and Introduction to Physical Science at various St. Louis institutions, including UM–St. Louis, St. Louis Community College at Meramec, Fontbonne University, and Jefferson College.